2019

Energy Harvesting from Natural Water Flow

Haonan Kong
University of Windsor

ENERGY HARVESTING FROM NATURAL WATER FLOW

By

Haonan Kong

A Thesis
Submitted to the Faculty of Graduate Studies
through the Department of **Mechanical, Automotive & Materials Engineering**
in Partial Fulfillment of the Requirements for
the Degree of **Master of Applied Science**
at the University of Windsor

Windsor, Ontario, Canada

2019

ENERGY HARVESTING FROM NATURAL WATER FLOW

by

Haonan Kong

APPROVED BY:

_____

X. Nie
Department of Mechanical, Automotive & Materials Engineering

_____

D. Ting
Department of Mechanical, Automotive & Materials Engineering

_____

V. Stoilov, Co-Advisor
Department of Mechanical, Automotive & Materials Engineering

_____

V. Roussinova, Co-Advisor
Department of Mechanical, Automotive & Materials Engineering

May 16th, 2019

DECLARATION OF ORIGINALITY

I hereby certify that I am the sole author of this thesis and that no part of this thesis has been published or submitted for publication.

I certify that, to the best of my knowledge, my thesis does not infringe upon anyone's copyright nor violate any proprietary rights and that any ideas, techniques, quotations, or any other material from the work of other people included in my thesis, published or otherwise, are fully acknowledged in accordance with the standard referencing practices. Furthermore, to the extent that I have included copyrighted material that surpasses the bounds of fair dealing within the meaning of the Canada Copyright Act, I certify that I have obtained a written permission from the copyright owner(s) to include such material(s) in my thesis and have included copies of such copyright clearances to my appendix.

I declare that this is a true copy of my thesis, including any final revisions, as approved by my thesis committee and the Graduate Studies office, and that this thesis has not been submitted for a higher degree to any other University or Institution.

ABSTRACT

The hydrokinetic energy contained in flowing water is plentiful and has the potential to be one of the environmentally friendly renewable sources of energy that can be harvested. A new energy harvesting system utilizing Vortex-induced Vibration (VIV) is presented and analysed in this thesis. The proposed energy harvester generates power by direct conversion of the hydrokinetic energy of water flow into mechanical vibrations. The harvester experiences alternating fluid forces due to the repeatable pattern of alternating vortices shed from the sides of the body which generates a wake with Von Kármán Vortex Street. The proposed harvester consists of two coupled components: a bluff body with specific geometry that produces mechanical oscillations from VIV resulting in periodic vibrations and a set of piezoelectric transducers that harvest the mechanical energy from the vibrations. This typical Fluid-structure Interaction (FSI) between fluid flow and the energy harvester was studied using numerical modeling and experimental tests. The vibrational power output of the energy harvester was directly measured from data acquisition system during experimental tests. The VIV response of the proposed harvester with two degrees-of-freedom (DOF) is also investigated numerically at different input velocities. Potential power output generated by the harvester was calculated based on the results from the two-way coupled numerical model and reported over a range of input velocity. A single energy harvester demonstrated a peak power output of 41 mW, from an input flow velocity of ~8 m/s.

DEDICATION

This thesis is dedicated to a greener future and the progressive society that focuses on it.

ACKNOWLEDGEMENTS

I would like to take this opportunity to express my sincere gratitude to my advisors, Dr. Vesselin Stoilov & Dr. Vesselina Roussinova, for being my inspiration and mentors. Their valuable advice, insightful criticism, and patient encouragement aided my research work in innumerable ways. Steadfast support and professional advice provided by the laboratory technicians was greatly appreciated.

I wish to offer my special thanks to my family, whose upbringing has taught me to have diligent and hardworking attitude; to my colleagues and friends, for encouraging me to further myself; to my soulmate, for her love, support and unwavering belief in me.

TABLE OF CONTENTS

LIST OF TABLES

LIST OF FIGURES

LIST OF APPENDICES

APPENDIX C: TABLES

LIST OF ABBREVIATIONS/SYMBOLS

VIV: Vortex-induced Vibration

FSI: Fluid-structure Interaction

FIM: Fluid-induced Motion

PZT: Lead-zirconate-titanate

PVDF: Polyvinylidene Fluoride

MFC: Macro-fibre Composite

CFD: Computational Fluid Dynamics

RANS: Reynolds Averaged Navier-Stokes

SST: Shear Stress Transport

DNS: Direct Numerical Simulation

LES: Large Eddy Simulation

PDE: Partial Differential Equation

DES: Detached Eddy Simulation

DDES: Delayed Detached Eddy Simulation

VIVACE: Vortex Induced Vibration Aquatic Clean Energy

PTC: Passive Turbulence Control

QP: Bimorph Quick Pack actuator

CAD: Computer-Aided-Design

EFS: Elastic Foundation Stiffness

DAQ: Data Acquisition System

FFT: Fast Fourier Transformation

NOMENCLATURE

δ = Mechanical Strain

σ = Mechanical Stress

Y = Young's modulus of the material

d = Piezoelectric strain coefficient

E = Electric field

D = Electrical displacement

ε = Dielectric constant of the piezoelectric material

U = free stream velocity (m/s)

D = diameter of cylinder (m)

f^* = inline to cross-flow natural frequency ratio

V_r = reduced velocity

A/D = normalized amplitude

m^*= mass ratio

d = length Scale

C_{DES}= DES model constant

Δ = local grid spacing

C_D= drag coefficient

C_L = lift coefficient

Re = Reynolds Number

v = kinematic viscosity (m^2/s)

S_t = Strouhal Number

f_s = vortex shedding frequency (Hz)

m = oscillating mass (kg)

k_s = spring stiffness (N/m)

c_s= damping coefficient

α= Variation

β= Rate

A_p= Projected area

CHAPTER 1

INTRODUCTION

1.1 The Necessity of Energy Harvesting

The climate change, pollution and depletion from the non-renewable energy has always been one of the serious concerns for today's world, undoubtedly, the impacts on our planet, ecosystems, cities and energy usage is significant. The fast growing economy and technological development requires an alternative approach to reduce and overcome the use of fossil fuels to achieve sustainability.

Energy harvesting is the capture and conversion of small amounts of available energy in the environment into usable energy, such as electrical energy. The electrical energy is conditioned for either direct use or accumulated and stored for later use. This provides an alternative source of power for applications in locations where there is no grid power and it is inefficient to install wind turbines or solar panels [1].

The Energy harvesting is beneficial because it provides a means of powering electronics where there are no conventional power sources, eliminating the need for frequent battery replacements and running wires to end applications. By this same token, it opens up new applications in remote locations, underwater, and other difficult-to-access locations where batteries and conventional power are not realistic. On the other hand, energy harvesting is also largely maintenance free and environmentally friendly.

1.2 Renewable Energy Resources

Renewable energy is the type of energy source which can be derived from natural processes that are replenished at a rate that is equal or faster than the rate at which they are consumed. There are various forms of renewable energy, deriving directly or indirectly from the sun, from heat generated deep within the earth and fluid flow including wind and water (hydro, wave or tidal energy).

1.2.1 Solar Energy

The Sun is an extremely powerful and plentiful energy sources, the energy extracted from sunlight can be used without releasing greenhouse gases or harmful by-products. There are two main technologies to harvest solar energy, which are solar photovoltaic and solar thermal. Solar radiation may be converted directly into electricity by solar cells (photovoltaic cells). In such cells, a small electric voltage is generated when light strikes the junction between a metal and a semiconductor (such as silicon) or the junction between two different semiconductors. The power generated by a single photovoltaic cell is typically only about 2 *W*. By connecting large numbers of individual cells together, however, as in solar-panel arrays, hundreds or even thousands of kilowatts of electric power can be generated in a solar electric plant or in a large household array. The energy efficiency of most present-day photovoltaic cells is only about 15 to 20 percent, and, since the intensity of solar radiation is low to begin with, large and costly assemblies of such cells are required to produce even moderate amounts of power [2].

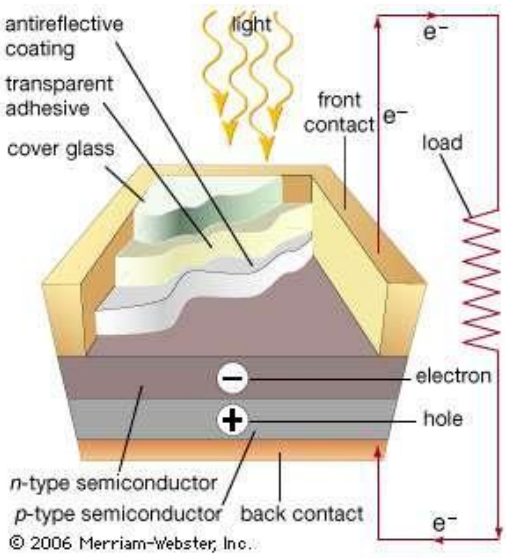

Figure 1 Photovoltaic Cell (britannica.com.)

Solar energy also can be converted directly into thermal energy by solar thermal collectors, which essentially a group of mirrors and lenses designed into specific configuration to track the sun from east to west during the day and concentrate sunlight continuously onto the receiver. Such a system can supply a home with hot water drawn from the storage tank, or, with the warmed water flowing through tubes in floors and ceilings, which can provide space heating. The efficiency of solar thermal collectors varies from 20 to 80 percent depends on the actual design and natural conditions [2].

1.2.2 Geothermal Energy

Geothermal power is a form of renewable energy utilizing subsurface hot water or steam created by the heat beneath the Earth's surface. The heat is produced mainly by the radioactive decay of potassium, thorium, and uranium in Earth's crust and mantle and also by friction generated along the margins of continental plates. Geothermal heat energy can be recovered and exploited for human use; the geothermal power plants pump the heated water or steam to power

the turbine that is used to generate electricity. The excess water vapour at the end of process is condensed and returned to the ground, where it can be reheated. Figure 2 is an example of a geothermal power plant with flash steam design, which uses mixture of steam and heated water extracted from the ground to start electrical generation process. The subsequent annual low-grade heat flow to the surface averages between 50 and 70 *mW* per square metre worldwide. In contrast, incoming solar radiation striking Earth's surface provides 342 *W* per square metre annually [3, 4].

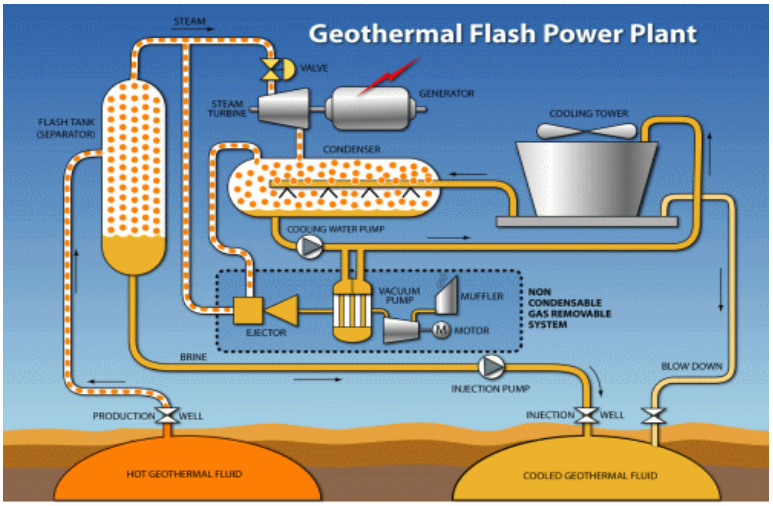

Figure 2 Geothermal Power Plant (edu.glogster.com)

1.2.3 Wind Energy

Wind is a form of solar energy and is a result of the uneven heating of the atmosphere by the Sun, the irregularities of the Earth's surface, and the rotation of the Earth. Wind turbine, or wind energy harvester is a device that harvest the kinetic energy in the wind and convert it into mechanical and electrical energy. The kinetic energy contained in the wind drives the propeller-

shaped blades around the rotor, and the rotor is connected to the shaft of the generator to produce electricity. The voltage of the electricity produced by the wind turbine is then increased by a transformer and substation to enable it to be fed into electricity grid. Wind turbines convert around 35 to 50 percent of kinetic energy in the wind passing through the blades into electricity. Individual wind turbine has much smaller capacity compared to the coal power plant, however, collectively they can supply electricity at a larger scale and ready for mass deployment. A group of wind turbines in the same location is called wind farm. The averaged capacity for a wind farm in Australia ranges from 25 to 45 percent [5, 6]. Although, wind turbine has a drawback that it cannot generate power constantly due to the natural condition varies over the seasons, especially in winter. On the other hand, wind turbines generate noise and visual pollution, and the use of land area is not profitable.

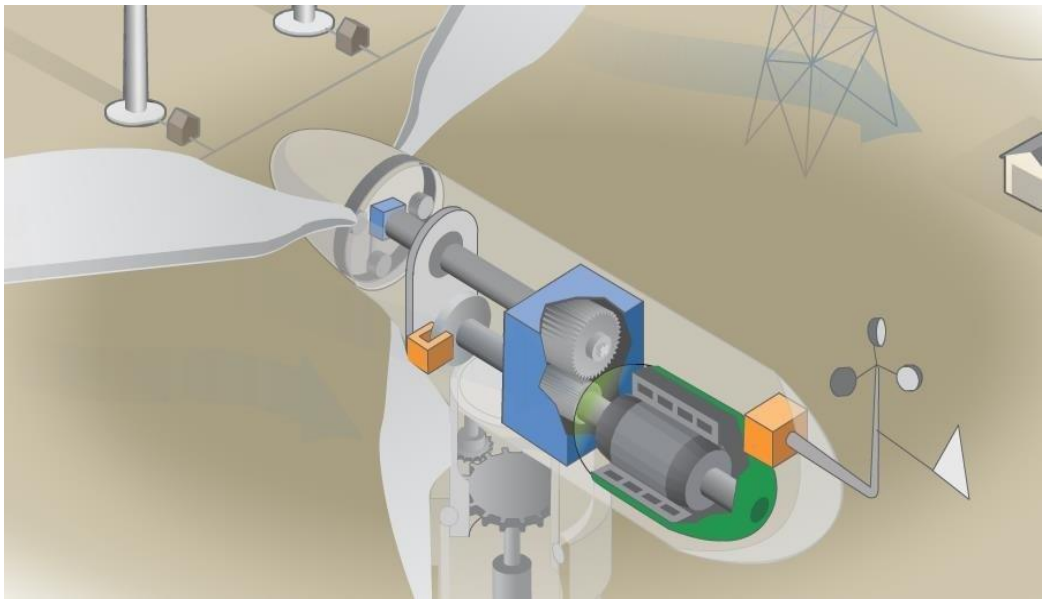

Figure 3 Wind Turbine (energy.gov)

1.3 Energy Harvesting from Fluid Flow

Energy harvester which is aiming to harvest and convert the kinetic energy available in the fluid flow into electricity requires a transduction mechanism. For harvesting the wind energy, the propeller converts the kinetic energy of the wind into mechanical energy of the rotor, which powers the generator to produce electricity. Some other applications focus on utilizing Fluid-induced Motions (FIM) by introducing a bluff body that interacting in the external fluid flow field. By placing a bluff body into a fluid moving with a certain velocity causes vortex formation which results in vibrations and oscillations of the bluff body. The vibrational energy of the bluff body can be harvested and further converted into other usable form of energy.

Electromagnetic, electrostatic and piezoelectric transductions are the three main methodologies that are being implemented to convert the mechanical energy to electricity. For small-scale energy harvesting, the piezoelectric transduction has more advantages, such as larger power density, relatively high voltage and no separate voltage source is required for initialization. On the other hand, electromagnetic approach requires large amplitude while in the fluid as water, which has high viscosity, small amplitude results from VIV is to be expected. Thus, the proposed harvester in this thesis is focusing on piezoelectric transduction, which converts the mechanical strain of the piezoelectric material directly into electric charges on its surface. Piezoelectric transducers are not reliant on the external voltage input, easier to be installed and collaborate with the compact design. On the other hand, with the application of piezoelectric transducer, mechanical stops is not required so that the device can be designed to exhibit very little mechanical damping, in other words, less energy losses.

1.4 Piezoelectric Generators

The piezoelectric effect is the ability of some materials to generate an electric potential in response to applied mechanical stress, which was discovered by Pierre and Jacques Curie in 1880 [7]. The electrical polarization is proportional to the applied strain. This is the piezoelectric effect used for mechanical to electrical energy conversion. Commonly used materials for piezoelectric power generation are lead-zirconate-titanate (PZT), polyvinylidene fluoride (PVDF) [8] and macro-fibre composite (MFC) [9].

Piezoelectric generators generally work in two modes: 33 mode (Figure 4(a)) or 31 mode (Figure 4(b)). In the 33 mode, a force is applied in the same direction as the poling direction, such as the compression of a piezoelectric block that has electrodes on its top and bottom surfaces. In the 31 mode, a lateral force is applied in the direction perpendicular to the poling direction, an example of which is a bending beam that has electrodes on its top and bottom surfaces. The 31 mode is the most commonly used coupling mode for energy generation although the 31 mode has lower efficiency than the 33 mode [8].

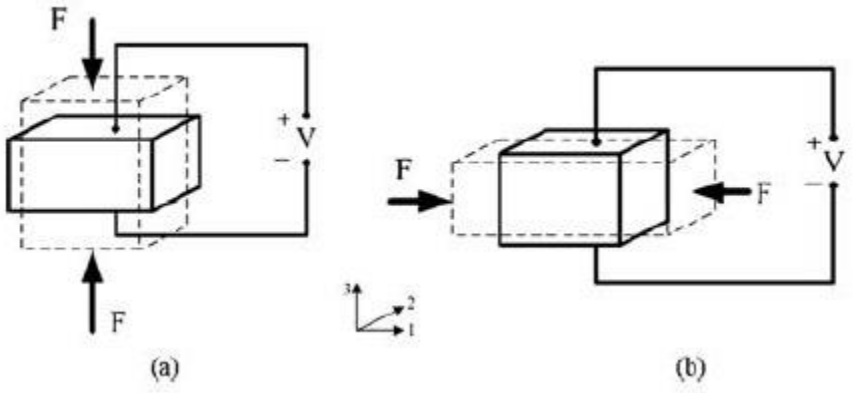

Figure 4 Piezoelectric Generators: (a) 33 mode (b) 31 mode

The constitutive equations for a piezoelectric material are given by:

$$\delta = \frac{\sigma}{Y} + d \cdot E \tag{1}$$

$$D = \varepsilon \cdot E + d \cdot \sigma \tag{2}$$

where δ is mechanical strain, σ is mechanical stress, Y is Young's modulus of the material, d is the piezoelectric strain coefficient, E is the electric field, D is the electrical displacement (charge density) and ε is the dielectric constant of the piezoelectric material [7].

Table 1 lists properties of some common piezoelectric materials. Output power of piezoelectric generators in same dimensions using different piezoelectric material is compared in Figure 5.

Table 1 Coefficient of Common Piezoelectric Materials [10, 11]

Material	PZT-5H	PZT-5A	$BaTiO_3$	PVDF
$d_{31}(\times 10^{-12} CN^{-1})$	-274	-171	78	23
Young's modulus (GPa)	50	50	67	2
Relative permittivity (ϵ/ϵ_0)	3400	1700	1700	12

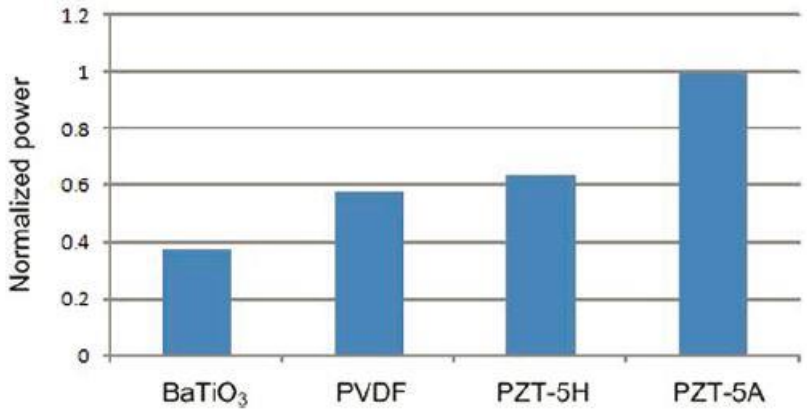

Figure 5 Comparison of Output Power of Different Piezoelectric Generators

From Figure 5, it is found that with the same dimension, the generator using PZT has the most amount of output power. However, the PZT type piezoelectric material has high stiffness, which is limited to fewer applications. Considering the nature of water flow and the lower cost and higher flexibility of PVDF piezoelectric polymer, PVDF piezoelectric material is selected for the proposed energy harvester in this thesis.

1.5 Objectives

The main objectives of the research study are:

- To develop a new energy harvesting system that converts the hydrokinetic energy of natural water flow into usable energy.
- To investigate the FSI between fluid flow and the proposed harvester including VIV responses in stream-wise and transverse directions, and the flow characteristics of the near wake.

The second objective also serves as important design step for the optimization of the energy harvesting system. The VIV response amplitude and frequency of the harvester are the two main parameters that must be quantified and optimized. It is expected that the three-dimensional (3-D) two-way coupled Computational Fluid Dynamics (CFD) modelling is going to provide accurate predictions for the VIV response of the proposed harvester and its energy harvesting potentials.

CHAPTER 2

LITERATURE REVIEW

This chapter provides an overview of literature including the concepts involved in energy harvesting from fluid flow by utilizing VIV, and a summary of the existing technologies related to the application of VIV and piezoelectric materials. The literature review is divided into two main sections. The first section presents basic concepts of VIV, VIV of circular cylinder and turbulence viscous models being applied in the numerical simulations. The second section discussed the design, numerical and experimental results of some existing energy harvesting technologies.

2.1 Concepts of VIV and Viscous model

In engineering practices involving fluid past a bluff body, VIV is commonly treated as an unwanted phenomenon that may lead to excessive structural vibrations and fatigue damage. In structural and marine engineering, potential failures due to VIV were observed in marine riser pipes and bridge decks, thus the prediction of these vibrations become critical [12]. The common reason for studying VIV has been the need to avoid it or eliminate/attenuate the vibrations. The purpose of this research, however, is to utilize the vibrations for harvesting the hydrokinetic energy of the fluid flow. Flowing water (natural currents and rivers) contains hydrokinetic energy which can be harnessed by using the VIV of a bluff body. VIVs result from the interaction between a solid body and moving fluid - a type of FIM. Vortex shedding from a rigid, circular cylinder can be defined as periodic detachment of pairs of alternative vortices that travel in the wake. The oscillating wake generates a Von Kármán vortex street behind the cylinder causing fluctuating forces to be experienced by the body [13, 14]. For the case of elastically

mounted cylinder, fluctuating forces generated in the wake excite the cylinder to oscillate with a certain frequency and amplitude. When the cylinder's natural frequency is locked into the frequency of the vortices shed in the wake, there is a resonance and the maximum VIV response is achieved.

For vortex shedding of stationary circular cylinder, near the widest section of the cylinder, the boundary layers separates from each side of the cylinder surface and form two shear layers that trail after the flow and bound the wake. Since the innermost portion of the shear layers, which is in contact with the cylinder, moves much more slowly than the outermost portion of the shear layers, which is in contact with the free flow, the shear layers roll into the near wake, where they fold on each other and coalesce into discrete swirling vortices [15, 16]. A regular pattern of vortices, called a vortex street, trails aft in the wake. The vortices interact with the cylinder and they are the source of the effects called VIV.

Vortex shedding from a smooth, circular cylinder in a steady flow is a function of Reynolds number. The Reynolds number is based on free stream velocity (U) and cylinder diameter (D),

$$Re = \frac{UD}{\nu} \tag{3}$$

where ν is the kinematic viscosity of the fluid. The major Reynolds number regimes of vortex shedding from a smooth circular cylinder is summarized by Lienhard [17], are given in Figure 6. At very low Reynolds numbers, below about Re = 5, the fluid flow follows the cylinder contours. In the range of $5 \leq \text{Re} \leq 45$, the flow separates from the back of the cylinder and a symmetric pair of vortices is formed in the near wake. The stream-wise length of the vortices increases

linearly with Reynolds number, reaching a length of three cylinder diameters at Reynolds number of 45 [18]. As Reynolds number is further increased, the wake becomes unstable [19] and one of the vortices breaks away [20]. A laminar periodic wake of staggered vortices of opposite sign (Vortex Street) is formed. Roshko et al. [21] found that between Re =150 and 300, the vortices breaking away from the cylinder become turbulent, although the boundary layer on the cylinder remains laminar.

The Reynolds number range $300 < \mathrm{Re} < 1.5 \times 10^5$ is called subcritical. In this range, the laminar boundary layers separate at about 80 degrees aft of the nose of the cylinder and the vortex shedding is strong and periodic. In the transitional range, $1.5 \times 10^5 < \mathrm{Re} < 3.5 \times 10^6$, the boundary layer becomes turbulent, the separation points move aft to 140 degrees, and the cylinder drag coefficient drops to 0.3 [22]. In the transitional range, laminar separation bubbles and three-dimensional effects disrupt the regular shedding process and broaden the spectrum of shedding frequencies for a smooth cylinder [23, 24, 25, 26]. In the supercritical Reynolds number range, where $\mathrm{Re} > 3.5 \times 10^6$, vortex shedding is reformed with a turbulent cylinder boundary layer [27]. Lastly, the vortex shedding persists at Reynolds numbers as high as $\mathrm{Re} = 10^{11}$ [28, 29].

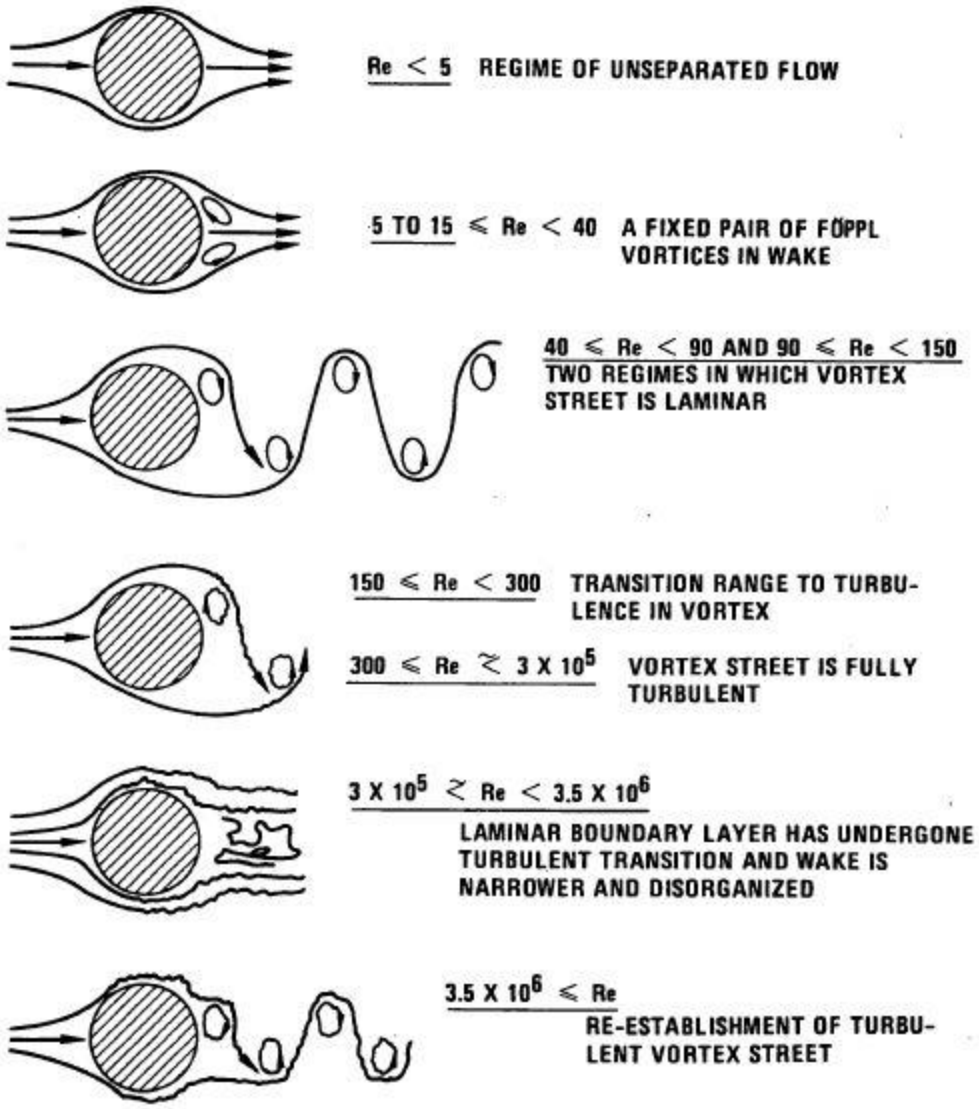

Figure 6 Regimes of Fluid Flow across Smooth Circular Cylinder (Lienhard, 1966)

In the past few decades, VIV has been extensively studied and many studies on VIV of a circular cylinder can be found in the comprehensive reviews [30-46]. The early numerical studies accommodate models of rigid cylinders elastically mounted or forced to vibrate in the cross-flow at low Reynolds numbers. Most papers on VIV have reported bluff body vibrations for the range of reduced velocities, defined as the inverse of the natural frequency of the body normalized by the free stream velocity and characteristic diameter of bluff body. In this range called lock-in

range, the body oscillation frequency is the same as the unsteady wake frequency and the body response amplitude exhibits a bell-shaped evolution as a function of the reduced velocity. It was shown by Gsell et al. that the body oscillations depend on the mass ratio between the body and the fluid as well as the structural dumping. The cross-flow response of the body oscillations can be significantly altered by adding a degree of freedom in the direction aligned with the flow (stream-wise direction) [30]. Experiments by Jauvtis and Williamson reported an amplification of the cross-flow vibration with amplitudes up to 1.5 diameters [31]. Several recent experimental studies [31-33] have also observed increase of the body response oscillation frequency during the in-line degree of freedom VIV. These studies have documented that the in-line VIV can lead to higher fatigue damage than the cross-flow VIV due to the doubled oscillation frequency. Previous computational studies on the VIV of bluff body were mostly based on the two-dimensional (2-D) models. Guilmineau and Queutey reported results of 1-DOF VIV of a circular cylinder, the VIV response was well captured in the initial and lower branches. However, the response in higher branches failed to match up to the experimental results [34]. It was found that the flow in the wake of a circular cylinder becomes 3-D when the Reynolds number exceeds 200 [35, 36] and thus, it is necessary to apply a 3-D model for numerical studies on VIV. In the most recent study by Wang et al., 2-DOF VIV response of circular cylinder with in-line to cross-flow natural frequency ratios $f^* = f_{nx}/f_{ny}$ was studied numerically using 3-D CFD simulations. They reported that the normalized amplitude, *A/D*, increases and shifts to a higher reduced velocity (V_r) when f^* increases from 1 to 2. When the in-line mass ratio equals to the cross-flow mass ratio, a single peak was observed for $f^* = f_{nx}/f_{ny} = 2$ [37]. Gsell et al. have simulated 2-DOF VIV of a circular cylinder at Reynolds number of 3900 using direct numerical simulation by solving 3-D Navier-Stokes equations. The predicted structural responses and forces were

consistent with the experimental results reported by Jauvtis and Williamson [30, 31]. The numerical results of this study confirmed the large-amplitude of cross-flow VIV and the shape of the responses. Majority of the VIV studies are still focusing on the cross-flow VIV as the cross-flow response amplitude is much larger than in-line response. Although there are large number of existing numerical studies focused on 1-DOF cross-flow VIV of a circular cylinder [38-42], the cylinder used as the bluff body is either stationary or the induced vibrations/oscillations of the cylinder was not being taken into consideration. In other words, the fluid part and solid structure was not fully coupled. As a result, the characteristics of the obtained velocity field are not accurate enough, which may underestimate the VIV response. Vortex shedding results in fluctuating forces exerting on the bluff body and may induce vibrations when the bluff body is elastically mounted or deformable [43, 44]. This vibration/oscillation of bluff body further alters vortex formation and shedding in return. The accurate prediction of the interaction between fluid and solid structure requires multi-physics coupled numerical simulation that involves the data exchanging between the fluid flow and structural mechanics.

A recent review by Rostami and Armandei classifies the vortex induced phenomena into two main groups resulting in either mechanical oscillations or rotation [45]. The authors also provide evidence that the most promising in terms of energy extraction efficiency versus cost are the oscillatory extracting devices based on buffeting or VIV. Buffeting is a type of vortex induced motion produced by the unsteadiness of the incoming flow, which may be caused by natural turbulence, or by the presence of the wake of upstream objects. The unsteadiness in the uniform flow is created by a blunt bluff body and the oscillations owing to the Von Kármán vortex street (wake buffeting) are extracted by a second elastically mounted body which is positioned downstream [46]. Armandei and Fernandes have studied a preliminary unit turbine

model based on the buffeting phenomenon. The proposed turbine model consists of an elastic rectangular flat plate positioned downstream of a cylindrical bluff body that was tested in a laboratory flume. The results demonstrate that such system can extract hydrokinetic energy with efficiency of up to 60% [47]. This methodology might be one of the possible solutions to further improving the performance of the proposed energy harvester.

In CFD studies regard to turbulence modeling, there are two main categories of turbulence models. The first one is so called Reynolds Averaged Navier-Stokes (RANS) model, which are widely used nowadays. The second one are direct numerical simulation (DNS) and large eddy simulation (LES), which are proven to have the potential to model turbulence in a much more general and better way than RANS models. Complexity of different turbulence models may vary strongly depending on the details one wants to observe and investigate by carrying out such numerical simulations. Complexity is due to the nature of the Navier-Stokes equations (N-S equations). N-S equations are inherently nonlinear, time-dependent, three-dimensional partial differential equation (PDE). The Spalart-Allmaras one-equation turbulent model is the simplest RANS model, which was designed specifically for aeronautics and aerospace applications involving wall-bounded flows [48]. Two equation models are by far the most widely used turbulence model. Typical examples of such models are $k-\omega$ and $k-\epsilon$ models in their different forms. These models simplify the problem to the solution of two additional transport equations and introduce an eddy-viscosity model to compute the Reynolds stresses. The draw-back of the $k-\omega$ models is their insensitivity to adverse pressure gradients and boundary layer separation. They typically predict a delayed and reduced separation relative to the experimental observations, which makes the $k-\epsilon$ model not adequate for the studies involving flow separation problem. On the other hand, $k-\omega$ models are typically better at

predicting adverse pressure gradient changes in boundary layer flows and flows with mild to massively separated regions. Furthermore, the $k-\omega$ Shear Stress Transport (SST) model has been calibrated to accurately compute flow separation from smooth surfaces. For turbulent flow over a circular cylinder, the strong and typical span-wise flow effects along with generation of large scales eddies in the separated region aft of the cylinder makes it favourable for hybrid RANS-LES methodology such as Detached Eddy Simulation (DES) [49] and Delayed Detached Eddy Simulation (DDES) [50]. The DES approach was proposed by Spalart et al. in 1997 [49]. The original DES proposed combines the RANS and LES in a non-zonal manner. DES is based on the Spalart-Allmaras one equation turbulence model [50]. Length scale, *d*, is generally taken as the shortest distance at any point to the closest wall in RANS model. In DES, it is replaced with the minimum between the distance to the wall and a length proportional to the local grid spacing. It is represented mathematically as

$$d_{DES} = \min(d, C_{DES}\Delta) \tag{4}$$

where C_{DES} represents a model constant taken as 0.65 in different studies [49]. Δ is the local grid spacing. For structured grids, it is the maximum grid spacing over all three directions. For unstructured grids, it is generally taken as the maximum edge length connecting the centroids of the adjacent cells. The main idea of DDES is to include the molecular and turbulent viscosity information into the switching mechanism to delay this switching in boundary layers [51].

Durrani [51] reported three common cases including URANS, DES and DDES for high Reynolds number flows over circular cylinder at Reynolds number of 1.4×10^5 and 8.0×10^6. It was found that, the shedding frequency, pressure distribution, drag and lift coefficients of the simulated results from hybrid RANS-LES model match well with the experimental work by

Roshko [52] and Von Nunnen [53] as well as some other numerical studies [54]. The computed Reynolds stresses also provide satisfactory comparison with the experimental results by Cantwell [55], which is very encouraging from the perspective of the applicability of hybrid RANS-LES methodology for massively separated flow at high Reynolds numbers.

2.2 Reviews on Existing Technologies

Because of global climate change, innovative renewable energy systems are urgently required for energy harvesting. Chaaban et al. point out that the increase in energy consumption with all its polluting consequences has made environmental issues one of the main concerns of decision makers, engineers and scientists. Chaaban et al. maintain that renewable energy resources can offer an attractive, cleaner alternative to reduce the impact of electricity generation and transportation [56]. Solar panels and wind turbines are well developed renewable systems, commercially applied, but almost 70% of the Earth's surface is covered with water. According to Harries et al., tidal power and hydro-electricity have become mature technologies in Australia, but there are few opportunities for further exploitation of Australia's relatively limited potential for hydroelectric development, begun over a century ago. Australia has not yet fully developed its conversion technology for the large amount of available ocean wave energy [57].

Bernitsas et al. [58] patented a most significant work to harness energy from the VIV phenomenon. Their energy converter called VIVACE (Vortex Induced Vibration Aquatic Clean Energy) is a passive circular cylinder with upward-downward motion induced by vortex shedding. This passive cylinder is mounted on springs and is designed to generate electricity in a range of flow velocities. The VIVACE system converts mechanical energy into electricity via rotary or linear generators [59]. The scope of the design of VIVACE is to harness hydrokinetic

energy from river currents with a uniform velocity as low as 0.4 m/s. Ding et al. [60] recently reported numerical simulations as well as experimental validation for energy harvesting by a single – cylinder VIVACE converter with passive turbulence control. In this study, the circular cylinder is geometrically modified using straight roughness strips placed on cylinder surface for the purpose of enhancing the flow induced motion. It has been shown that different parameters of the roughness can affect the properties of the flow induced motion, including the roughness location, the roughness height, and the roughness coverage [61 - 63]. Passive turbulence control (PTC) was developed to use the roughness strip, and the physical model was tested in the lab. The results show that when the strip thickness is about equal to the thickness of the boundary layer, the PTC has the greatest effect on the flow induced motion [62]. The proposed model is studied using two-dimensional Unsteady Reynolds-Averaged Navier-Stokes (2-D URANS) simulations and results are validated by experimental data. For flow speed in the range of 0.4 m/s to 1.6 m/s, the result shows that the potential power output of this proposed harvester can reach up to 21 W. With the PTC, the VIVACE converter will be able to extract the hydrokinetic energy from currents over the entire range of FIM synchronization. Energy conversion efficiency can be increased to 37% in the simulations and 28% in experiments as reported by Ding et al. [60].

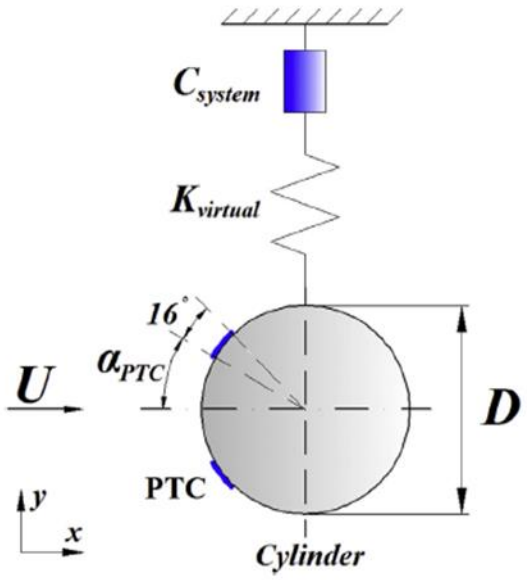

Figure 7 VIVACE Convertor (Ding et al., 2014)

So far, the power converters used to generate electricity from the VIV are mostly based on the electromagnetic generators. A simple model of such electromagnetic vibration generator consists of an LR circuit with the impedance of the coil in series with the load resistance. The vibration transmitted from the base excitation by the VIV makes a relative translational movement of the magnet in relation to the coil. This relative oscillating motion causes a variation magnetic flux inside the coil, and the voltage induced in the coil can be determined by Faraday's law. Liu et al. [63] developed a multi-frequency electromagnetic energy harvesting device which consisted of a permanent magnet and a circular suspension structure on an energy harvesting chip. It was shown that the magnetic flux changes and power output ability can be improved by adjusting the distance between the magnet and the chip. Dung et al. [64] developed an electromagnetic energy harvester for harnessing energy from vibration induced by Karman Vortex Street. This harvester converts flow energy into electrical energy by fluid flow and vortex shedding from a trapezoidal bluff body and electromagnetic induction. The periodic vortex

shedding behind the bluff body immersed in a steady stream causes a pressure oscillation in the stream. Their experimental results show that an output peak-to-peak voltage of nearly 20 mV in average when the excitation pressure oscillates with an amplitude of 0.3 *kPa* and a frequency of 62 *Hz*. Figure 8 shows the operation of their proposed energy harvester.

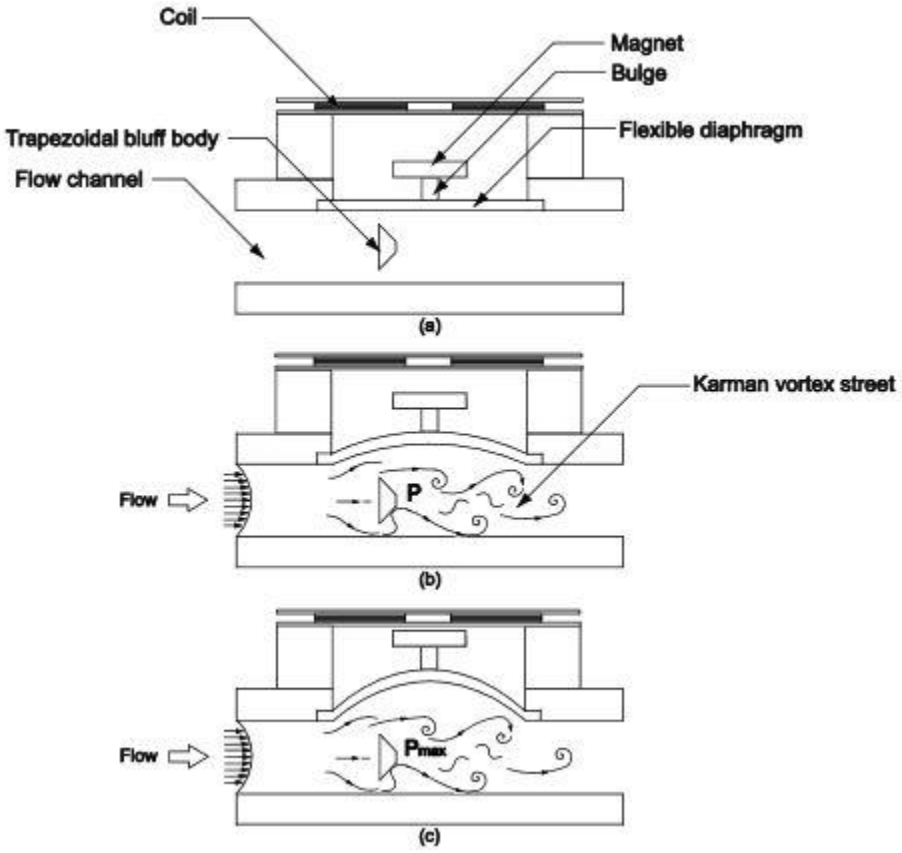

Figure 8 Operation of Electromagnetic Harvester (Dung et al., 2012)

The selection of the power convertors is a serious challenge because of the random and broadband characteristics of ambient VIV vibrations. The feasibility of piezoelectric generators has been explored in other studies also. Piezoelectric materials can be used as a means of transforming the vibrations into electrical energy that can be stored. Piezoelectric generators are highly efficient, inexpensive to make, and pollution-free. Recent studies have shown that

piezoelectric generators perform much better at low-level vibrations, which makes them suitable for the application of energy harvesting from natural water flow [65, 66]. The electrical energy produced by these materials is far too small to power an electrical device. Thus, many studies in energy harvesting have focused on methods of accumulating and increasing the amount of energy generated.

In several studies, power generator array were designed to improve the power output performance. Liu et al. [67] investigated a power generator array based on thick-film piezoelectric cantilevers to improve frequency flexibility and power output. The piezoelectric cantilevers array can be tuned to a certain frequency and can expand the excited frequency bandwidth in ambient low frequency vibration. The prototype generator has a measured performance of 3.98 μW effective electrical power and 3.93V DC output to resistance load. Chen et al. [68] proposed an electrical generator with a novel structure which uses one dimensional piezoelectric cantilever beams. It was found that the width of the vibration and band gap can be increased with the mass. In order to improve the power output of the piezoelectric transducer, Roundy et al. [69] used a multi degrees-of-freedom bimorph system which consists of a piezoelectric beam with three masses and four springs. This system improved the bandwidth of the harvester from 6 *Hz* to 24 *Hz*, and it was also shown that the total energy output increases as there is no frequency tuning of the actuator. Optimization of energy harvesting devices has also been investigated by researchers for the purpose of higher conversion efficiency. In Sodano et al.'s recent studies [65], three types of piezoelectric devices are investigated and experimentally tested to determine their abilities to convert vibrations into electrical energy respectively. The three types of piezoelectric devices are the monolithic piezo-ceramic material lead–zirconate–titanate (PZT), the bimorph Quick Pack (QP) actuator, and the macro-fiber composite (MFC).

The experimental efficiency of these three devices was compared as well as their feasibility in practical applications. Lefeuvre et al. [66] proposed a nonlinear approach to optimize the power flow of vibration-based piezoelectric energy-harvesting devices. This self-adaptive principle is based on a particular synchronization between extraction of the electric charge produced by the piezoelectric element and the system vibrations, which maximizes the mechanical to electrical energy conversion. Theoretical predictions confirmed by experimental results show that the new principle increases the harvested power by 400% as compared with a quasi-linear impedance adaptation optimization method.

CHAPTER 3

MATHEMATICAL MODELING

3.1 Computational Methodology

CFD modeling serves as an important step for designing and optimizing the harvester. The geometry of the harvester was determined and optimized based on the combination of 2-D CFD numerical simulation in commercial software ANSYS^{TM} and analytic harmonic modeling in MATLAB. After the optimum geometry was selected, 3-D tow-way coupled FSI simulations of the harvester in water flow were conducted in ANSYS^{TM} to study the 2- DOF VIV response. The drag (C_d) and lift coefficients (C_l), longitudinal and lateral displacements, and frequency responses of the harvester were reported and compared with the stationary model. Next, the vibrational energy of the harvester extracted from the fluid flow was used to estimate the power output of the harvester. Furthermore, two-way coupled FSI simulations at high Reynolds number were also conducted to further investigate the potentials of harvesting kinetic energy from flowing water. In this chapter, important quantities involved in mathematical modeling including Strouhal number, energy density and the details of harmonic modelling of the harvester were introduced. The detail of CFD modeling will be discussed in Chapter 4.

3.2 Vortex Shedding of Circular Cylinder

The frequency and amplitude of the VIV response of the bluff body are the most important factors than can determine the conversion efficiency when it is for the purpose of energy harvesting. The geometry of the bluff body plays a crucial role for utilizing VIV response. The studies on FIM of circular cylinder confirm that flow asymmetry caused by body geometric

asymmetry, attachments, or upstream flow disturbance may cause excitation in a circular cylinder [70]. Recent experimental studies demonstrate that the FIM is highly dependent on the cross-sectional geometry and the angle of incident flow. It was found that the amplitude of oscillation of bluff bodies with circular cross-section is substantial compared to other geometries with equivalent characteristic dimensions. A large number of researches use circular cylinder as bluff body to study the vortex shedding phenomenon, whose VIV response is simple and typical. The drag on such structures often leads to large in-line vibrations that may be beneficial for energy harvesting purpose [25-27]. On the other hand, the symmetric and smooth geometry of the circular cylinder leads to strong and periodic vortex shedding.

3.3 Strouhal Number

Strouhal number (***St***) is the dimensionless quantity that describes the oscillating flow mechanisms of the system, which is the predominant frequency of vortex shedding multiplies with the diameter of the cylinder divided by the free stream velocity,

$$S_t = \frac{f_s D}{U} \tag{5}$$

where f_s is the vortex shedding frequency in unit of *Hz* (cycle per second), *U* is the free stream flow velocity approaching the cylinder, and *D* is the diameter of cylinder. Experiments have shown that the oscillations in lift force (force perpendicular to the flow) occur at the shedding frequency, but oscillations in the drag force (force parallel to the flow) occur at twice the shedding frequency.

The Strouhal number of a stationary circular cylinder in a subsonic flow is a function of Reynolds number, as shown in Figure 9. In the transitional regime, $2 \times 10^5 < Re < 3.5 \times 10^6$, Achenbach and Heinecke [24] found that for smooth surface cylinder has a chaotic, disorganized, high-frequency wake and Strouhal numbers as high as 0.47, while rough surface cylinders has organized, periodic wakes with Strouhal numbers of $St \cong 0.25$. Overall in the transitional range, vortex-induced vibration of circular cylinders generally occurs at $St \sim 0.2$.

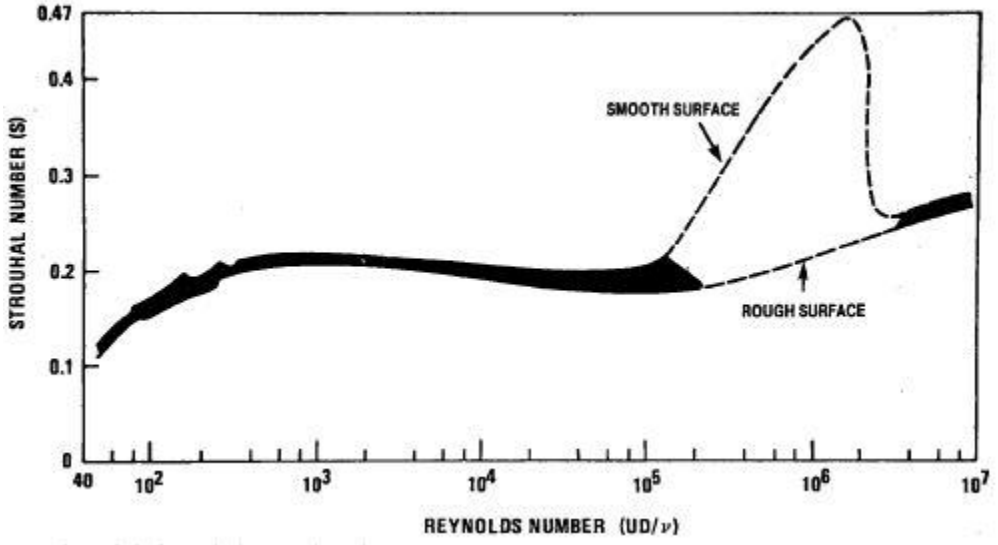

Figure 9 Effect of Reynolds Number on Strouhal Number for Circular Cylinder [Blevin, 1977]

3.3 Harmonic Model

The equations of motion for the cylinder oscillating in a fluid flow in x and y-direction are given by

$$m\ddot{y} + c_s\dot{y} + k_s y = F_L(t) \tag{6}$$

$$m\ddot{x} + c_s\dot{x} + k_s x = F_D(t) \tag{7}$$

where c_s is the dumping coefficient and k_s is the spring stiffness. Figure 7 shows that the centre of the cylinder is attached to an immobile support. There are four spring-damper systems installed in the cylinder. The oscillating mass, m, includes the mass of the cylinder and the mass of spring damper systems given by

$$m = m_{cylinder} + m_s \tag{8}$$

System damping includes structure damping, which is the energy loss caused by dissipation in the transmission system, and $c_{harvest}$ is the "damping" coefficient which represents the net amount of energy harvested/converted to electrical energy.

$$c_s = c_{structure} + c_{harvest} \tag{9}$$

As it is shown in Figure 10, the proposed harvester consists of a circular, hollow cylindrical bluff body with four spring-damper mechanisms, and each piezoelectric harvester attached to the spring-damper mechanisms respectively. Thus, the hydrokinetic energy of the water flow is converted into electrical energy directly by using piezoelectric materials.

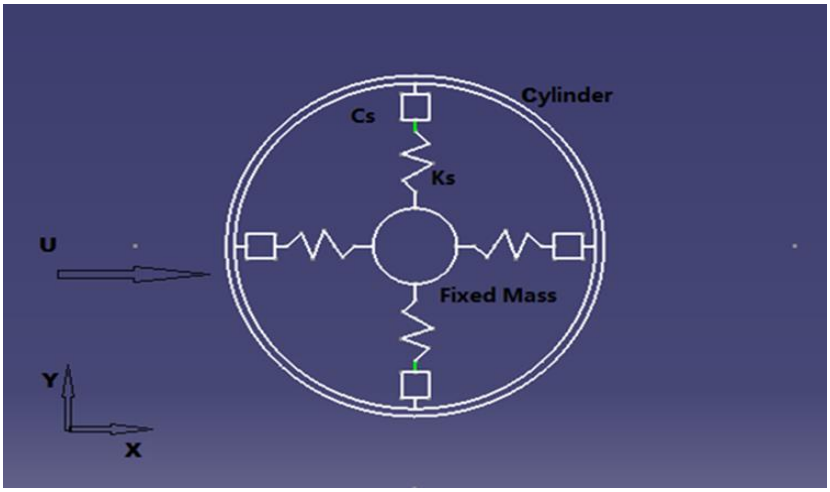

Figure 10 Schematic of the Proposed Harvester

3.4 Energy Density

In this section, a quantity known as energy density is introduced to obtain a design approximation of the resonant response of the piezoelectric energy harvester. Energy density is defined as a squared product of oscillation frequency and amplitude, which is proportional to the amount of mechanical energy available to be extracted from the fluid flow. Eqs.10 - 12 illustrate the relations between energy density and the kinetic energy stored in the flow. The in-line and transverse displacements of the cylinder were obtained from the two-way coupling FSI simulations and then energy density of each case was calculated to compare and optimize the performance of the proposed harvester. The details of the energy density for different cases will be reported in Chapter 5.

$$y = A\sin(\omega t) \tag{10}$$

$$\dot{y} = \omega A\cos(\omega t) \tag{11}$$

$$E_k = \frac{1}{2}m\bar{v}^2 = \frac{1}{2}m\omega^2 A^2\overline{cos^2(\omega t)} = \frac{1}{4}m\omega^2 A^2 \tag{12}$$

In order to predict the displacement of the proposed harvester, information for the drag and lift forces is required. The approach undertaken in this study is to use numerical simulations to extract the time variation of the drag and lift coefficients. This methodology is explained in the next section.

CHAPTER 4

COMPUTATIONAL, STRUCTURAL AND EXPERIMENTAL SETUP

4.1 Computational Setup

In this chapter, the computational, structural setup of the numerical modelling and the experimental setup were reported in details. There are three computational models involved in this chapter, which are 2-D preliminary model, 3-D stationary model and 3-D two-way coupled model. The information including mesh structures, boundary conditions were reported in the first section. The second section describes the setup of the structural model of the 3-D two-way coupled simulation. The last section of this chapter discusses the setup of the experimental work, including the process of implementation and uncertainty analysis.

4.1.1 2-D Preliminary model

In many engineering applications, complex 3-D flows can be simplified as 2-D under appropriate assumptions. Since the purpose is to harvest the kinetic energy of the water flow in rivers as such, the length of the cylinder is assumed to be relatively large. Thus, for design purposes, 2-D numerical model was initially built to investigate the correlation between the diameter of the cylindrical bluff body and its VIV response behavior, thus, optimum diameter of the bluff body can be determined for a specific range of free stream flow velocity. VIV response behavior of bluff bodies with different diameter was studied by monitoring the time evolution of the lift and the drag coefficients and calculating the fluid forces acting on the body. The CFD simulation is developed and implemented with commercial software ANSYS^{TM} Fluent. In each simulation, the diameter of the cylinder was varied from 0.05 m to 0.20 m at uniform flow

condition with free stream flow velocity of 1 m/s. The Reynolds numbers based on the diameter of the cylinders vary from 5×10^4 to 2×10^5, which is mostly in the subcritical regime.

To predict the characteristics of unsteady flow separation correctly, fine mesh is required. Especially around the boundary of the cylinder, the mesh has to be fine enough to obtain accurate approximation. The computational domain was separated into three sub-domains to keep the appropriate mesh density closer to cylinder and coarser elements far away from the cylinder to the reduce calculation effort. The size of the computational domain was selected to be 10D wide and 15D long. The fluid domain includes five boundaries: flow inlet, flow outlet, two side walls and the cylinder boundary. The circular cylinder is positioned at the specific location inside the domain, which is 5D away from the sidewalls and 5D downstream of the flow inlet. At the flow inlet, the boundary condition is velocity inlet with uniform fluid flow velocity of 0.2 m/s to 1 m/s. At the flow outlet, pressure outlet boundary condition is assigned and a zero pressure gradient condition is specified at the outlet boundary. The side walls are specified as symmetry boundary, which assumes the cylinder is submerged in the mid-depth inside the fluid environment. The boundary of the cylinder is defined as stationary non-slip wall.

Figure 11 shows the mesh structure inside the domain. The meshing is constructed in ANSYS^{TM} Fluent ICEM workbench. Edge sizing and inflations layers have been applied to the cylinder boundary so that the grid around the cylinder is uniform and finer than the global mesh elsewhere. In detail, the cylinder boundary was assigned to be the target edge and being divided into 40-50 small pieces based on the size of the cylinder. Since the inflation layers depend on the diameter of the cylinder, it is desirable to include between 15 and 20 layers around the boundary of the cylinder to predict the flow separation accurately. The first layer thickness option was

selected, thus detail dimension for the first layer, the growth rate throughout the layers and the total number of layers can be altered based on the size of the cylinder. Quadrilateral elements are used for the inflation layers that surround the cylinder and triangular elements are used for the rest of the computational domain. The laminar viscous model was used in 2-D preliminary model because the Reynolds number lies in the subcritical regime, which the laminar separation is the dominant near the cylinder's boundary. As the number of the elements used to approximate the continuous solution increases, the accuracy of the numerical model used to calculate the actual solution also increases. Multiple simulations were performed with an increasing number of mesh elements to ensure mesh independent solution. The drag coefficient was monitored throughout. It was found that the minimum number of elements required for a mesh-independent solution is in the order of 65,000 elements. Figure 12 shows that at lower mesh density, the average value of drag coefficient fluctuates, and becomes stable at ~ 65,000 elements.

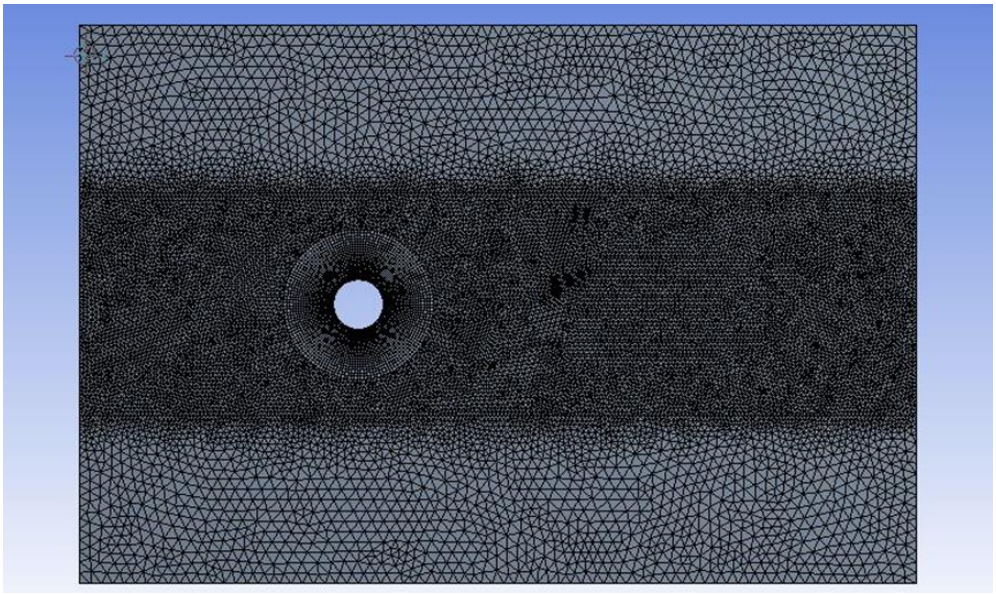

Figure 11 Mesh Structure of 2-D Simulation

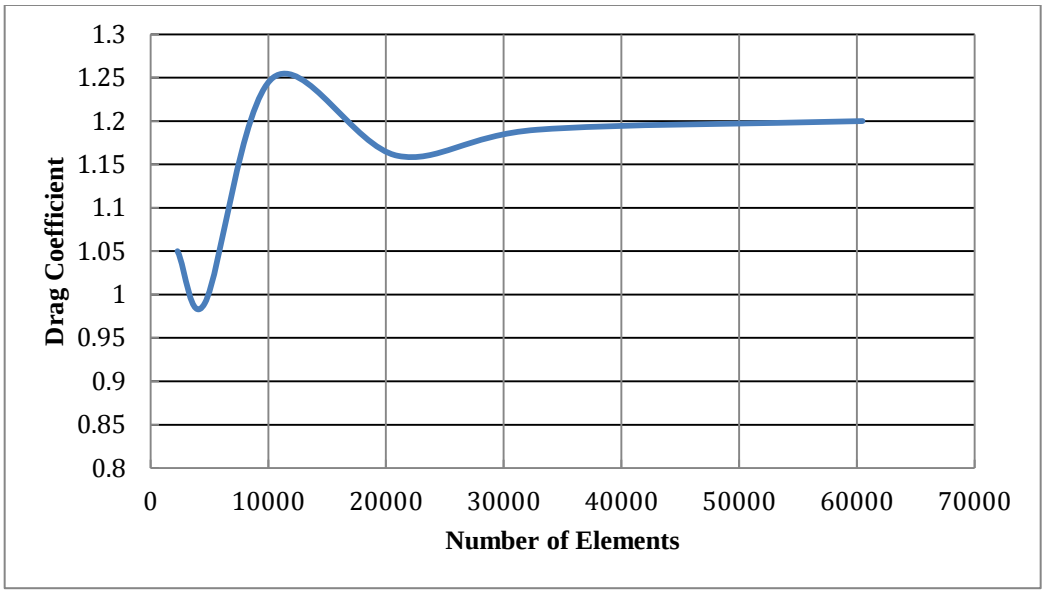

Figure 12 Drag coefficient (C_d) vs Number of Elements for Cylinder with D = 0.2 m

In order to determine the optimal diameter for the proposed harvester, the drag and lift coefficients and forces are compared between different cases. Once the computations reach steady state, the drag and lift coefficients and the corresponding forces exerted on the cylinder are extracted. These forces are then applied to the spring-damper mechanical system of the harvester. The equation of motions of the spring-damper mechanical system under fluid excitation forces was simulated numerically using MATLAB, and the displacement and velocity along X and Y directions were calculated. The lift force acting in the Y-direction moves the cylinder transversely to the water flow. The frequency and amplitude of the oscillations of the harvester result from the unsteady fluid forces are used to estimate the amount of energy that can be harvested. The detailed numerical results and comparison are discussed in the next section.

4.1.2 3-D Stationary Cylinder Simulation

The setup of 3-D numerical simulations of a stationary circular cylinder is presented in this section. Turbulent models were applied into the simulations to study the turbulent flow structure of the near wake. The numerical results of the simulation for stationary (rigid) cylinder are compared with 3-D two-way coupled model in the next section to investigate the significance of FSI simulations. The experimental and numerical study of high Reynolds number turbulent flow past a circular cylinder remains one of the most active areas of research in fluid mechanics. Large number of studies have proven that for turbulence modeling separated flows such as the flow past a circular cylinder [71], RANS models and $k-\omega\ SST$ model developed by Menter et al [72, 73] possesses the best overall performance in terms of predicting the mean surface pressure coefficient distribution(C_p), the mean drag coefficient ($\overline{C_d}$), the mean streamline profiles in some characteristic plane (symmetry plane of the cylinder) when compared with the LES model which requires very fine computational mesh. Numerical flow analysis at high Reynolds number over a circular cylinder by applying DES and DDES models has also good agreement with the experimental data as reported in [51-55]. Many researchers have studied performance of RANS-based turbulence models (mainly $k-\omega$ models) applied to external flow around the cylinder. It is possible to fully resolve for the turbulent flow around circular cylinder by applying DNS.

DES is a hybrid model including the benefits of both the Reynolds averaged Navier-Stokes (RANS) model near the walls and the LES model formulated for the regions away from the walls. A DES is an LES model that switches to a RANS-based model near the wall boundary, thus permitting a relatively coarse grid near solid boundaries. In the regions, where the turbulent

length scales are less than the maximum grid dimension are assigned to the RANS model. As the turbulent length scale exceeds the grid dimension, the regions are solved by using the LES model. Therefore, the grid resolution is not as demanding as pure LES, thereby considerably cutting down the cost of the computation.

Numerical simulations with both of these two turbulent models are studied and compared. By performing a simulation of the stationary cylinder prior to the two-way coupled model, the most suitable turbulent model was determined. Numerical simulations with $k-\omega\ SST$ model were considered here for comparison purpose. The boundary conditions and y^+ value remain the same for all calculation/simulations. The density of the mesh gradually increases as the Reynolds number goes up to ensure the accuracy of the calculation. The time-averaged drag and lift coefficients, velocity and vortices contours were reported for comparison. By comparing with the published experimental results [74] as reported in Fig.13, the numerical results of DES model have good agreement in terms of averaged drag coefficient. Table 2 presents a quantitative comparison of the drag coefficient for two turbulence models, it can be concluded that DES model has the better performance when evaluating the $\overline{C_d}$ value for wide range of Reynolds number.

Table 2 Comparison of Mean Drag Coefficient for Two Turbulence Models

Reynolds Number	Number of cells	Time step (s)	DES		$k-\omega\ SST$	
			$\overline{C_d}$	C_l	C_d	C_l
8.8×10^4	85050	0.005	1.013	0.8629	0.4107	0.0816
2.0×10^5	92654	0.005	0.875	0.4813	0.3352	0.0395
3.5×10^5	102,454	0.001	0.2835	0.332	0.2852	0.0037
7.1×10^5	120,489	0.001	0.2657	0.2677	0.2466	0.0031
1.5×10^6	140,587	0.001	0.3913	0.1268	0.3889	0.0024

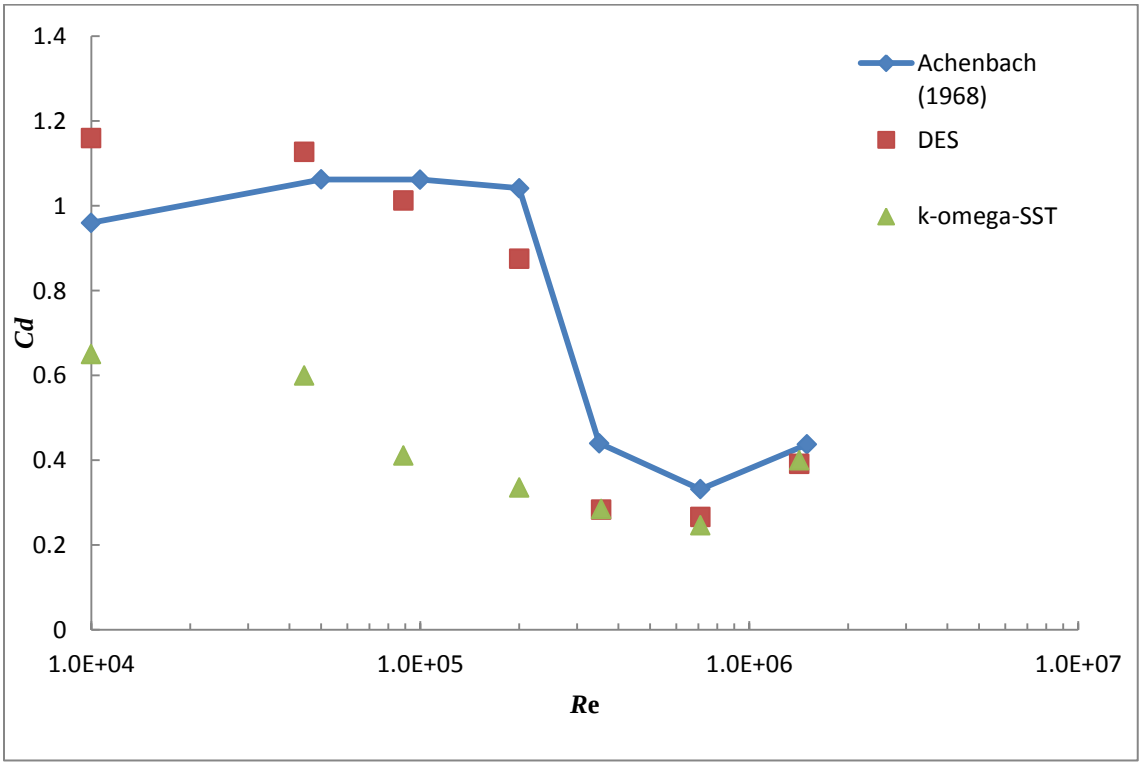

Figure 13 Drag coefficient vs Re of Two Models and Published Experimental Work

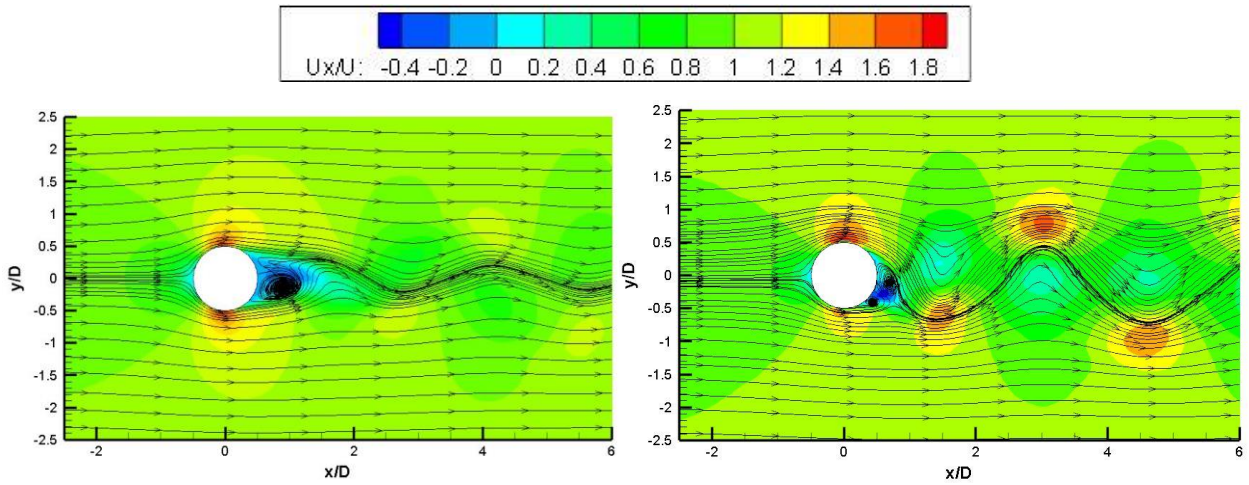

(a) $k-\omega$ SST (b) DES

Figure 14 Instantaneous Stream-vise Velocity Contours for Two Viscous Models

(a) $\mathbf{k-\omega}$ SST (b) DES

Figure 14 represents the instantaneous stream-wise velocity contours with streamlines in the center plane of the domain for two turbulence models. It is clear that the similar wake structure can be observed for the DES model and the $k-\omega\ SST$ model, however, the vortex street of DES model is obviously stronger where higher velocities are detected. Difference exists in terms of streamlines, in the near wake region. DES model in Figure 14 (b) shows that two swirling vortices/ spiral centers exist behind the cylinder, one clockwise vortex core caused by the downwash flow and located in the upper region and another counter-clockwise vortex core induced by the very weak up-wash flow and located in lower region. But no such vortex phenomena can be captured in Figure 14 (a) for the $k-\omega\ SST$ model.

Overall, these findings suggest that DES provides a more accurate prediction of the features for turbulent flows around circular cylinder for a wide range of flow conditions and Reynolds number compared with RANS-based models and at the same time alleviates grid

resolution requirements of the LES close to the boundary. Thus, DES model was selected to be the turbulence model for the two-way coupled FSI model.

4.1.3 3-D Coupled FSI Simulation

In order to further investigate the actual behavior of the proposed harvester in the fluid flow, 2-DOF VIV of a circular cylinder is studied by using 3-D two-way coupled FSI simulations. In order to eliminate the effect of the buoyancy force, the density of the material is set to be the same as the density of water. Possible edge effects in the simulation were eliminated by selecting the length of the cylinder to be exactly the same as the thickness of the fluid domain. Figure 15 shows the isometric view of the fluid domain, which has dimension of $10D \times 15D$. The cylinder is at the location where is $3D$ away from the inlet along the stream-wise direction and $5D$ from top and bottom wall along transverse direction.

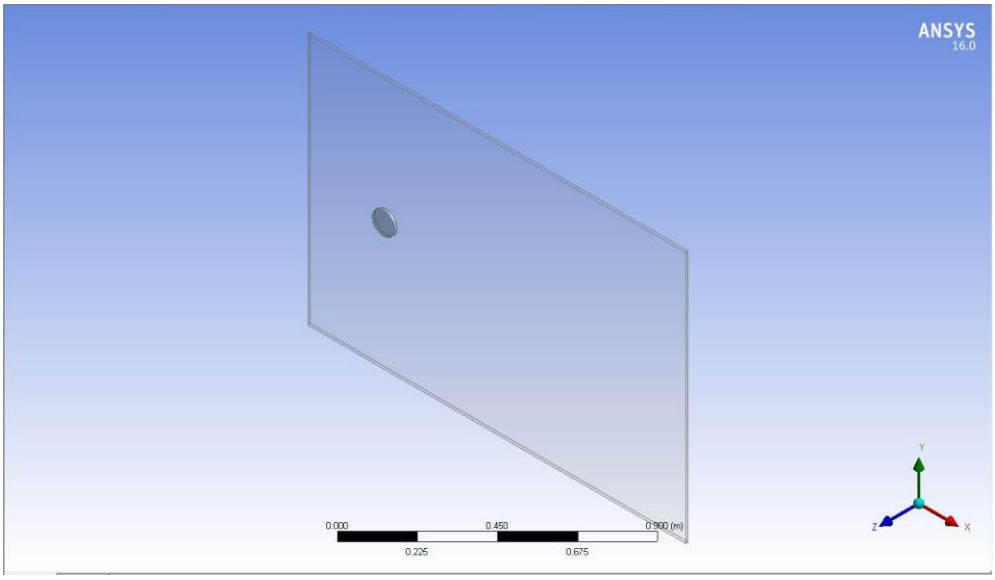

Figure 15 Computational Domain

Figure 16 represents the mesh structure of the fluid domain. The dominant structure was meshed with tetrahedral elements which are recommended to accommodate the dynamic meshing. The higher grid resolution is also required to acquire mesh independent results. Body sizing function was applied to the computational domain to adjust the optimum element size for a mesh-independent solution with least computational effort. Boundary conditions of each surface are reported in Table C. 3 in Appendix C. The boundary of the cylinder is assigned to be non-slip wall. The flow inlet is a velocity inlet with turbulence intensity of 5%. At the outlet boundary, the gradient of the fluid velocity in the stream-wise direction is set to zero and the pressure at the outlet is being assigned at a reference pressure $P = 0\ P_a$. The two transverse boundaries which are parallel to the flow direction, top and bottom surfaces of the computational domain were treated as symmetry walls.

In order to obtain accurate solution and capture the near wall flow physics when conducting CFD calculations, the boundary layers in wall bounded flows is crucial to be properly resolved. Thus, edge sizing and inflation functions were applied to the boundary layer of the cylinder. Depending on the inlet boundary condition, the edge sizing was set to have 50 to 60 points along the boundary of cylinder. The inflation layers contain 15-25 quadrilateral layers, with first layer thickness of 0.002 m and growth rate of 1.1. The advantage of adopting the inflation layers is to have sufficiently fine mesh to adequately capture regions where the flow will experience rapid change in key variables such as pressure and velocity. Due to the fact that this is a two-way coupled simulation, the regeneration of dynamic meshes requires lots of computational resources. On the other hand, those quadrilateral inflation layers are not affected by as flexible as the tetrahedral elements, thus the inflation layers are set to display with the cylinder during the coupled simulations. In this way, high resolution quadrilateral elements can

be applied to the boundary layer of cylinder without the consideration of consuming too much time for completing the calculation.

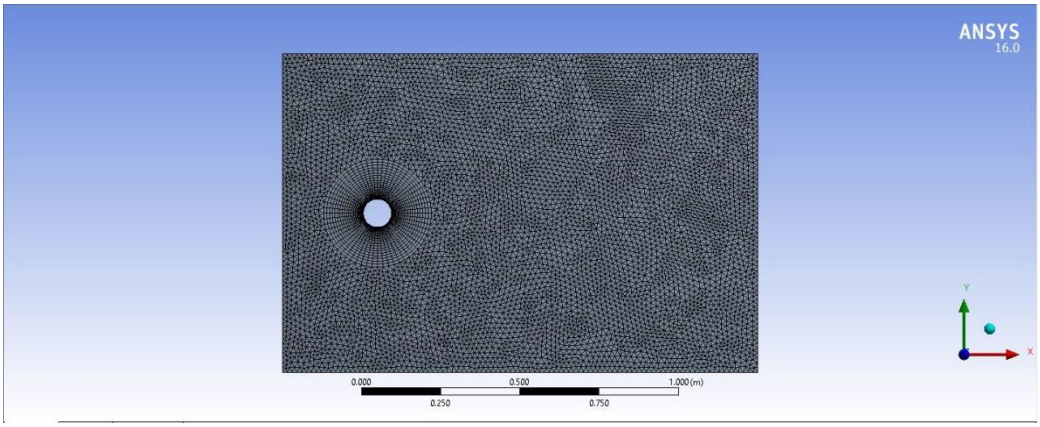

Figure 16 Mesh Structure of Two-way Coupled Simulation

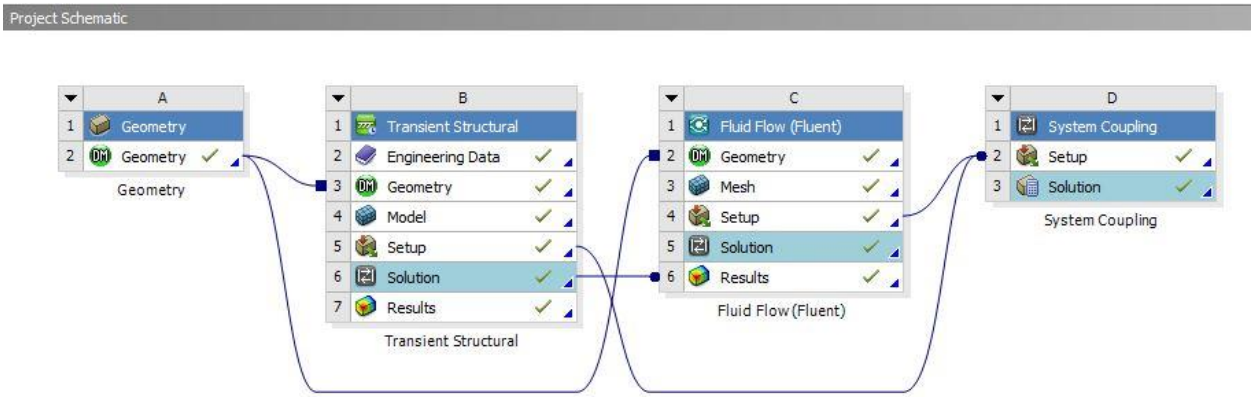

Figure 17 Project Schematic of Two-way Coupled Simulation

Figure 17 shows a schematic of the coupling strategy of the current FSI simulations. The current fluid-structure interaction problem was solved using the system coupling solver in commercial software ANSYS V16.0. Transient structural module and Fluid Flow (Fluent) module are coupled in two-way data transfer controlled by the system coupling, and they are sharing the same geometry. Outline of solver settings, data transfer settings, execution control,

solution information and chart monitors are provided in the Appendix B. In analysis settings, the duration control is defined by the end time. The coupled simulation has step size of 0.001s, with minimum iterations of 1 and maximum iterations of 30 within one time step. Two -way data transfer processes can be configured in the system coupling settings. The selected participants are the Transient Structural module and Fluent module. For the first data transfer process with the source being the Transient Structural module, the incremental displacement of the cylinder will be transferred to the target region, which is the cylinder‘s interface in Fluent. The second data transfer process is taking the forces from the region of cylinder’s interface, which calculated in Fluent and transfer back to the Transient Structural. For 15 seconds of duration with step size of 0.001s, there are 15000 coupling steps in total. In execution control, the co-simulation sequence is set to select Fluent to run first. During each coupling step in two-way coupled simulation, Fluent starts to run first and then the forces acting on the interface are calculated and transferred to the Transient Structural module. Mechanical APDL solver in Transient Structural module takes the force and calculates the incremental displacement then transfers the information back to Fluid Flow (Fluent) through the data transfer process. Finally, Fluid Flow (Fluent) software takes the displacement and updates the solution. If the convergence criteria are met, the coupling simulation will then continue to next coupling step.

In Fluent, the calculation was carried out with pressure-based solver. The gravity function is enabled with gravitational acceleration of -9.81 $\frac{m}{s^2}$ along transverse direction. Based on the numerical results from simulations of 3-D stationary cylinder, DES is more capable of predicting the VIV phenomenon for this case compared with $k-\omega\ SST$, thus DES turbulence model was selected for simulations with higher Reynolds number. For lower Reynolds number range, the laminar model was applied.

To accommodate the motion of the cylinder, dynamic mesh function was activated. The spring based smoothing and remeshing method was selected for this case. There are five parameters which allow the user to define the settings for the smoothing and can be adjusted based on the actual model, including spring constant factor, convergence tolerance, number of iterations, elements and Laplace node relaxation. For the spring-based smoothing method, the edges between any two mesh nodes are idealized as a network of interconnected springs. The initial spacing of the edges before any boundary motion constitutes the equilibrium state of the mesh. A displacement at a given boundary node will generate a force proportional to the displacement along all the springs connected to the node. Using Hook's Law, the force on a mesh node can be written as

$$\vec{F}_i = \sum_j^{ni} k_{ij}(\Delta\vec{x}_j - \Delta\vec{x}_i) \tag{13}$$

where $\Delta\vec{x}_i$ and $\Delta\vec{x}_j$ are the displacements of node i and its neighbor j, n_i is the number of neighboring nodes connected to node i, and k_{ij} is the spring stiffness between node i and its neighbor j. The spring constant for the edge connecting nodes i and j is defines as

$$k_{ij} = \frac{k_{fac}}{\sqrt{|\overrightarrow{x_i} - \overrightarrow{x_j}|}} \tag{14}$$

where k_{fac} is the value entered for the spring constant factor. At equilibrium, the net force on a node due to all the springs connected to the node must be zero. This condition results in an iterative equation such that

$$\Delta\vec{x}_i^{m+1} = \frac{\sum_j^{ni} kij\overrightarrow{\Delta x_j^m}}{\sum_j^{ni} k_{ij}} \tag{15}$$

where m is the iteration number. Since displacements are known at the boundaries (after boundary node positions have been updated), Eq.15 is solved using a Jacobi sweep on all interior

nodes. At convergence, the position are update such that

$$\vec{x}_i^{n+1} = \vec{x}_i^n + \Delta\vec{x}_i^{converged} \tag{16}$$

where n + 1 and n are used to denote the positions at the next time step and the current time step, respectively.

The user can control the spring stiffness by adjusting the value of the spring constant factor between 0 and 1. A value of 0 indicates that there is no damping on the springs, and boundary node displacements have more influence in the motion of the interior nodes. A value of 1 imposes the default level of damping on the interior node displacements as determined by the Eq.15. In order to maximize the response of the cylinder, the spring constant factor was selected to be 0. The solution of Eq.15 can be controlled by using the values of convergence tolerance and number of iterations. ANSYS Fluent solves Eq.15 iteratively during each time step until one of the following criteria is met:

- The specified number of iterations has been performed.
- The solution is converged for that tine step:

$$\left(\frac{\Delta\vec{x}_{rms}^m}{\Delta\vec{x}_{rms}^1}\right) < \text{convergence tolerance} \tag{17}$$

where $\Delta\vec{x}_{rms}^1$ is the interior and deforming nodes RMS displacement at the first iteration. The values were kept as default for this case. Due to the fact that the mesh structure is a mixed element zone, and spring-based smoothing is not desired to all the elements, thus in the element selection box, the **Tet in Mixed Zones** in 3-D is selected so that only the tetrahedral cells is under spring-based smoothing.

ANSYS^{TM} Fluent V.16 includes several remeshing methods that include local cell remeshing, face region remeshing, local face remeshing, 2.5D surface remeshing (for 3-D flows only) and cut-cell zone remeshing. 2.5D surface remeshing was only compatible with extruded elements. However, the dominant elements in the domain are tetrahedral elements. For this simulation, local cell, local face and region face remeshing methods are applied, which give the user more options to control the mesh regeneration. Parameters including minimum and maximum length scale, maximum cell skewness, maximum face skewness and size remeshing interval are selected based on the software recommended default values. Furthermore, predefined size function has also been adopted in this simulation. In the size function, the function variation, function rate of change, and function resolution have been modified to accommodate the deformation of the meshes for all simulation cases. In the sizing function remeshing option toolbox, three parameters can be controlled to govern the size function. The size function **Resolution** controls the density of the background mesh. By default, it is equivalent to 3 in 2-D simulations and 1 in 3-D simulations. The size function **Variation** is a measure of the maximum permissible cell size and it ranges from $-1 < \boldsymbol{\alpha} < +\infty$. The size function **Rate** is the measure of the rate of growth of the cell size, and it ranges from $-0.99 < \boldsymbol{\beta} < 0.99$. A value of 0 implies linear growth, whereas higher value implies a slower growth near the boundary with faster growth as one move toward interior. The new mesh configuration is automatically constructed based on the displacement of the cylinder and parameters in dynamic meshes settings. Then FLUENT solves the Navier-Stokes and turbulence equations again on the new mesh configuration. This fluid-structure interaction loop is repeated at each time step of the simulation until convergence criteria is met.

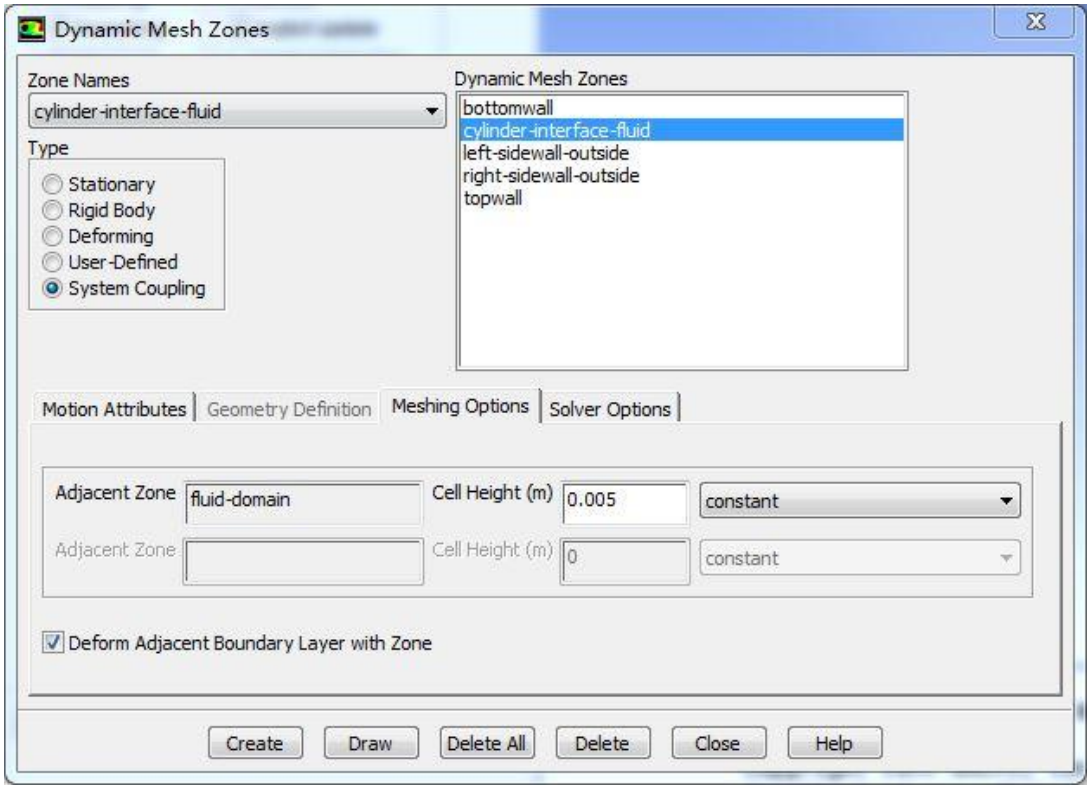

Figure 18 Dynamic Mesh Zones-Cylinder Interface

Figure 18 is the Dynamic Mesh Zones Setting window, as it can be seen, there are five different zones, and each is assigned to a specific type. Cylinder interface is a system coupling zone, which allows the zone to be involved in a system coupling simulation where the motion is defined by the application that ANSYS Fluent is coupled with on this zone, which is Transient Structural workbench for this simulation. Under geometry definition, deform adjacent boundary layer with zone option can be selected, which enables the smoothing of an adjacent boundary layer mesh. This option is not available when stationary and deforming is selected in the type list. By selecting this option, the quadrilateral inflation layers, which closest to the cylinder interface for this simulation, can move simultaneously with the cylinder. Thus, finer and uniform quadrilateral meshes are always available near the cylinder boundary with excess computational effort.

The top and bottom walls are subjected to stationary zone, so that the nodes on these two zones are excluded when updating the node positions. The left and right wall that parallel to the flow direction are set to be deforming zones. For deforming zones, three parameters including minimum length scale, maximum length scale and maximum skewness can be adjusted based on the actual zone scale information. The minimum and maximum length scale allows the user to specify the minimum and maximum length scale for the zone, and they are 0.004m and 0.03m for the current simulation. The maximum skewness is used to specify the desired value for maximum skewness, which is set to be 0.5.

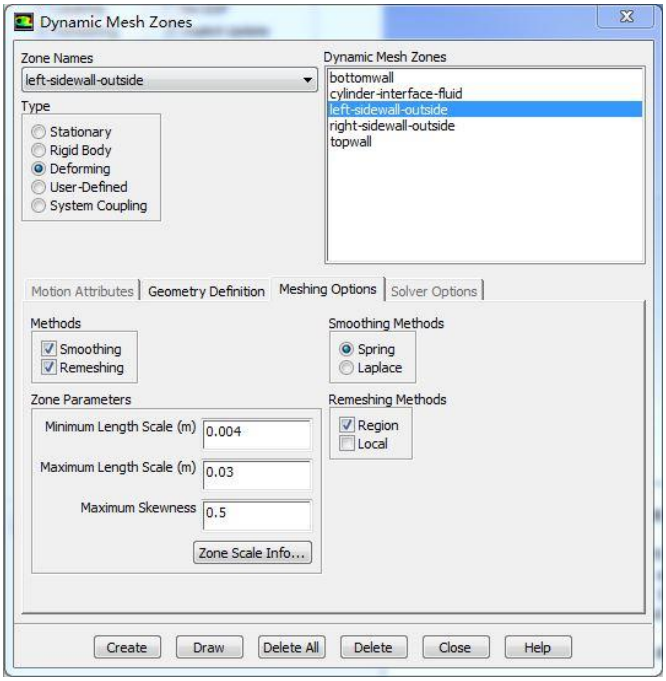

Figure 19 Dynamic Mesh Zone-Deforming Zones

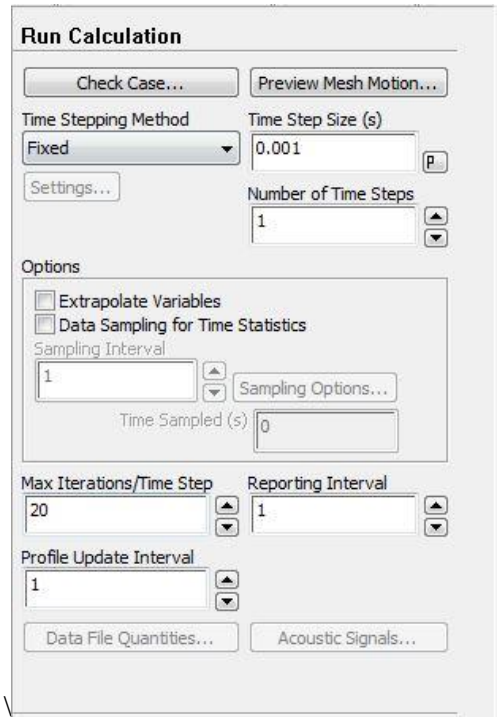

Figure 20 Run Calculation Control

Figure 20 is the settings of run calculation control of ANSYS Fluent, the time step is selected to be 0.001s, and this step size is being tested on many mesh sizes. Since the finer the mesh, the smaller the step size need to be chosen. With the current hardware standards and solution accuracy requirements, after many tests, the step size of 0.001s is the best choice for the two-way coupled simulation. However, for the case of higher inlet velocity (U= 8 m/s), the step size was adjusted to be 0.0005s. The number of time step here is set to be 1 since for coupling simulations, the time duration is actually being controlled by the system coupling setup workbench. During the co-simulation, the drag and lift coefficients are written and exported in the directory folder. At the meantime, the solution history of quantities including total pressure, velocities and vorticity are exported for further data post processing.

4.2 Structural Setup

The settings for the transient solid model are presented in this section. The mesh structure for the solid part is tetrahedral elements so that the solution from ANSYS Fluent can be properly interpolated onto the fluid-solid interface. The cylindrical surface of the cylinder is set to be the system coupling interface, the elastic support and displacement constraints are applied on the surface as well. The elastic support uses Elastic Foundation Stiffness (EFS) as a parameter, which specifies spring stiffness per unit volume that only acts in the direction normal to the face of the elements. EFS has an unit of N/m^3, thus for difference geometry, proper conversion of spring stiffness needs to be considered. The displacement constraints have set the displacement along Z-axis to be zero, and free on x and y axis, which indicates that the cylinder has freedom along in-line and transverse direction. The directional deformation along X and Y direction was calculated during the simulation. The displacements of the solid part along in-line flow and transverse direction were analysed and compared with 1-way numerical results and experimental data. The details of the solution will be discussed in the details in Chapter 5 of the thesis.

4.3 Experimental Setup

Experimental tests were conducted in the laboratory to study the behaviors and performance of the harvester in the real working environment. The displacement and frequency of the oscillation of the harvester was recorded using a data-acquisition system. The experimental results was analysed and compared with numerical results for the purpose of validation.

In this section, the details of experiments conducted on the proposed energy harvester are presented. The experiments were conducted in the laboratory flume shown in Figure 21 (a). During the experiments, the free stream flow velocity was maintained in the range of 0.2 m/s to 0.5 m/s by changing the operating frequency of the pump. The discharge rate in unit of (L/s) increases linearly with the increase of operating frequency (*Hz*). With higher discharge rate, larger amount of water is pumped into the flume, which results in the increase in depth of fluid in flume, a gate installed at the exit the flume was used to adjust the depth accordingly.

Figure 21 (b) is a CAD drawing of the mounting frame, which was used in the experiments to secure the cylinders to be immersed into the fluid flow. The side beams and cylinders used in the experiments are made of acrylic for better visualization, the rod connected the cylinder with the frame is made of rust-resistance stainless steel. There are several holes on the beams for the purpose of adjusting the location of the cylinder in the fluid flow. The specifications of all the material used in the experiment were provided in the Table C. 1 in Appendix C.

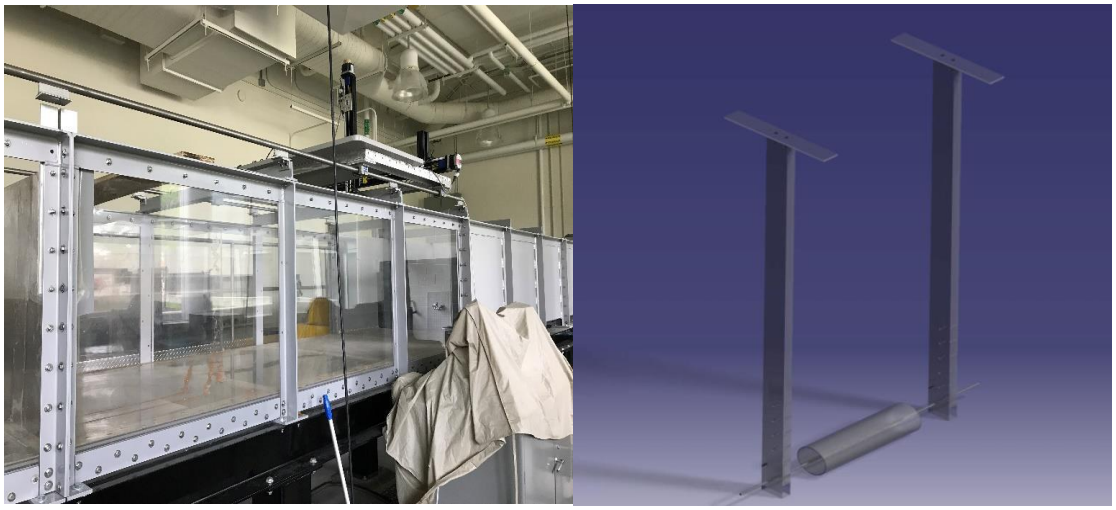

(a) **(b)**

Figure 21 (a) Laboratory Flume (b) Mounting Frame

Table 3 Table of Flow Conditions

D=0.089m	Frequency (*Hz*)	Discharge rate, Q (L/s)	Depth (m)	Bulk velocity (m/s)
#1	55	129.4	0.211	0.51
#2	46	107.3	0.199	0.45
#3	40	92.7	0.198	0.39
#4	36	82.9	0.197	0.35
#5	31	70.6	0.196	0.3
#6	25	56	0.187	0.25
D=0.11m				
#1	49	114.7	0.233	0.41
#2	41	95.1	0.226	0.35
#3	35	80.4	0.223	0.3
#4	23	51.1	0.213	0.2

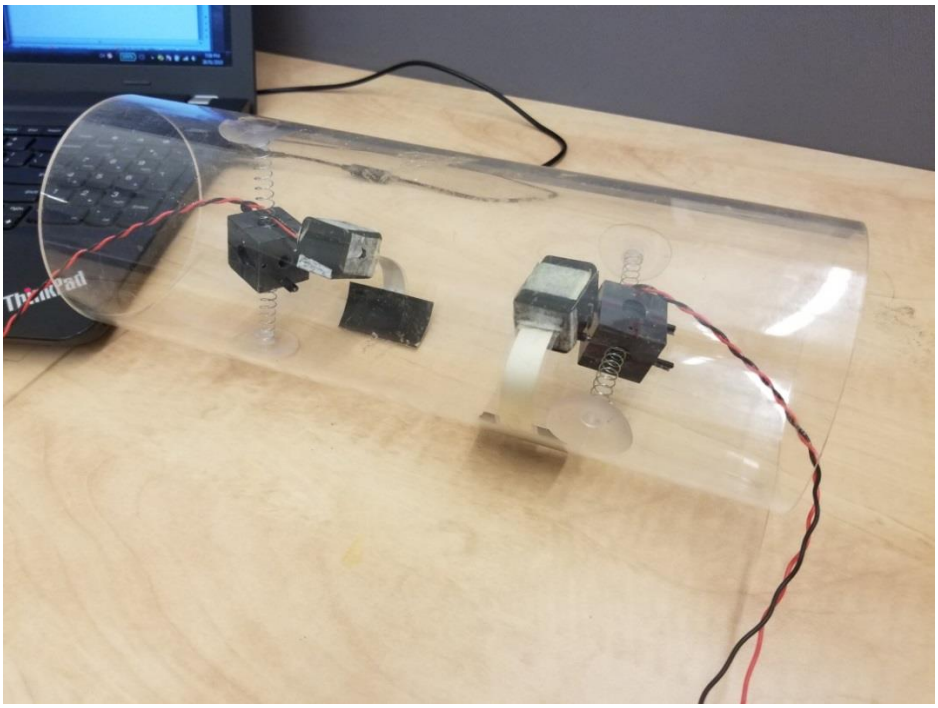

Figure 22 Harvester Assembly

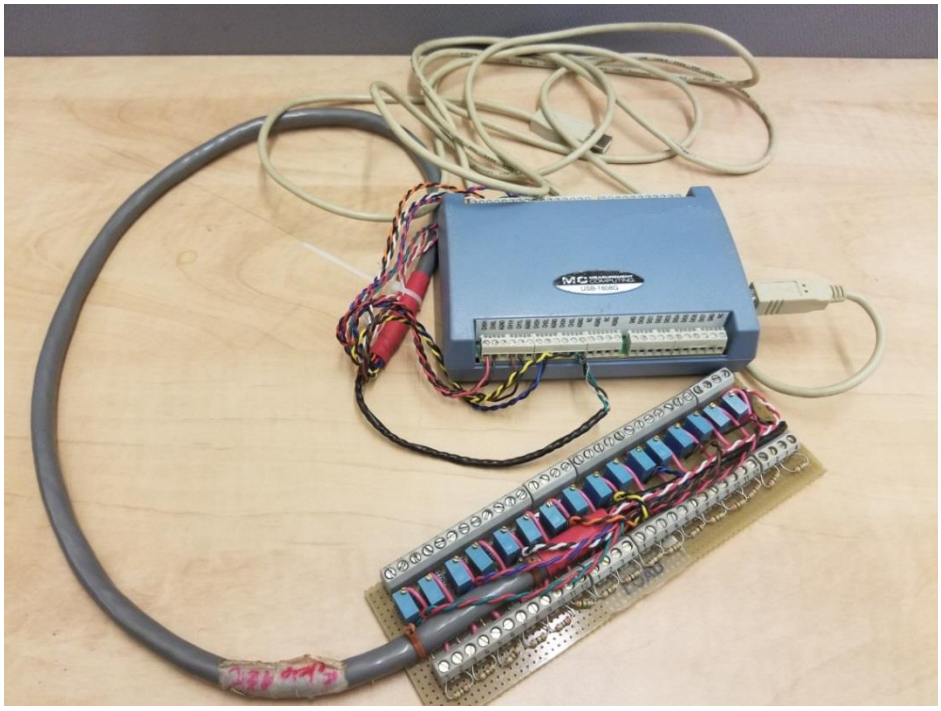

Figure 23 Data Acquisition System

The data acquisition system being used in the experiments is purchased from Measurement Computing (MC), and some modifications were done to add more channels to the device, as shown in Figure 23. The model number is USB-1608G, which is a high-speed multifunction USB data acquisition (DAQ) device, is ideal for low to medium channel count applications, and provides analog, digital, and counter/timer functions. DAQami software was used to record the output voltage of the piezoelectric transducer. Figure 24 is the interface of the software. The differential mode was selected and active channels are Analog input #1(AI1) and AI7 which corresponds to the piezoelectric transducers mounted in the lateral and longitudinal position, respectively. The deformation of the piezoelectric transducer was transformed into analog signal in the unit of mV, and the range is $\pm$1V. The sampling rate is 100 analog samples per second. Uncertainty analysis indicates that analog input DC voltage measurement accuracy, for the range of $\pm$1V, has the gain error is $\pm$0.024% of reading and offset error of $\pm$245 μV.

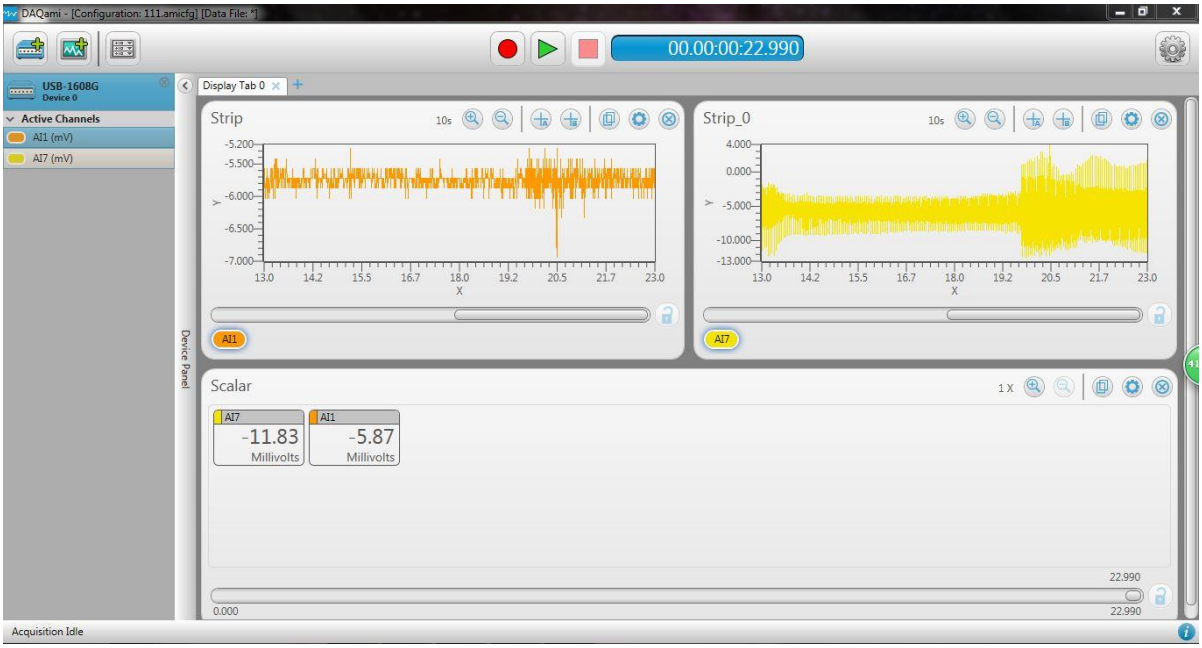

Figure 24 DAQami Software Interface

During the experiments, the deformation of the piezoelectric material mounted on the cylinder, which placed perpendicular to each other, are converted into analog signal and recorded by the data acquisition system. The piezoelectric transducer placed parallel to the flow is corresponding to the inline flow VIV frequency response, while the other one corresponds to the cross-flow VIV response. Detailed analysis of the experimental data and comparison between the experimental and numerical results will be discussed in the next chapter.

CHAPTER 5

RESULTS AND DISCUSSION

5.1 Computational Results

5.1.1 2-D Numerical Results

Flow past cylinders with different diameters ranging from 0.05m to 0.2m has been simulated with ANSYS™ Fluent. During the simulations, variations of the drag and lift coefficients have been monitored. Figure 25 to Figure 28 present the time history of drag and lift coefficients of the simulations with inlet velocity of 1 m/s for cylinders with various diameters. After the transient period at t = 2.5s, the drag and lift coefficient oscillate periodically in time with well-defined frequency and amplitude. Fast Fourier Transformation (FFT) was done for each different case to investigate the response frequency; it was found that the vortex shedding frequencies are dropping as the diameter of the cylinder gets larger. Another key finding is the drag coefficient, oscillates with a frequency that is twice that of the lift coefficient and of the vortex shedding itself. Drag is due to the difference between the pressure on the front and the back of the cylinder. The pressure on the front is the stagnation pressure of the incoming flow ($P_\infty + \frac{1}{2}\rho U^2$). The pressure at the rear of the cylinder, the base pressure, drops with the shedding of vortices, irrespective of its sign. Thus, it oscillates at twice the shedding frequency [75].

Take the simulation for cylinder with diameter of D = 0.09m as an example, the drag and lift coefficients C_d and C_l as a function of time were recorded and exported. The data were further imported to MATLAB™ and the values of the drag and lift forces as a function of time were calculated using the following correlations:

$$F_d(t) = C_d A_p \left(\frac{\rho V^2}{2}\right) \tag{18}$$

$$F_l(t) = C_l A_p \left(\frac{\rho V^2}{2}\right) \tag{19}$$

where C_d is drag coefficient, C_l is lift coefficient and A_p is projected area of the body into the fluid stream. The selected time interval was selected from 5s to 10s which corresponds to the steady oscillating behaviour. Next, general-least-square regression was applied to find the best analytical function that fits the lift and drag forces as a function of time. It was found that the expressions of drag and lift force combine sine and cosine functions with the following form:

$$F_d(t) = 8 + 1.2\sin\left(41t - \frac{5\pi}{8}\right) - 0.4\cos\left(41t - \frac{5\pi}{8}\right) \tag{20}$$

$$F_l(t) = 0.12 - 5.3\sin\left(20.5t - \frac{3\pi}{8}\right) + 8.3\cos\left(20.5t - \frac{3\pi}{8}\right) \tag{21}$$

As it can be seen from Eq.21, the frequency ($\omega = 2\pi f$) of the oscillation of the lift force exerted on the cylinder is 3.27 *Hz*, which is very close to the theoretical vortex shedding frequency (f_s).

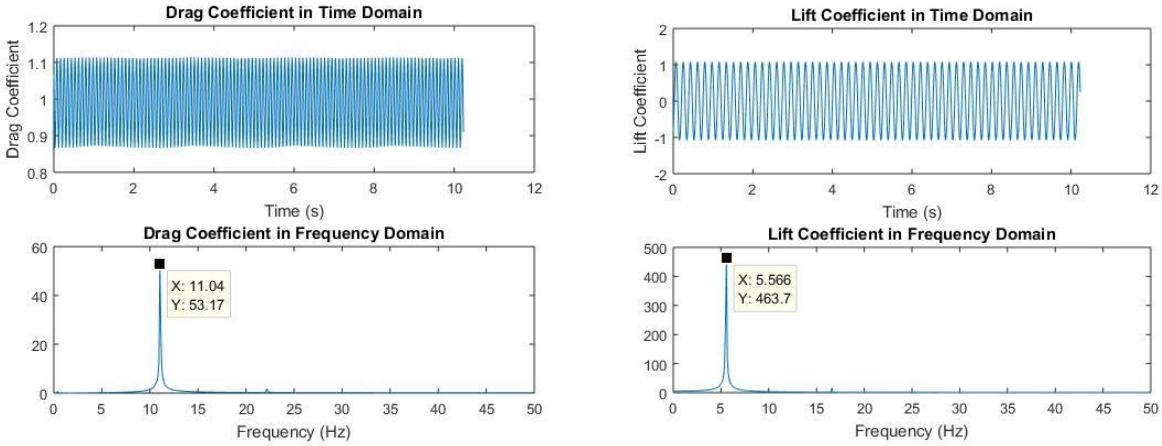

Figure 25 Drag and Lift Coefficient for Cylinder of D=0.05m

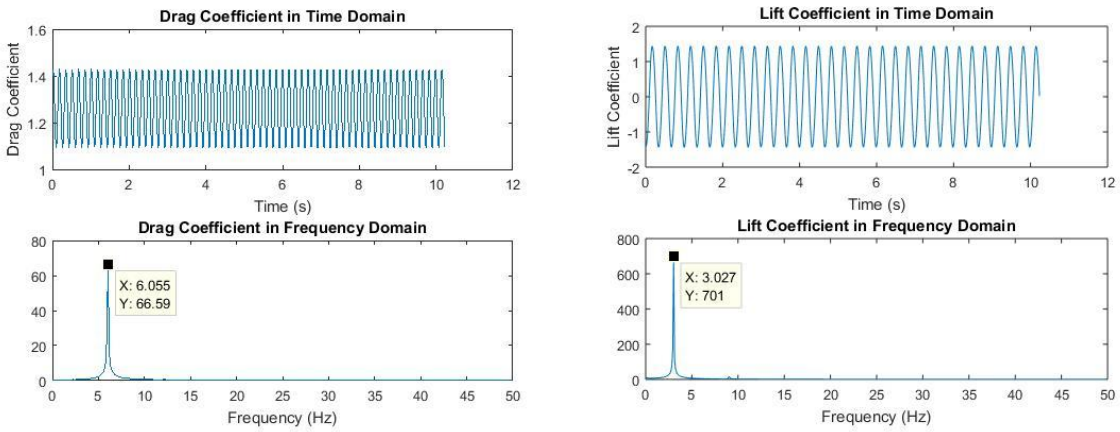

Figure 26 Drag and Lift Coefficient for Cylinder of D=0.09m

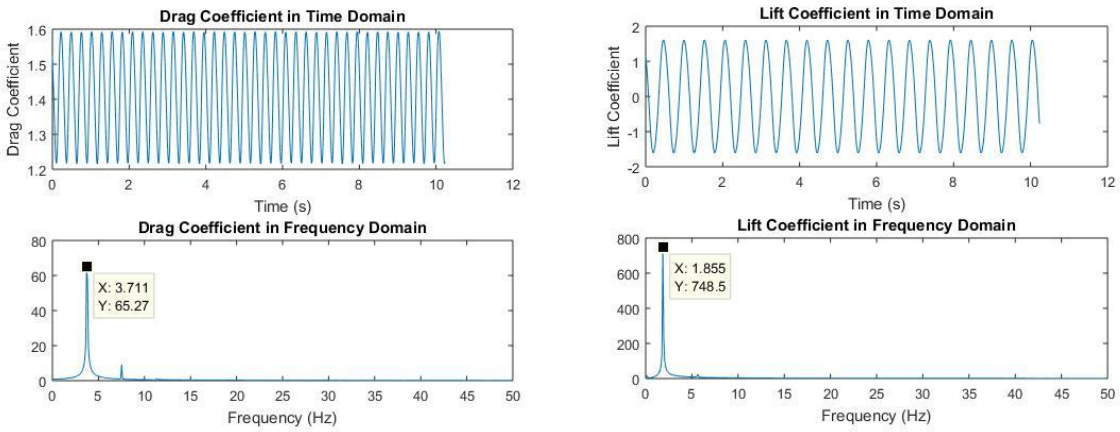

Figure 27 Drag and Lift Coefficient for Cylinder of D=0.15m

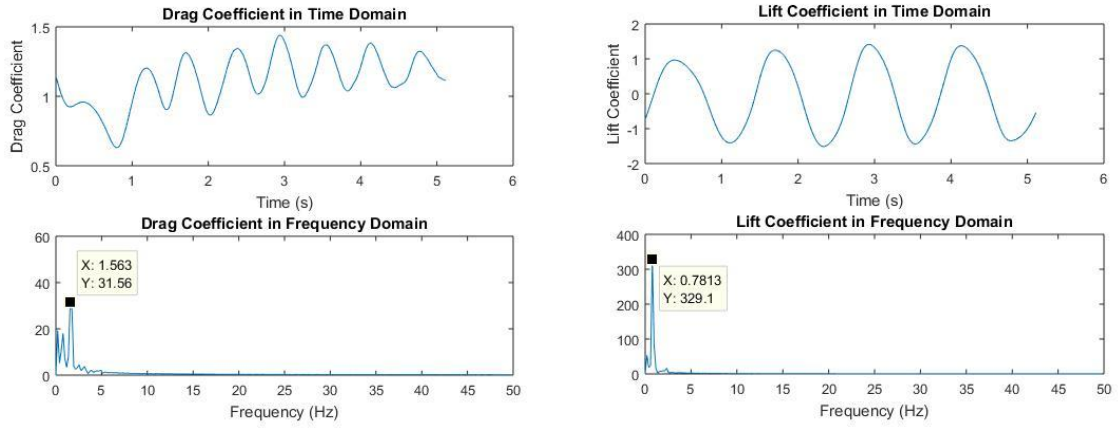

Figure 28 Drag and Lift Coefficients for Cylinder of D=0.2m

By applying the interpolated drag and lift forces into the equations of motion of the cylinder (Eqs.6 and 7), the amplitude and frequency of oscillation of the cylinder can be obtained numerically. In Figure 29 and 30, the cross-flow and inline flow displacements as a function of time for the cylinder with diameter of D=0.09m were numerical calculated and reported. For cylinders with different diameters, the displacements are also reported in the thesis, which can be found in Appendix B. From the plots, the frequency and amplitude response of cylinder with different dimension can be obtained. Dominant VIV response frequencies and oscillation amplitude of cylinders with different dimension are summarized in Table C. 2 in the Appendix C. Energy density for cylinder with different diameter was calculated and reported in Figure 31. The energy density is proportional to the square product of amplitude and frequency$(A * f)^2$. This quantity is used to compare the performance of each cylinder with different diameter. Figure 31 shows that the optimum cylinder diameter providing maximum energy density was found to be 0.09m.

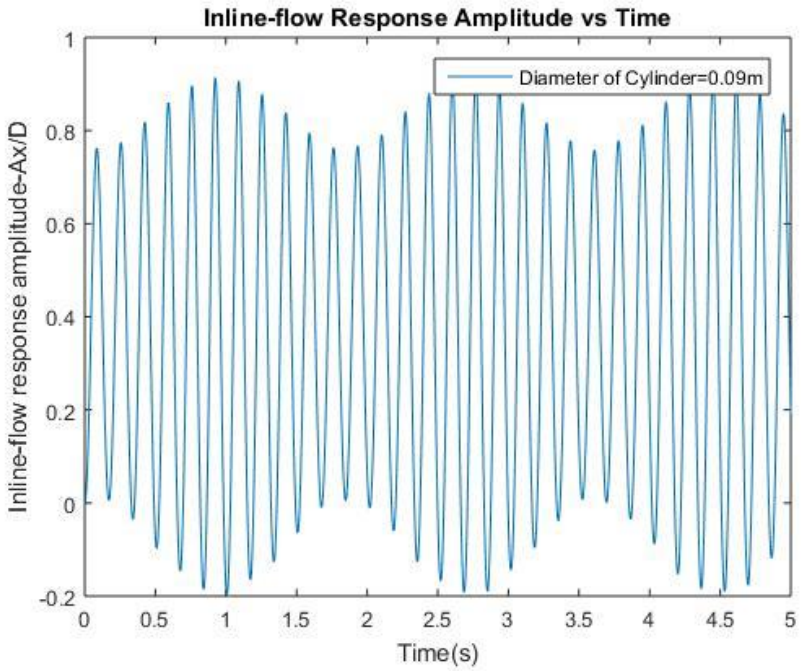

Figure 29 Inline-flow Response Amplitude (Ax/D) vs Time (D=0.09m)

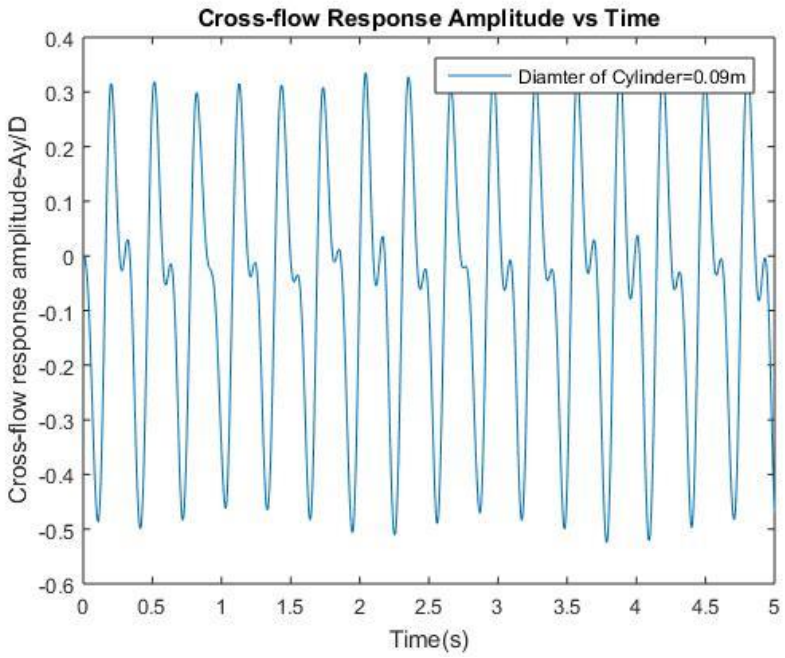

Figure 30 Cross-flow Response Amplitude (Ay/D) vs Time (D=0.09m)

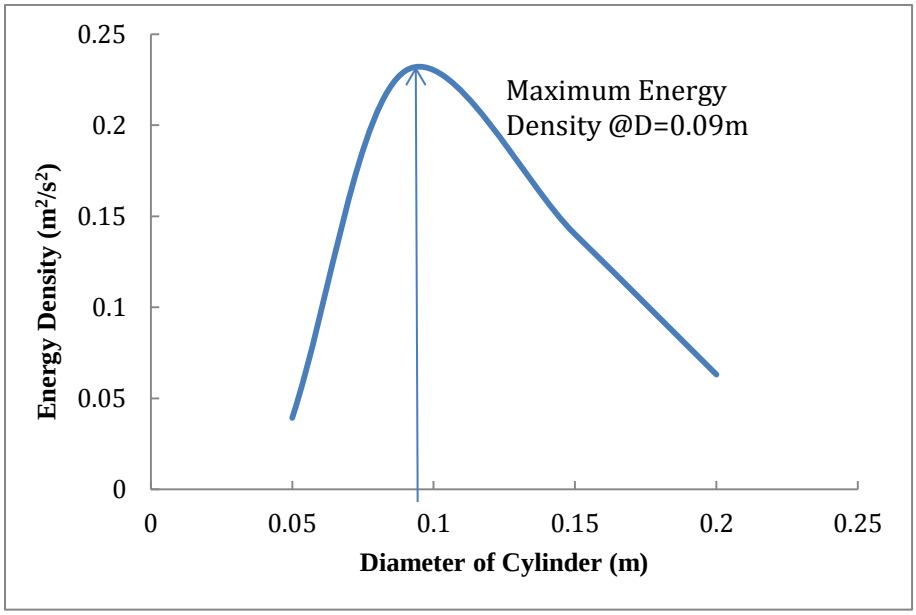

Figure 31 Energy density vs Diameter of cylinder

5.1.2 3-D Numerical Results-Stationary Cylinder

The results of 3-D numerical simulation of stationary cylinder are reported in Table 4. There are six cases with different inlet velocities ranges from 0.5 m/s to 16 m/s, which corresponds to Reynolds number from 4.44×10^4 to 1.42×10^6. FFT analysis was done for each case, the VIV response frequencies were found to increase dramatically with increasing velocity. The averaged drag coefficients against Reynolds number were reported in Figure 32, which was in agreement with the published experimental and numerical results [74]. The drag coefficient is nearly constant for the sub-critical Re regime $C_d \approx 1.2$, then drops dramatically by factor of 4 to $C_d \approx 0.28$ for the critical Re regime and keep constant for at this value for the super-critical Re regime as well, and increases to $C_d \approx 0.4$ for post-critical Re regime. The fluctuation of the drag coefficient is well predicted by the present DES model. On the other hand, the mean lift coefficient drops with the increase of Reynolds number, the reason is that the asymmetric laminar separation bubble near the boundary of sub-critical regime results in large lift coefficient ($C_l \approx 1$), with the increase of Reynolds number, the laminar boundary layer gradually resolved into chaotic turbulent layers. Strouhal number St of different cases was also concluded in Table 4. The maximum St was found near critical Re regime with $S_t = 0.32$ and drops with Re moves in super-critical regime. In comparison with the experimental results, the Strouhal number obtained from results of present DES model is being under-predicted for super-critical Re regime. Since the calculation of St is correlated to the time history of the lift coefficient, thus the under-estimation of St for the super-critical Re regime is most likely due to the grid coarseness.

Table 4 3-D-Stationary Cylinder Simulation Summary

Re	$\overline{C_d}$	$\overline{C_l}$	f_{C_d}	f_{C_l}	U (m/s)	St
4.44E+04	1.17	0.92	3.13	1.56	0.5	0.26
8.88E+04	1.01	0.86	6.35	3.13	1	0.27
2.00E+05	0.88	0.51	13.87	6.87	2.25	0.28
3.55E+05	0.34	0.23	28.61	14.26	4	0.32
7.11E+05	0.27	0.17	43.55	21.97	8	0.24
1.42E+06	0.39	0.13	70.70	35.25	16	0.20

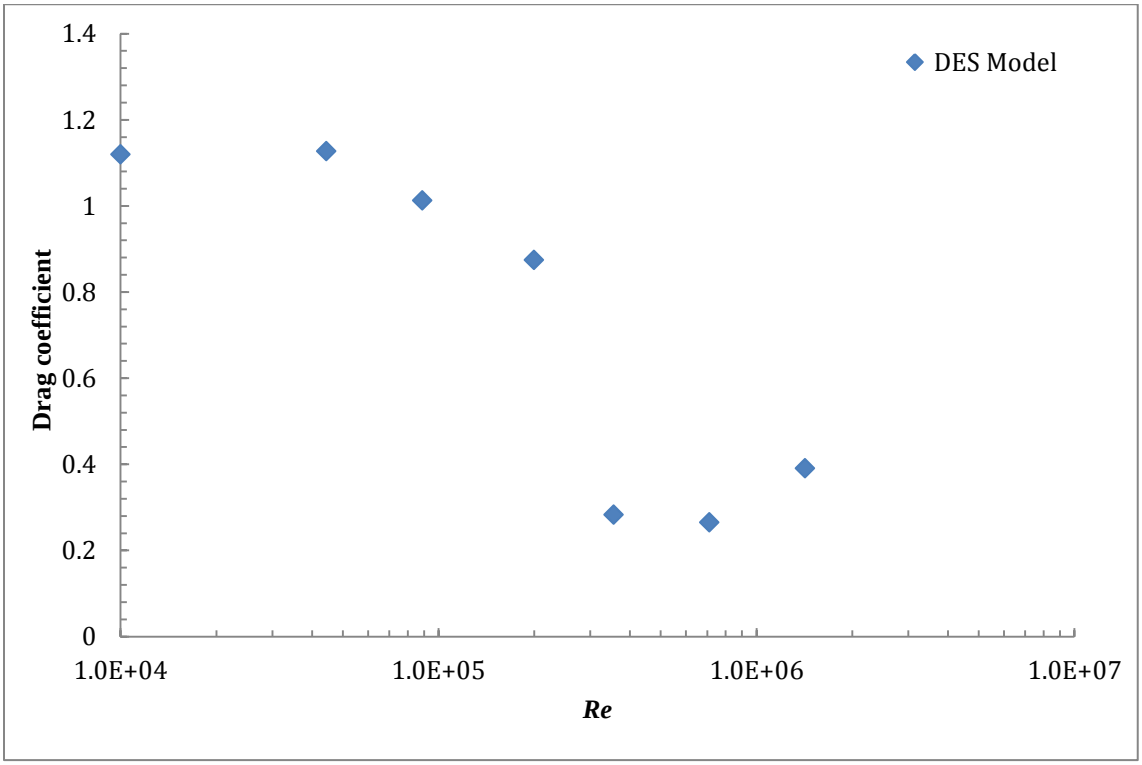

Figure 32 Drag coefficient vs Re of Current DES Model

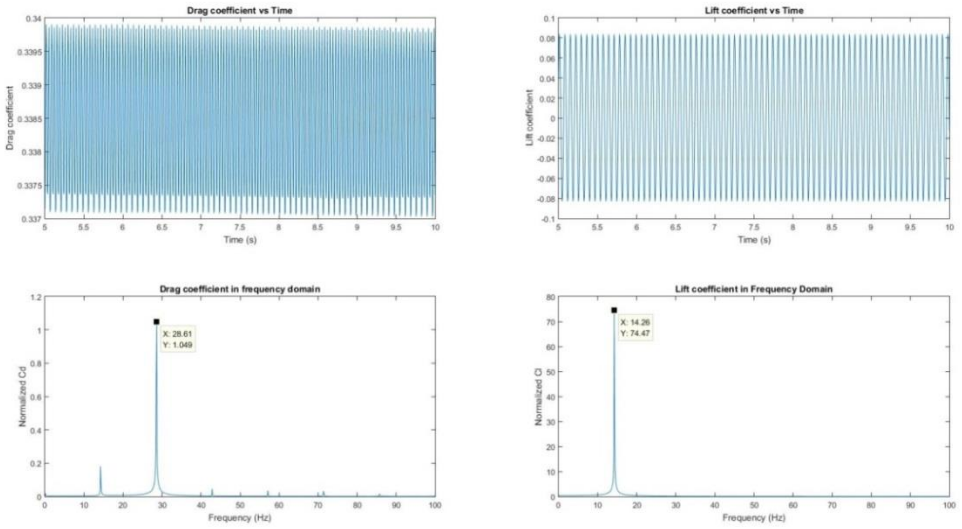

Figure 33 FFT Analysis of Simulation of U=4 m/s

Spectral analysis of drag and lift coefficients for the 3-D simulation was carried out using FFT analysis. Figure 33 is an example of FFT analysis for the simulation with inlet velocity of 4 m/s. The dominant frequency of the oscillation of drag was found to be 28.61 *Hz* and 14.26 *Hz* for lift coefficient, respectively. The FFT analysis for other cases can be found in the Appendix B. Figure 34 (a)-(b) show the streamlines and vorticity contours for 3-D simulations with different inlet velocities.

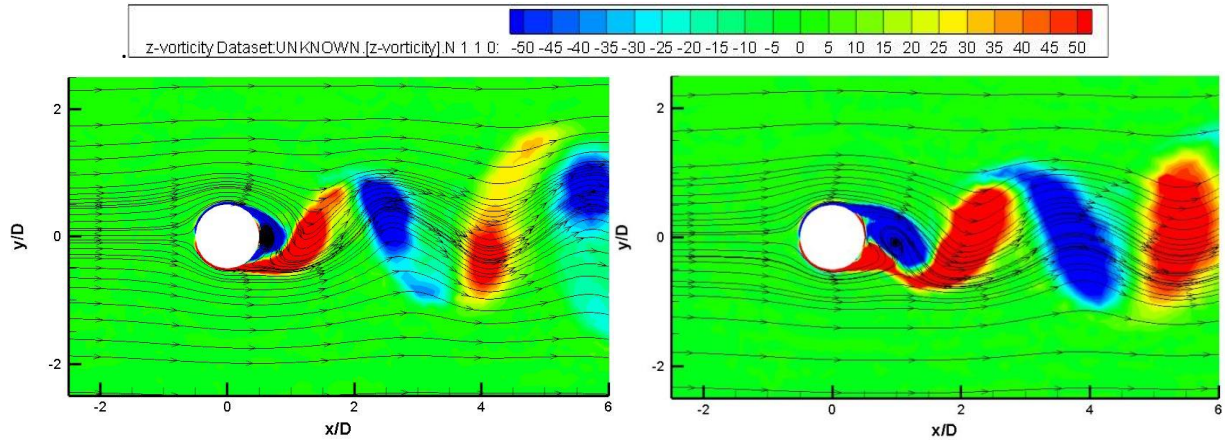

(a) (b)

Figure 34 Vorticity Contours with Streamlines for (a) U=2.25 m/s (b) U=4 m/s

5.1.3 3-D Numerical Results-2 DOF Cylinder

The results of coupled FSI simulations of cylinder with 2-degree of freedom (DOF) were reported in Table 5. It is observed that there is a significant increase in the vibration amplitude (A_y/D , A_x/D) when the inlet velocity shifts to higher values. Large increase of response amplitude in the transverse direction results in the increase of the power output. The in-line and cross-flow VIV response frequencies also rise with increasing velocities. The root-mean-square value of drag coefficient is related to the turbulence in the model, high turbulence was achieve by increasing the inlet velocity up to 8 m/s. In Figure 35, the power output versus root-mean-square value of the drag coefficient, C_d^{rms} are plotted. Higher C_d^{rms} value indicates the instability of the flow because of the high turbulence created. Thus, it can be concluded that the high turbulence is beneficial for the purpose of energy harvesting.

Table 5 Summary of two-way FSI Simulations

U (m/s)	C_d^{rms}	$f_{crossflow}$ (*Hz*)	f_{inline} (*Hz*)	A_y/D	A_x/D	St	P_Potential (mW)
0.5	0.74	1.95	4.40	0.063	0.033	0.30	5.22
1	1.68	2.69	5.62	0.199	0.155	0.24	11.90
2.25	2.21	4.15	8.30	0.476	0.413	0.16	20.98
4	2.84	6.84	12.70	1.036	0.734	0.15	24.20
8	4.21	8.54	17.24	2.156	1.058	0.10	41.14

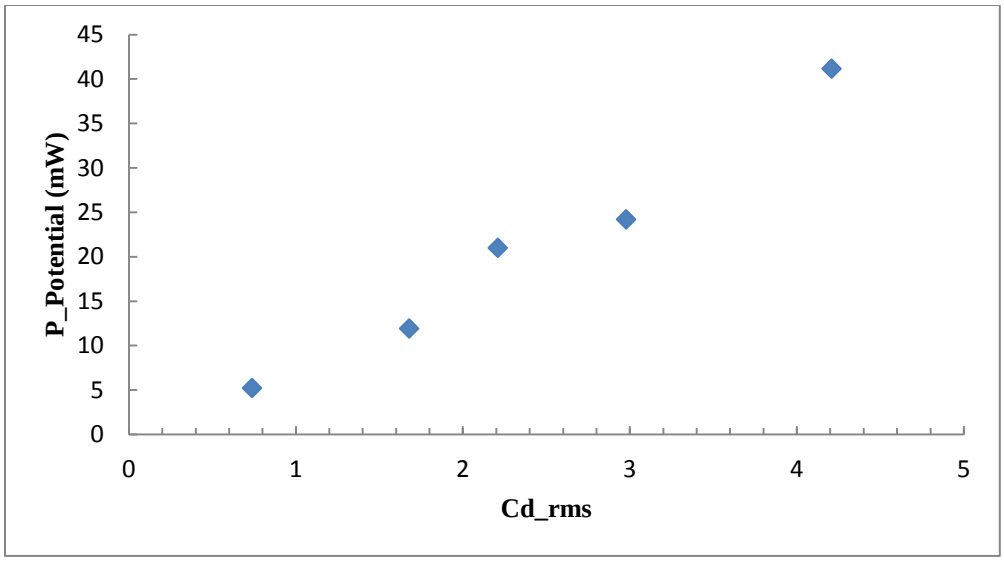

Figure 35 Harvested Power Output vs C_d^{rms}

The lateral and longitudinal displacements of the harvester were exported from the transient structural workbench to MATLAB to estimate the power output of the proposed harvester, which is reported as P_Potential in Table 5. The overall efficiency of the harvester is estimated analytically by integrating lateral and longitudinal displacements of the cylinder to find the X (in-line) and Y (transverse) velocity of the cylinder versus time and then calculate the kinetic energy the harvester captured from the flow.

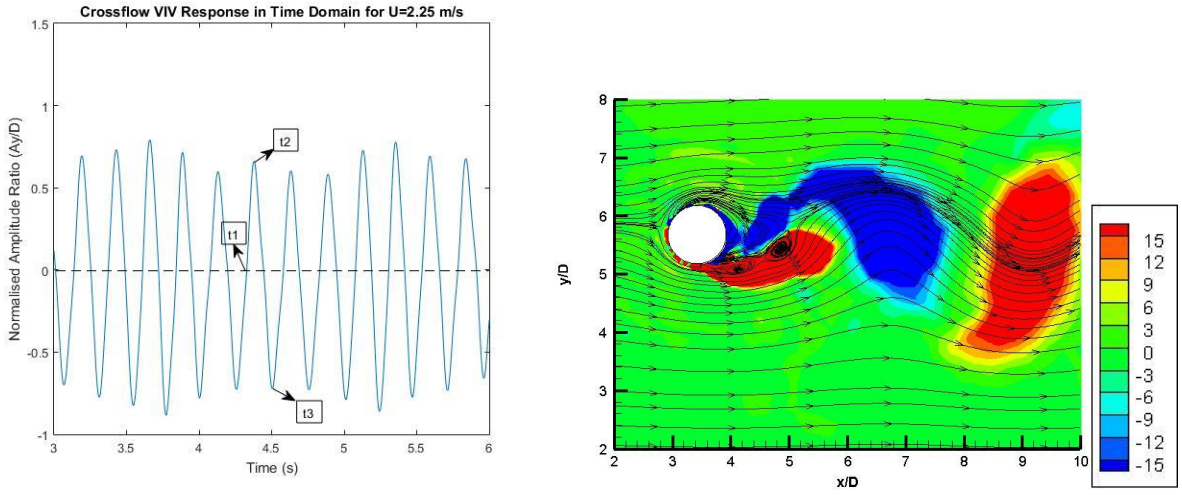

(a) (b)

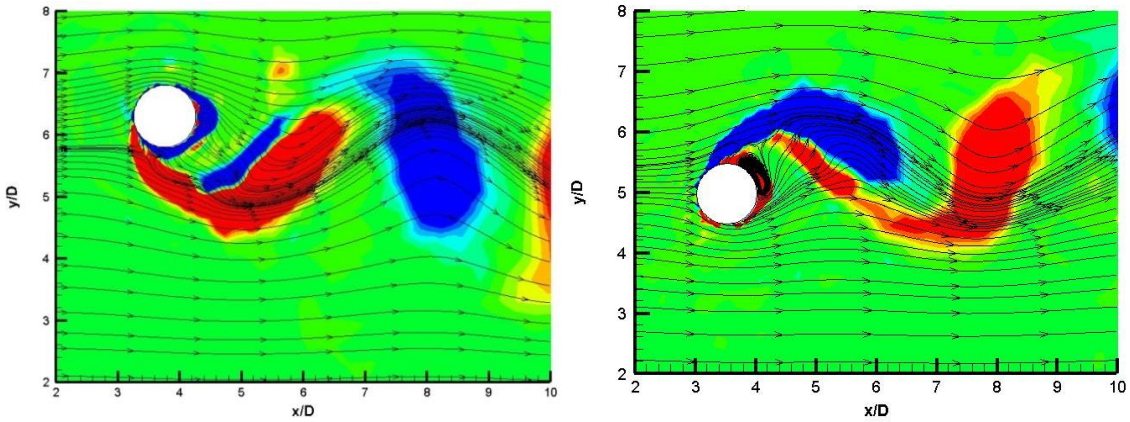

(c) (d)

Figure 36 Instantaneous Vorticity Contours with Streamlines at Time

(b) t1 = 4.329 s (c) t2 = 4.378 s and (d) t3 = 4.506 s

The flow patterns observed in the center plane of the domain are depicted in Figure 36 (a)-(d), which represents iso-contours of the instantaneous span-wise vorticity (ω_z). Vorticity contours are displayed for inlet velocity of U=2.25 m/s for one oscillation period. The location of the cylinder along its trajectory is shown in Figure 36 (a) and the corresponding instantaneous vorticity fields at the identified instances (t_1, t_2 and t_3) of shedding are depicted in Figure 36 (a). In the wake of the cylinder, the vortex shedding corresponds to $2P_0$ shedding regime as classified by Morse and Williamson [75]. In this regime, the alternating vortices are generated in the far wake which was progressively decaying as advected downstream. In the near wake region, a positive vortex is attached to the lower shear layer as shown in Figure 36 (b) and (c). The structural response is in phase with the positive attached vortex. Consequently, negative vortex is attached to the upper shear layer as shown in Figure 36 (d), where the cylinder displacement is also negative. The corresponding velocity vectors identify regions of flow acceleration around the cylinder. The flow is affected by the motion of the cylinder and differs significantly from the flow around a rigid fixed cylinder.

5.2 Experimental Results

Analog signal recorded from the data acquisition system was then imported into MATLAB for FFT analysis to investigate the frequency response of the harvester. During the experiments, videos of each test were taken and the amplitude of the harvester was measured by Pixel Measuring Tool. The tool works as a virtual ruler, which can measure the number of pixels of a certain distance, for this case, the displacement of the harvester. By knowing the size of a pixel, the maximum displacement of the harvester can be obtained and used to calculate the amount of potential energy converted from the kinetic energy of fluid flow.

From Figure 37 to Figure 42 are the results of FFT analysis of harvester with diameter of 0.089m, and Figure 43 to Figure 46 are for larger harvester with diameter of 0.11m. Table 6 is the summary of the experimental results of all the testing cases.

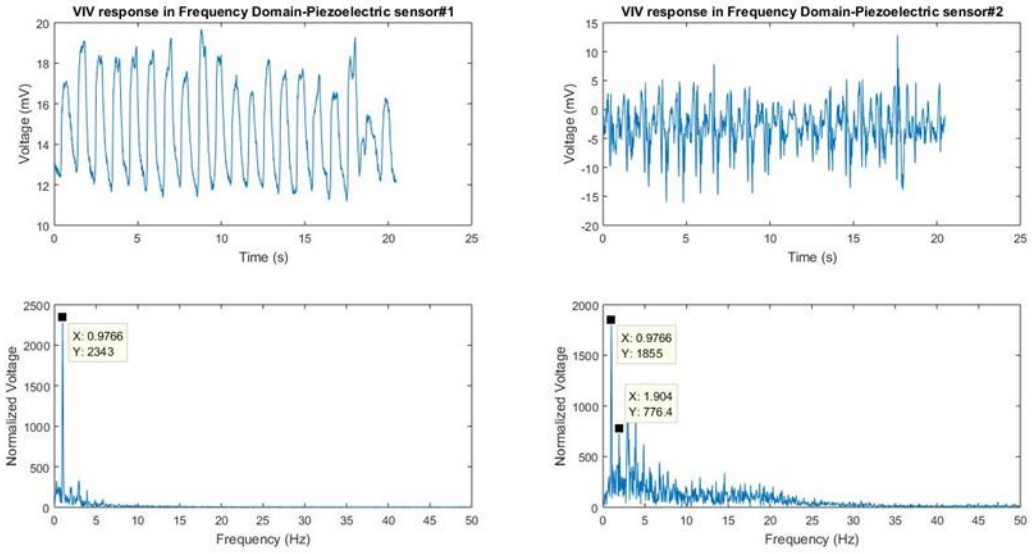

Figure 37 Case #1 of Harvester with D=0.089m

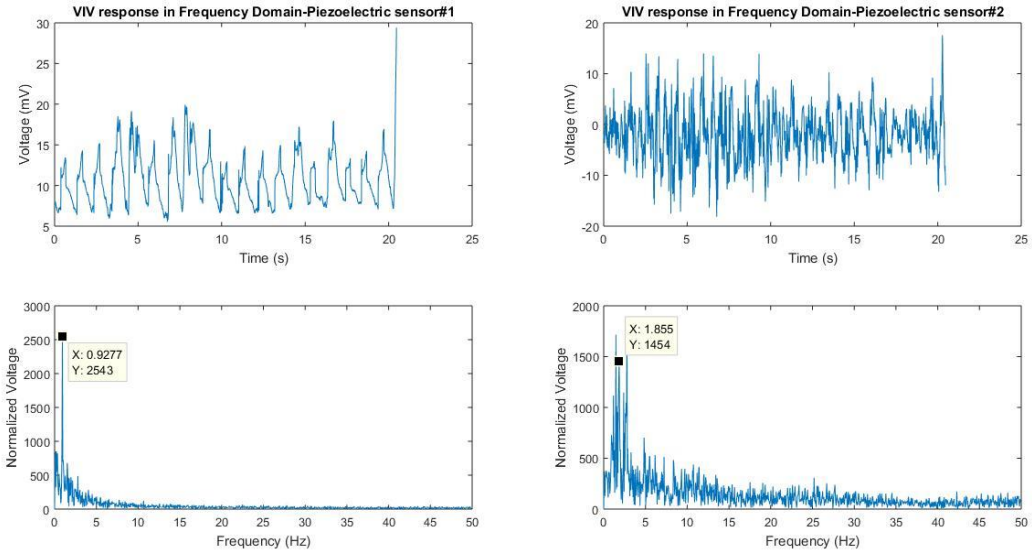

Figure 38 Case #2 of Harvester with D=0.089m

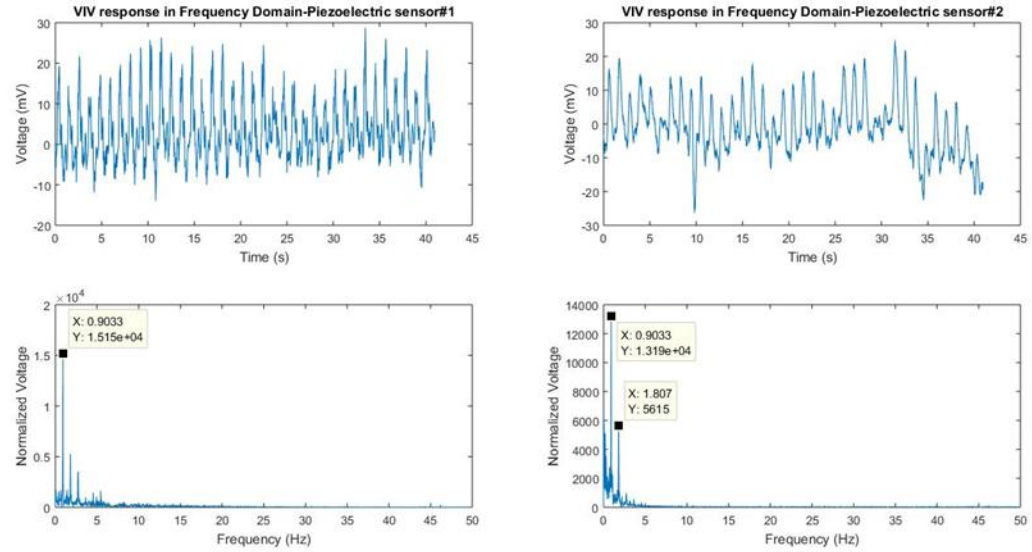

Figure 39 Case #3 of Harvester with D=0.089m

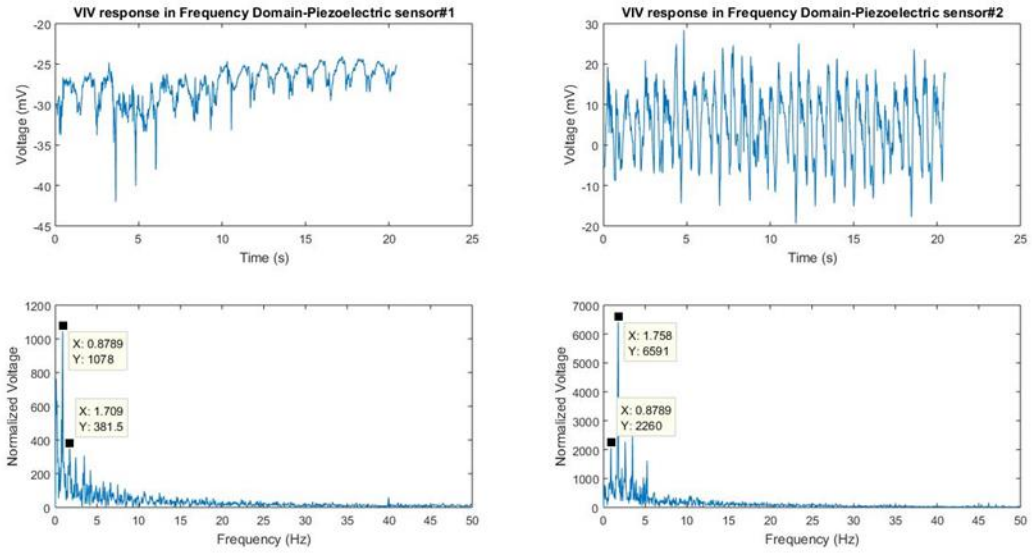

Figure 40 Case #4 of Harvester with D=0.089m

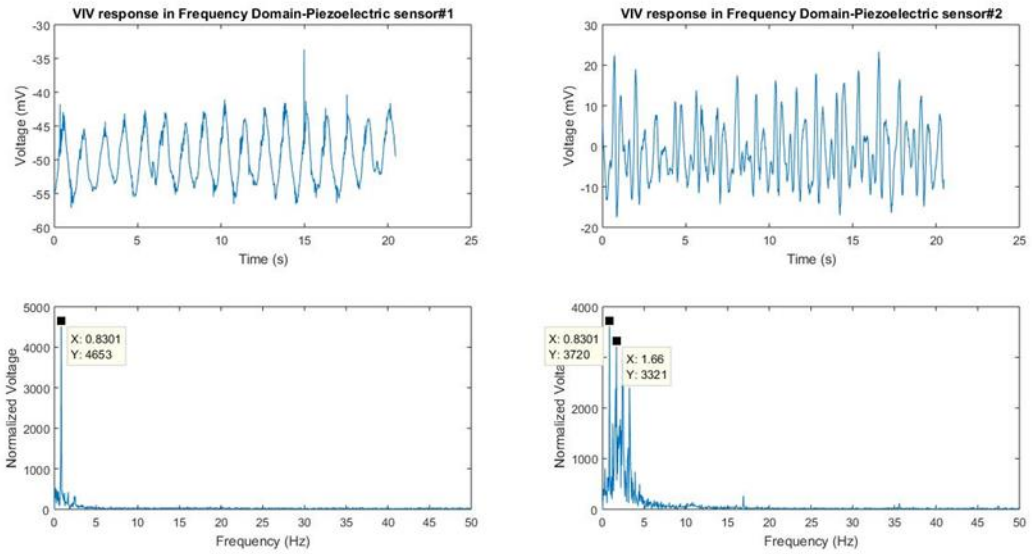

Figure 41 Case #5 of Harvester with D=0.089m

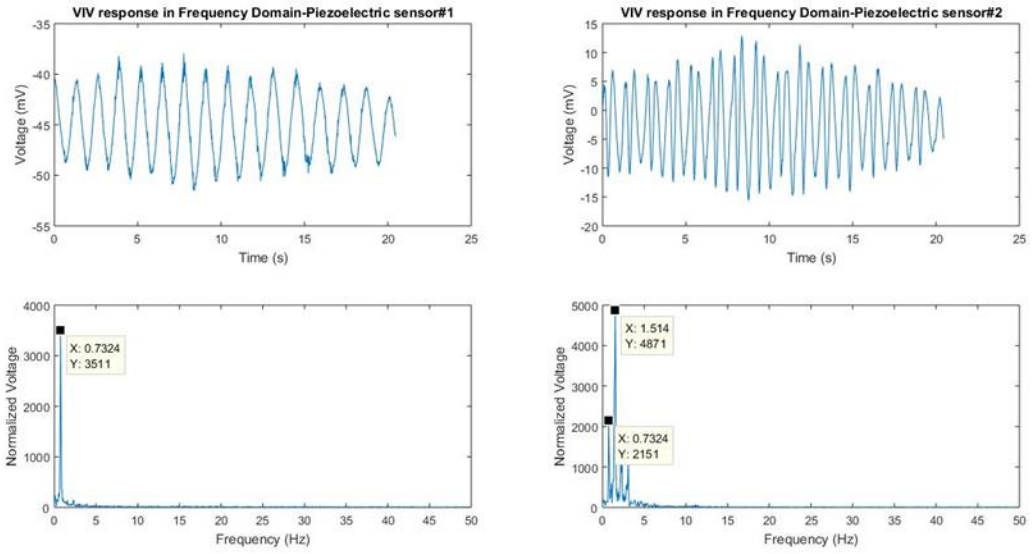

Figure 42 Case #6 of Harvester with D=0.089m

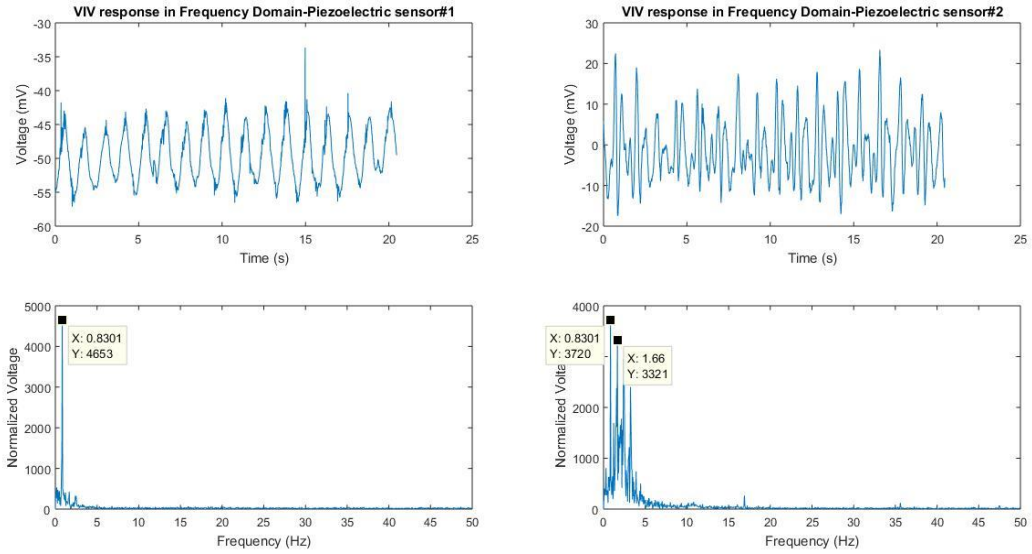

Figure 43 Case #1 of Harvester with D=0.11m

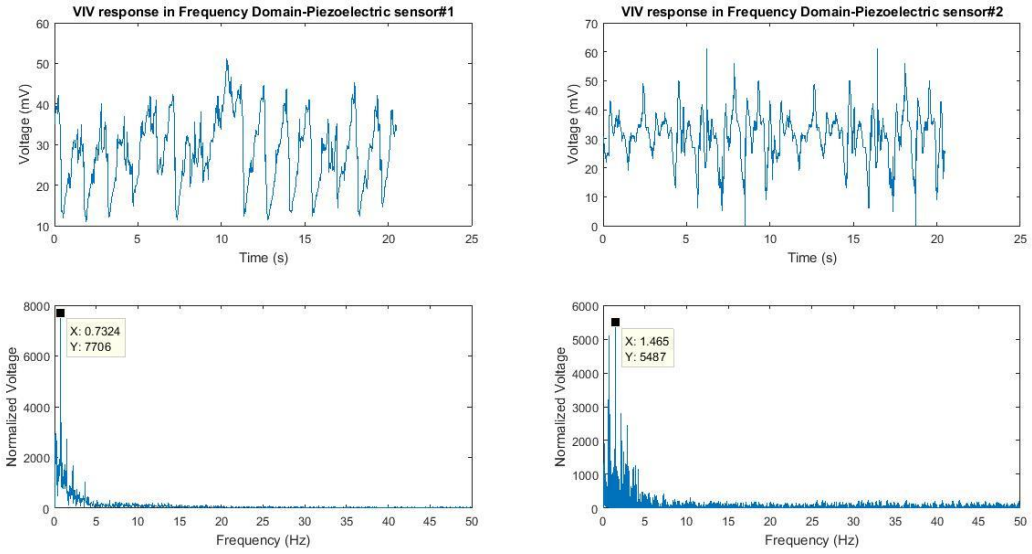

Figure 44 Case #2 of Harvester with D=0.11m

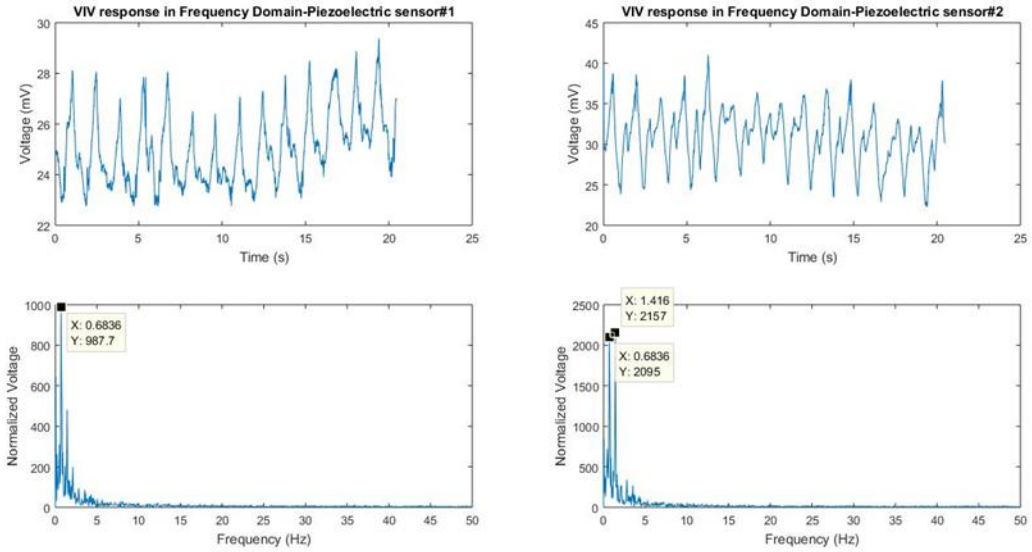

Figure 45 Case #3 of Harvester with D=0.11m

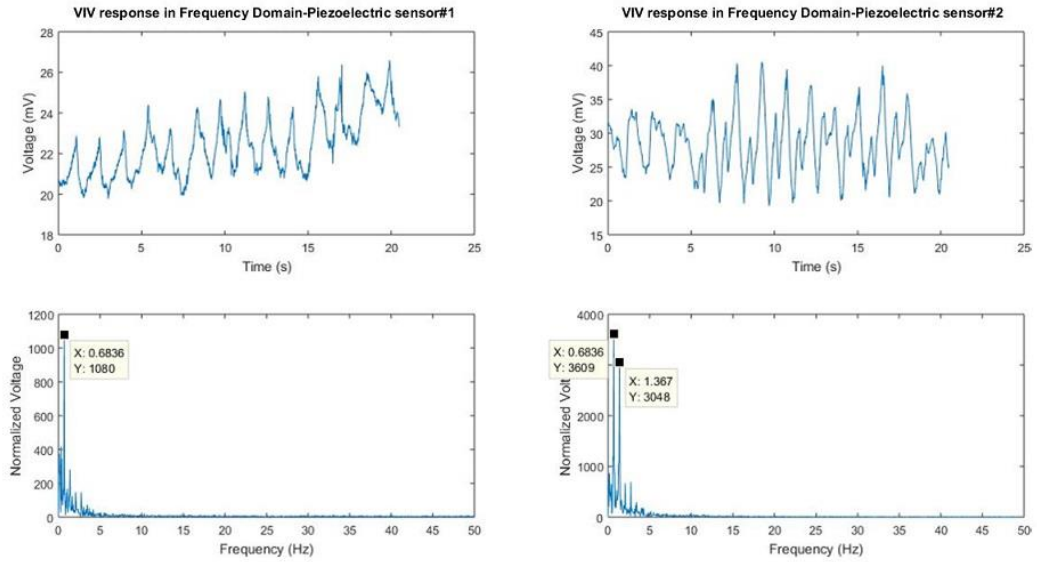

Figure 46 Case #4 of Harvester with D=0.11m

Table 6 Summary of Experimental Results

D=0.089m					
U (m/s)	f_{inline} (Hz)	$f_{crossflow}$ (Hz)	A_X (m)	A_y (m)	P_potential (mW)
0.25	1.514	0.7324	0.008	0.02	3.288393107
0.3	1.66	0.8301	0.009	0.025	3.463908395
0.35	1.758	0.8799	0.012	0.0317	3.765246219
0.4	1.807	0.9033	0.015	0.035	3.964437097
0.45	1.855	0.9277	0.0178	0.0425	4.361397696
0.5	1.904	0.9766	0.026	0.048	4.874137664
D=0.11m					
U (m/s)	f_{inline} (Hz)	$f_{crossflow}$ (Hz)	A_X (m)	A_y (m)	P_potential (mW)
0.2	1.367	0.6836	0.015	0.035	4.70603739
0.3	1.416	0.6836	0.022	0.038	4.977565287
0.35	1.465	0.7324	0.025	0.045	5.341393928
0.4	1.66	0.8301	0.033	0.056	6.084958539

The power output of the harvester as a function of flow velocity is reported in Figure 47. Overall, the harvester with diameter of 0.11m has the better performance, and with the increase of flow velocity, the energy accumulated is proportionally increasing. In the next section, the

total kinetic energy captured by the harvester is numerically calculated and then the efficiency of the harvester will be reposted.

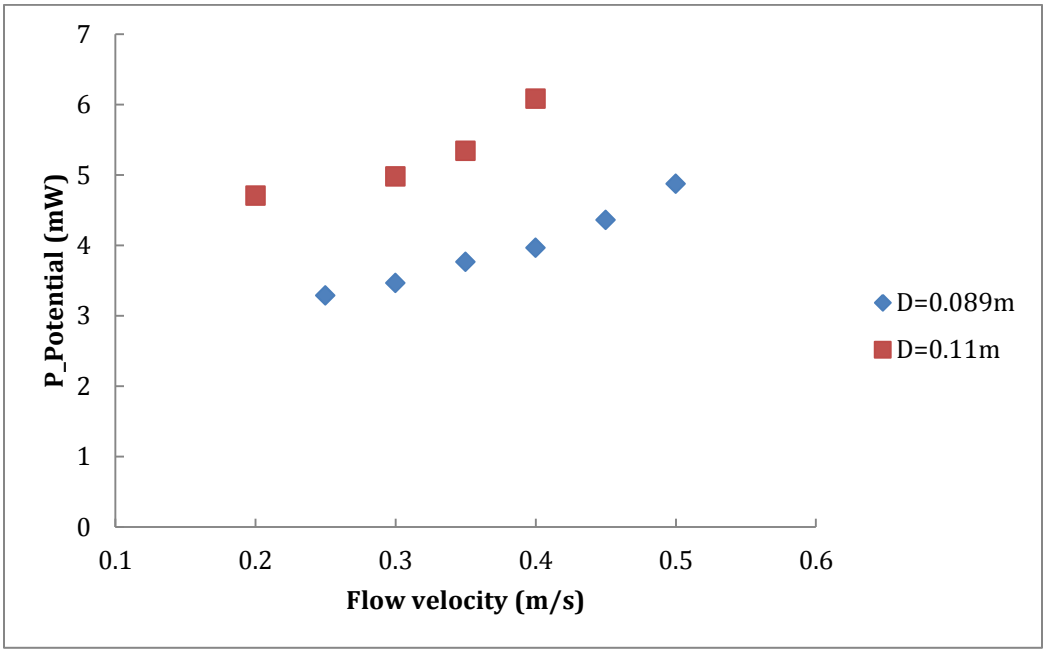

Figure 47 Harvested Power Output vs Flow velocity

5.3 Comparison

In this section, the first part focuses on the comparison between 1-way numerical model and 2-way coupled model. The second part emphasises on the comparison between the numerical results of 2-way coupled model and the experimental results.

5.3.1 Comparison between 1-way & 2-way Coupled Model

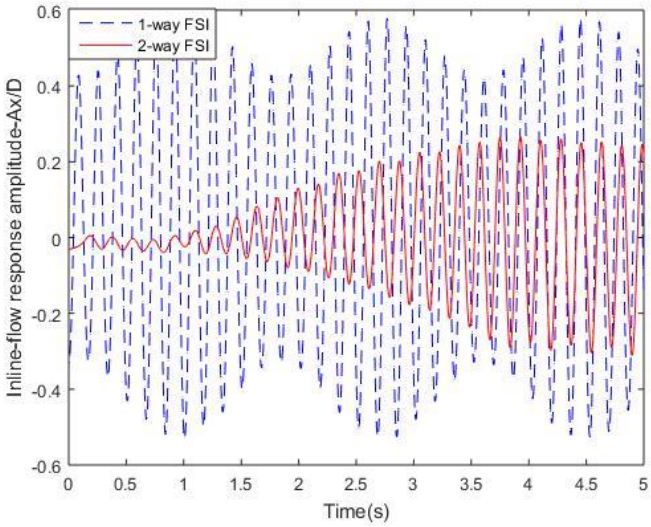

Figure 48 Inline-flow Response Amplitude (Ax/D) vs Time

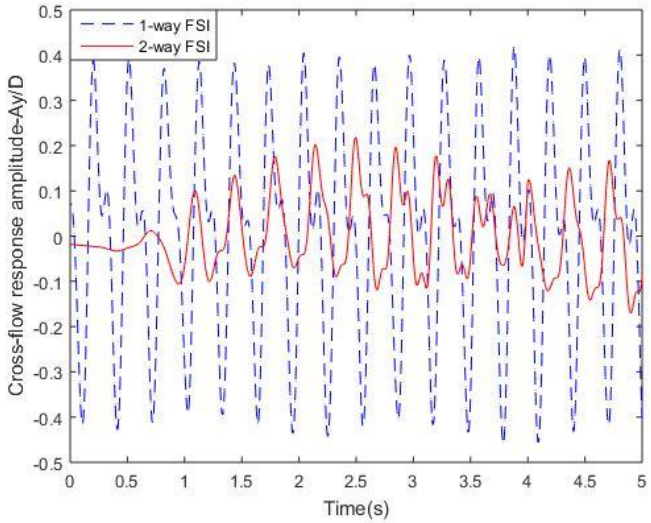

Figure 49 Cross-flow Response Amplitude (Ay/D) vs Time

Figure 48 and Figure 49 are the inline and cross-flow response amplitude ratio (A_x/D, A_y/D) vs time for 1-way analytic model and 2-way FSI model. For the VIV response frequency-wise, the results show that the VIV response frequencies for both cases are quite similar, with the 2-way FSI model has more complicated response frequency spectrum. For both of inline and cross-flow VIV responses, the 1-way coupled model obviously overestimated the response amplitude since the added mass was not being considered in this model. The 2-way FSI model includes the buoyancy and gravity force in the computation, which results in more accurate results.

5.3.2 Comparison between 2-way Coupled Model & Experimental Results

Table 7 Comparison Summary of U=0.5 m/s

	Experimental	Numerical
f_{inline} (Hz)	1.90	4.40
$f_{crossflow}$ (Hz)	0.98	1.95
A_x/D	0.026	0.033
A_y/D	0.048	0.063

Due to the limitation of the experimental facility, the maximum velocity can be achieve while maintaining a certain depth to allow the harvester fully submerged in the flume is 0.5 m/s. Thus, the simulation of U=0.5 m/s was used to compare with the experimental result. As it can be seen in the Table 7, the dominant response frequencies along the inline and cross-flow direction obtained from 2-way FSI simulation are 4.40 *Hz* and 1.95 *Hz*, respectively, which are almost two times higher than the results from experiments. However, the amplitude is similar for both cases. This overestimation of response frequency results from the consideration of edge effects, since infinite long cylinder assumption was made for the simulation, however, during the

experiments, the edge effects is affecting the VIV behavior of the bluff body. As we can conclude that, for lower inlet velocity, the edge effect is not beneficial to the VIV.

CHAPTER 6

CONCLUSION

This thesis presents numerical and experimental study of an energy harvester that utilizes 2-DOF vortex-induced vibration phenomenon. Numerical modeling was done by using two-way coupled FSI model available in ANSYS^{TM}. The frequency and amplitude of the VIV response and characteristics of the flow field are analyzed for low mass ratio and zero structural damping for wide range of Reynolds numbers. Both numerical simulations and experimental studies have shown that the proposed harvester successively harvests the kinetic energy of the flowing water and converts into vibrational energy. It is observed that there is a significant increase in the vibration amplitude and frequency when the inlet velocity increases. High level of turbulence, no matter how it can be achieved, can also result in higher power output of the harvester. The instantaneous vorticity contours indicates the vortices shed in the wake correspond to $2P_0$ shedding regime. The vortices in attached to the shear layers in the near wake region are found to be in phase with the structural response of the harvester. A single harvester is able to produce a maximum power of 41 mW. This research study has proven the feasibility of VIV for energy harvesting purposes and can be used as a reference for design of the piezoelectric energy harvester utilizing VIV response.

Suggested future work includes bluff body optimization and array testing. The proposed VIV harvesters are designed to be placed in the staggered formation in the fluid flow. With a proper alignment of these harvesters, the interaction between these harvesters will further amplify the VIV, which results in exponential increase in the response frequency (Strouhal number). In addition, further improvement can be achieved by the combination of VIV and buffeting phenomenon.

REFERENCES/BIBLIOGRAPHY

1. Kingatua, A. (2016). The How and Why of Energy Harvesting for Low-Power Applications. Retrieved from https://www.allaboutcircuits.com/technical-articles/how-why-of-energy-harvesting-for-low-power-applications/.
2. Ashok, S. (2006). Solar energy. Retrieved from https://www.britannica.com/science/solar-energy.
3. Diane, J. (2014). Geothermal Energy. Retrieved from https://edu.glogster.com/glog/geothermal-energy/1vsce2fp7i1.
4. Lund, J. W. (2018). Geothermal energy. Retrieved from https://www.britannica.com/science/geo-thermal-energy.
5. Office of Energy Efficiency & Renewable Energy. (2015). How Do Wind Turbines Work?. Retrieved from https://www.energy.gov/eere/wind/how-do-wind-turbines-work.
6. Office of Environment & Heritage. (2013). Wind Energy fact sheet. Retrieved from https://www.environment.nsw.gov.au/resources/households/WindEnergyfactsheet.pdf.
7. Kamierski, T., Steve, B (2010). Energy Harvesting Systems: Principles, Modeling and applications. Springer Publishing Company. 10.1007/978-1-4419-7566-9.
8. Sodano, H.A. (2007) A review of power harvesting using piezoelectric materials (2003–2006). Smart Mater. Struct. 16: 1–21.
9. Sodano, H.A., Inman, D.J. (2005) Comparison of piezoelectric energy harvesting devices for recharging batteries. J. Intell. Mater. Syst. Struct. 16(10): 799–807.
10. Beeby, S.P, Tudor, M.J, White, N.M. (2006) Energy harvesting vibration sources for microsystems applications. Meas. Sci. Tech. 17: 175–195.
11. MEMSnet. Retrieved from http://www.memsnet.org/material.Cited18May2010.
12. Ezeonwumelu,T.C., Ossia, C.V.,& Douglas, I.E. (2017). Fatigue Damage of Vertical Rigid Risers due to In-Line Vortex Induced Vibration in Nigeria Shallow Waters. *American Journal of Mechanical Engineering*, 5(2), 33-40.
13. Robert, D. Blevins, (2001). *Flow-Induced Vibration*, Krieger Publishing Company, p.45.
14. Abhishek, N. (2014). Power generation using lock-in vortex shedding frequencies from quasi-constant airflow, Department of Mechanical Automotive and Material Engineering, University of Windsor, Windsor, ON, Canada, *MASc. thesis*.
15. Perry,A. E., et al. (1982). "The Vortex Shedding Process Behind Two-Dimensional Bluff Bodies," Journal of Fluid Mechanics, 116, 77-90.

16. Williamson, C. H. K., and Roshko, A. (1988). "Vortex Formation in the Wake of an Oscillating Cylinder," *Journal of Fluids and Structures*, **2**, 355-381.
17. Lienhard, J. H. (1966). "Synopsis of Lift, Drag and Vortex Frequency Data for Rigid Circular Cylinders," Washingon State University, College of Engineering, Research Division Bulletin 300.
18. Nishioka, M., and Sato, H. (1978). "Mechanism of Determination of the Shedding Frequency of Vortices Behind a Cylinder at Low Reynolds Number," *Journal of Fluid Mechanics*, **89**, 49-60.
19. Huerre, P., and Monkewitz, P.A. (1990). "Local and Global Instabilities in Spatially Developing Flow," *Annual Review of Fluid Mechanics*, **22**,473-538.
20. Friehe, C. A. (1980). "Vortex Shedding from Cylinders at Low Reynolds Numbers," *Journal of Fluid Mechanics*, **100**, 237-241.
21. Roshko, A. (1954). "On the Drag and Vortex Shedding Frequency of Two-Dimensional Bluff Bodies," National Advisory Committee for Aeronautics Report NACA TM 3159, July. Also see "On the Wake and Drag of Bluff Bodies," *Journal of Aeronautical Science*, **22**, 124-135 (1955).
22. Farell, C. (1981). "Flow Around Circular Cylinder: Fluctuating Loads," *ASCE Journal of Engineering Mechanics*, **107**,565-588.
23. Bearman, P .W. (1969). "On Vortex Shedding from a Circular Cylinder in the Critical Reynolds Number Regime," *Journal of Fluid Mechanics*, **37**, 577-586.
24. Achenbach, E., and Heinecke, E. (1981). "On Vortex Shedding from Smooth and Rough Cylinders in the Range of Reynolds Numbers 6×10^3 to 5×10^6," *Journal of Fluid Mechanics*, **109**, 239-251.
25. Farell, C., and Blessmann, J. (1983). "On Critical Flow around Smooth Circular Cylinders," *Journal of Fluid Mechanics*, **136**, 375-391.
26. Jones, G. W., J. J. Cincotta, and R. W. Walker (1969). "Aerodynamic Forces on a Stationary and Oscillating Circular Cylinder at High Reynolds Numbers," National Aeronautics and Space Administration Report NASA TR R-300.
27. Roshko (1961). "Experiments on the Flow Past a Circular Cylinder at Very High Reynolds Number," *Journal of Fluid Mechanics*, **10**, 345-356.
28. Griffin (1982). "Some Recent Studies of Vortex Shedding with Application to Marine Tubulars and Risers," *Journal of Energy Resources Technology*, **104**, 2-13.
29. Nickerson, E. C., and Dias, M.A. (1981). "On the Existence if Atmospheric Vortices Downwind if Hawaii during the HAMEC Project," *Journal of Applied Meteorology*, **20**, 868-873.
30. Gsell, S., Bourguet, R., Braza, M., (2016). Two-degree-of-freedom vortex-induced vibrations of a circular cylinder at Re = 3900. *J. Fluids Struct.* 67, 156-172.

31. Jauvtis, N., Williamson, C.H.K. (2004). The effect of two degrees of freedom on vortex-induced vibration at low mass and damping. *J. Fluid Mech.* 509, 23–62.
32. Blevins, R.D., Coughran, C.S. (2009). Experimental investigation of vortex-induced vibration in one and two dimensions with variable mass, damping and Reynolds number. *J. Fluids Eng.* 131, 1–7.
33. Dahl, J.M., Hover, F.S., Triantafyllou, M.S. (2006). Two-degree-of-freedom vortex-induced vibrations using a force assisted apparatus. *J. Fluids Struct.* 22,807–818.
34. Guilmineau, E., Queutey, P. (2004). Numerical simulation of vortex-induced vibration of a circular cylinder with low mass-damping in a turbulent flow. J. Fluids Struct. 19, 449–466.
35. Williamson, C.H.K. (1988). The existence of two stages in the transition to three-dimensionality of a cylinder wake. Phys. Fluids 31, 3165–3168.
36. Williamson, C.H.K. (1989). Oblique and parallel modes of vortex shedding in the wake of a circular cylinder at low Reynolds number. J. Fluid Mech. 206,579–627.
37. Enhao W, Q. X. (2017). Three-dimensional numerical simulation of two-degree-of-freedom VIV of a circular cylinder with varying natural frequency ratios at Re=500. Journal of Fluids and Structures, 73, 162-182.
38. Facchinetti, M.L., de Langre, E., Biolley, F. (2004). Coupling structure and wake oscillators in vortex-induced vibrations. J. Fluids Struct. 19,123–140.
39. Farshidianfar, A., Zanganeh, H., (2010). A modified wake oscillator model for vortex-indcued vibration of circular cylinders for a wide range of mass-damping ratio. J. Fluids Struct. 26, 430-441.
40. Govardhan, R., Williamson, C.H.K., (2000). Modes of vortex formation and frequency response for a freely-vibrating cylinder. J. Fluid Mech. 420, 85-130.
41. Khalak, A., Williamson, C.H.K., (1999). Motions, forces and mode transitions in vortex-induced vibration at low mass-damping. J. Fluids Struct. 13, 813–851.
42. Sarpkaya, T., (1995). Hydrodynamics damping, flow-induced oscillations and biharmonic response. J. Offshore Mech. Arct. Eng. 117, 232–238.
43. Mittal, S., Singh, S. (2005). Vortex-induced vibrations at subcritical Re, J. Fluid Mech. 534, 185-194.
44. Brika, D., Laneville, A. (1993). Vortex-induced vibrations of a long flexible circular cylinder, J. Fluid Mech. 250, 481-508
45. Rostami, A., Armandei, M. (2017). Renewable energy harvesting by vortex-induced motions: Review and benchmarking of technologies, *Renewable and Sustainable Energy Reviews* **70**, 193-214.

46. Armandei M., and Fernandes A., (2016). Marine current energy extraction through buffeting, *International Journal of Marine Energy* **14**, 52-67.
47. Crivellini, A., D'Alessandro, V., & Francesco, B. (2013). A Spalart–Allmaras turbulence model implementation in a discontinuous Galerkin solver for incompressible flows. Journal of Computational Physics. 241. 388–415. 10.1016/j.jcp.2012.12.038.
48. Spalart, P. R., Jou W-H., Strelets M., Allmaras, S. R., (1997). "Comments on the Feasibility of LES for Wings and on a Hybrid RANS/LES Approach" Advances in DNS/LES, 1stAFOSR Int. Conf. on DNS/LES, Greyden Press, Columbus Oh.
49. Spalart, P., Deck, S., Shur, M., Squires, K., Strelets, M. K., and Travin, A., (2006). "A New Version of Detached-Eddy Simulation, Resistant to Ambiguous Grid Densities," Theoretical and Computational Fluid Dynamics. 0935-4964, pp.181-195.
50. Spalart, P. and Allmaras, S.R. (1992). "A One-Equation Turbulence Model for Aerodynamic Flows", AIAA Paper 92-0439.
51. Durrani N. (2018). Modelled and Resolved Turbulent Stresses Around a Circular Cylinder Using DES. In: Hoarau Y., Peng SH., Schwamborn D., Revell A. (eds) Progress in Hybrid RANS-LES Modelling. HRLM 2016. Notes on Numerical Fluid Mechanics and Multidisciplinary Design, vol 137. Springer, Cham.
52. Roshko, A., (1961). "Experiments on the Flow past a Circular Cylinder at Very High Reynolds Number", Journal of Fluid Mechanics, Vol. 10, No. 3, pp. 345-356.
53. Nunen, J. V. (1974). "Pressure and Forces on a Circular Cylinder in a Cross flow at High Reynolds Numbers", Flow Induced Structural Vibrations, Springer-Verlag, Berlin, pp. 748-754.
54. Travin, A., Shur. M., Strelets, M. and Spalart, P. (1999) "Detached-Eddy Simulation past a Circular Cylinder", Journal of Flow, Turbulence and Combustion, 63, 269-291.
55. Cantwell, B. and Coles, D. (1983). "An experimental study of entrainment and transport in the turbulent near wake of a circular cylinder."Journal of Fluid Mechanics, Vol. 136, pp. 321-374.
56. Chaaban, F. B., Assi, R., & Abdo, J. (2007). A century of energy conversion — an environmental overview. International Journal of Environmental Studies 47, 133-142.
57. Harries, D., McHenry, M., Jennings, P., & Thomas, C. (2011). Hydro, tidal and wave energy in Australia. International Journal of Environmental Studies 63, 803-814.
58. Bernitsas, M. M, Raghavan, K, Ben-Simon, Y, Garcia, E. M. (2008). VIVACE (Vortex Induced Vibration Aquatic Clean Energy): a new concept in generation of clean and renewable energy from fluid flow. *Journal of Offshore Mechanics and Arctic Engineering* **130(4)**, 041101.
59. Chang, C.C., Kumar, R.A., Bernitsas M.M. (2011). VIV and galloping of single circular cylinder with surface roughness at $3\times10^4 < Re < 1.2\times10^5$, *Ocean Engineering* **38**, 1713-1732.

60. Ding, L., Zhang, L., Bernitsas, M. M., & Chang, C. (2016). Numerical simulation and experimental validation for energy harvesting of single-cylinder VIVACE converter with passive turbulence control. *Renewable Energy* **85**, 1246-1259.
61. Chang, C.C., Bernitsas, M.M., (2011). Design of VIVACE converter using PTC, [Presented at the] 30th OMAE 2011 Conf., Rotterdam, The Netherlands.
62. Park, H., Kumar, R.A., Bernitsas, M. M. (2013). Enhancement of flow-induced motion of rigid circular cylinder on springs by localized surface roughness at $3\times10^4 < Re < 1.2\times10^5$, *Ocean Engineering* **72**, 403-415.
63. Liu, H, Qian, Y, Lee, C. (2013). A multi-frequency vibration-based MEMS electromagnetic energy harvesting device. *Sensors and Actuators A: Physical Journal* **204**, 37–43.
64. Dung-An, W; Chun-Yuan, C and Huy-Tuan, P. (2012). Electromagnetic energy harvesting from vibrations induced by Karman vortex street; Mechatronics; Volume 22; pages 746-756
65. Sodano, H. A, Inman, D. J, Park, G. (2005). Comparison of piezoelectric energy harvesting devices for recharging batteries. *Journal of Intelligent Material Systems and Structures* **16(10)**, 799–807.
66. Lefeuvre, E, Badel, A, Richard, C, Guyomar, D. (2005). Piezoelectric energy harvesting device optimization by synchronous electric charge extraction. *Journal of Intelligent Material Systems and Structures* **16(10)**, 865–876.
67. Liu, J.Q, Fang, H. B, Xu, Z. Y, Mao, X. H, Shen, X. C, Chen, D, et al. (2008). A MEMS-based piezoelectric power generator array for vibration energy harvesting. *Microelectronics Journal* **39(5)**, 802–6.
68. Chen, Z., Yang, Y., Lu, Z., Luo, Y., (2013). Broadband characteristics of vibration energy harvesting using one-dimensional phononic piezoelectric cantilever beams. *Physica B: Condensed Matter* **410**, 5–12.
69. Roundy, S, Leland, E. S, Baker, J., Carleton, E., Reilly, E., Lai, E., et al., (2005). Improving power output for vibration-based energy scavengers. *IEEE Pervasive Computing* **4(1)**, 28–36.
70. Sarpkaya T, (2004). A critical review of the intrinsic nature of vortex-induced vibrations, *Journal of Fluids and Structures* **19,** 389-447.
71. Zhang, D., (2017). "Comparison of Various Turbulence Models for Unsteady Flow around a Finite Circular Cylinder at Re=20000", Journal of Physics: Conf. Series **910**-012027.
72. Menter, F.R, Kuntz, M., Langtry, R. (2003). "Ten years of industrial experience with the SST turbulence model". Turbulence, Heat and Mass Transfer, 4(1), 625-632.
73. Menter, F.R. (1994). "Two-equation eddy-viscosity turbulence models for engineering applications". AIAAJournal, 32(8), 1598-1605.

74. Achenbach, E. (1968). Achenbach, E.: Distribution of Local Pressure and Skin Friction around a Circular Cylinder in Cross-Flow up to Re = 5×106. Journal of Fluid Mechanics 34(4), 625-639. Journal of Fluid Mechanics. 34. 625 - 639. 10.1017/S0022112068002120.

75. Morse, T., Williamson, C. (2009). Fluid forcing, wake modes and transitions for a cylinder undergoing controlled oscillations. *J Fluids Struct* 25(4):697–712.

APPENDICES

Appendix A: MATLAB Code

1. Run EOM

```
clear
clc
g=9.81;
m=1;%kg%D=0.05 m=0.16kg/D=0.09 m=0.3kg/D=0.15 m=0.6kg/D=0.2 m=1kg
k1=150;%spring coefficient
D=0.2;%Diameter of the cylinder
l=0.7;%Original Length of the spring
options=odeset('RelTol',1e-9,'AbsTol',1e-9);
[t,xy]=ode15s(@(t,xy)CylinderEOM3(t,xy,g,k1,l,m),[0 10],[0 0 0 0],options);

Disp_m=sqrt(xy(:,1).^2+xy(:,3).^2);
figure(1)
plot(t,xy(:,3))
xlabel('Time(s)')
ylabel('Cross-flow Displacement(m)')
legend('Diamter of Cylinder=0.20m')
title('Cross-flow Displacement vs Time')
figure(2)
plot(t,xy(:,1))
xlabel('Time(s)')
ylabel('Inline-flow Displacement (m)')
legend('Diameter of Cylinder=0.20m')
title('Inline-flow Displacement vs Time')
figure(3)
plot(t,Disp_m)
xlabel('Time(s)')
ylabel('Displacement(m)')
%Length of the spring
%lc
   %lc1=sqrt(xy(:,1).^2+(l-xy(:,3)).^2)
   lc1=sqrt((xy(:,1)-l).^2+xy(:,3).^2);

   %lc2=sqrt(xy(:,3).^2+(l-xy(:,1)).^2)
   lc2=sqrt(xy(:,1).^2+(l-xy(:,3)).^2);

   lc3=sqrt(xy(:,1).^2+(l+xy(:,3)).^2);
   %lc3=sqrt(xy(1).^2+(l+xy(3)).^2);

   lc4=sqrt(xy(:,3).^2+(l+xy(:,1)).^2);
   %lc4=sqrt(xy(3).^2+(xy(1)+l).^2);

   %Energy in spring
    E1=0.5*k1*(lc1-l).^2;
    E2=0.5*k1*(lc2-l).^2;
    E3=0.5*k1*(lc3-l).^2;
```

```
    E4=0.5*k1*(lc4-l).^2;
    E=E1+E2+E3+E4
    %figure(4)
    %plot(t,E)
    %trapz(t,E)/t(length(t))
```

2. Equation of Motion of the Cylinder

```
function dxy=CylinderEOM3(t,xy,g,k1,l,m)
    dxy(1,:)=xy(2);%x1 displacment to velocity
    dxy(3,:)=xy(4);%y1

    %lc1xy=sqrt(l-(xy(1)).^2+xy(3).^2);%old
    lc1xy=sqrt(l-(xy(1,:)).^2+xy(3,:).^2);%old
    %lc1xy=sqrt(xy(1).^2+(l-xy(3)).^2);%new-compression
    lc2xy=sqrt(xy(1,:).^2+(l-xy(3,:)).^2);%old
    %lc2xy=sqrt(xy(3).^2+(l-xy(1)).^2);%new-extension
    lc3xy=sqrt(xy(1,:).^2+(l+xy(3,:)).^2);%new-extension
    %lc3xy=sqrt(xy(1).^2+(l+xy(3)).^2);%old
    lc4xy=sqrt(xy(3,:).^2+(l+xy(1,:)).^2);%new-compression
    %lc4xy=sqrt(xy(3).^2+(xy(1)+l).^2);%old

    % forces' components
    %xy
    F1xxy=k1*(lc1xy-l)*(l-xy(1,:))./lc1xy;                F1yxy=-k1*(lc1xy-
l)*xy(3,:)./lc1xy;
    %F1xxy=k1*(lc1xy-l)*xy(1)./lc1xy;                     F1yxy=-k1*(lc1xy-
l)*(l-xy(3))./lc1xy;
    F2xxy=-k1*(lc2xy-l)*xy(1,:)./lc2xy;                   F2yxy=k1*(lc2xy-
l)*(l-xy(3,:))./lc2xy;
    %F2xxy=-k1*(lc2xy-l)*(l-xy(1,:))./lc2xy;               F2yxy=k1*(lc2xy-
l)*xy(3,:)./lc2xy;
    F3xxy=-k1*(lc3xy-l)*xy(1,:)./lc3xy;                   F3yxy=-k1*(lc3xy-
l)*(l+xy(3,:))./lc3xy;
    F4xxy=-k1*(lc4xy-l)*(l+xy(1,:))./lc4xy;               F4yxy=-k1*(lc4xy-
l)*xy(3,:)./lc4xy;

    %Drag Force (Function of t)

     %Fdrag=5.3413+0.6*sin(60*t-5*pi/8)-0.8*cos(60*t-5*pi/8);%D=0.06m
     %Fdrag=8+1.2*sin(41*t-5*pi/8)-0.4*cos(41*t-5*pi/8);%Original
data%D=0.09m
     %Fdrag=12.6+2*sin(41*t-5*pi/8)-0.4*cos(41*t-5*pi/8);%OLD%D=0.09m
     %Fdrag=13.3529+2.1*sin(18.42*t-5*pi/8)-1.1*cos(18.42*t-5*pi/8);%D=0.15m
     %Fdrag=17.8+3*sin(13.8*t-5*pi/8)-1.5*cos(13.8*t-
5*pi/8);%D=0.20m%Interpolate
     Fdrag=17.5+3*sin(10.1*t-pi/2)-1.5*cos(10.1*t-pi/2);%D=0.2m Original data

     %D=0.09m, v=0.2-1m/s
     %Fdrag=1.6+0.18*sin(8.38*t-5*pi/8)-0.18*cos(8.38*t-5*pi/8);%v=0.2
     %Fdrag=3.2+0.36*sin(16.75*t-5*pi/8)-0.36*cos(16.75*t-5*pi/8);%v=0.4
     %Fdrag=4.8+0.55*sin(25.12*t-5*pi/8)-0.55*cos(25.12*t-5*pi/8);%v=0.6
     %Fdrag=6.4+0.72*sin(33.5*t-5*pi/8)-0.72*cos(33.5*t-5*pi/8);%v=0.8
     %Fdrag=8+1.2*sin(41*t-pi/2)-0.4*cos(41*t-pi/2);%v=1
```

```
     %Lift Force (Function of t)
     %Flift=0.1221-5.3*sin(20.5*t-3*pi/8)-8.3345*cos(20.5*t-3*pi/8);%Original
data(D=0.09)
     %Flift=-0.1386-6*sin(30*t-3*pi/8)+3*cos(30*t-
3*pi/8);%(D=0.06) %Interpolate
     %Flift=-0.4269-16*sin(9.21*t-3*pi/8)+4*cos(9.21*t-
3*pi/8);%(D=0.15) %Intepolate
     %Flift=-0.5748-20*sin(6.9*t-3*pi/8)+8*cos(6.9*t-
3*pi/8);%(D=0.2)%Intepolate
     Flift=-3.5-14*sin(5.05*t-7*pi/8)+14*cos(5.05*t-7*pi/8);%Original
data(D=0.2)

     %Different Velocity sheet1 (D=0.09m)
     %Flift=0.013-1*sin(4.19*t-3*pi/8)-1.7*cos(4.19*t-3*pi/8);%v=0.2
     %Flift=0.026-2.13*sin(8.377*t-3*pi/8)-3.45*cos(8.377*t-3*pi/8);%v=0.4
     %Flift=0.0391-3.2*sin(12.56*t-3*pi/8)-5.15*cos(12.56*t-3*pi/8);%v=0.6
     %Flift=0.052-4.26*sin(16.75*t-3*pi/8)-6.9*cos(16.75*t-3*pi/8);%v=0.8
     %Flift=0.1221-5.3*sin(20.5*t-3*pi/8)-8.3345*cos(20.5*t-3*pi/8);%v=1

    %EOM of Cylinder
    %x-Direction
    dxy(2)=Fdrag/m+F1xxy/m+F2xxy/m+F3xxy/m+F4xxy/m;
    %y-Direction
    dxy(4)=Flift/m-g+F1yxy/m+F2yxy/m+F3yxy/m+F4yxy/m;

    %MASS
    %x-Direction
%     dxy(6)=-g-F1xxy/M-F2xxy/M-F3xxy/M+F4xxy/M-F1xzx/M-F2xzx/M-
F5xzx/M+F6xzx/M-C1*(xy(6)-xy(2))/M;
%     %y-Direction
%     dxy(8)=F1yxy/M-F2yxy/M+F3yxy/M+F4yxy/M+F3yyz/M+F4yyz/M+F5yyz/M-F6yyz/M-
C2*(xy(8)-xy(4))/M;
%     %Z-Direction
%     dxy(12)=F1zzx/M-F2zzx/M+F5zzx/M+F6zzx/M-F3zyz/M-
F4zyz/M+F5zyz/M+F6zyz/M-C1*(xy(12)-xy(10))/M;
%
    %dxy=dxy';
end
```

3. Fast Fourier Transformation

```
% Inline
clc
clear
dataset1= xlsread('Displacement_cylinder_Inline_flow_1','Sheet1','A2:B4097');
t1=dataset1(:,1);
Ax=dataset1(:,2);
Ax1=detrend(Ax);
Fs=1000;
Ts=1/Fs;
dt=0:Ts:4.095-Ts;
nfft1=length(Ax1);
ff1=fft(Ax1,nfft1);
fff1=ff1(1:nfft1/2);
xfft1=Fs*(0:nfft1/2-1)/nfft1;
%f1 = figure;
```

```
subplot(2,2,1);
plot(t1,Ax);
xlabel('Time (s)');
ylabel('Amplitude (m)');
title('Inline VIV Response in Time Domain')
subplot(2,2,3);
%f2 = figure;
plot(xfft1,abs(fff1));
xlabel('Frequency (Hz)');
ylabel('Normalized Amplitude');
title('Inline VIV Response in Frequency Domain');
axis([0 50 0 50]);
% Crossflow
dataset2= xlsread('Displacement_cylinder_Crossflow_1','Sheet1','A2:B4097');
t2=dataset2(:,1);
Ay=dataset2(:,2);
Ay1=detrend(Ay);
Fs=1000;
Ts=1/Fs;
dt=0:Ts:4.095-Ts;
nfft2=length(Ay1);
ff2=fft(Ay1,nfft2);
fff2=ff2(1:nfft2/2);
xfft2=Fs*(0:nfft2/2-1)/nfft2;
%f3 = figure;
subplot(2,2,2);
plot(t1,Ay);
xlabel('Time (s)');
ylabel('Amplitude (m)');
title('Crossflow VIV Response in Time Domain')
subplot(2,2,4);
%f4 = figure
plot(xfft2,abs(fff2));
xlabel('Frequency (Hz)');
ylabel('Normalized Amplitude');
title('Crossflow VIV Response in Frequency Domain');
axis([0 50 0 120]);
```

4. Root-mean-square calculation

```
clear
dataset1= xlsread('Displacement_cylinder_Inline_flow_1','Sheet1','A2:B4097');
t1=dataset1(:,1);
Ax=dataset1(:,2);
Ax_sum=sum(Ax.^2);
Ax_rms=sqrt(Ax_sum/(numel(Ax)+1))
Axd=Ax_rms/0.089
dataset2= xlsread('Displacement_cylinder_Crossflow_1','Sheet1','A2:B4097');
t2=dataset2(:,1);
Ay=dataset2(:,2);
Ay_sum=sum(Ay.^2);
Ay_rms=sqrt(Ay_sum/(numel(Ay)+1))
Ayd=Ay_rms/0.089
```

5. 1-way coupled vs 2-way coupled comparison

```
clear
clc
g=9.81;
m=0.3;%kg%D=0.05 m=0.16kg/D=0.09 m=0.3kg/D=0.15 m=0.6kg/D=0.2 m=1kg
k1=200;%spring coefficient
D=0.09;%Diameter of the cylinder
l=0.15;%Original Length of the spring
options=odeset('RelTol',1e-9,'AbsTol',1e-9);
[t,xy]=ode15s(@(t,xy)CylinderEOM3(t,xy,g,k1,l,m),[0 5],[0 0 0 0],options);

Disp_m=sqrt(xy(:,1).^2+xy(:,3).^2);
figure(1)
dataset1= xlsread('Displacement_cylinder_Crossflow_1','Sheet3','A1:B5001');
t1=dataset1(:,1);
Ay=dataset1(:,2);
Ayd=detrend(Ay);
Ayd1=Ayd.*1.8;
Ayd2=detrend(xy(:,3)/0.09);
plot(t,Ayd2,'b--',t1,Ayd1,'r')
xlabel('Time(s)')
%ylabel('Cross-flow Displacement(m)')
ylabel('Cross-flow response amplitude-Ay/D')
%legend('Diamter of Cylinder=0.09m')
legend('1-way FSI','2-way FSI')
%title('Cross-flow Response Amplitude vs Time')

figure(2)
dataset2= xlsread('Displacement_cylinder_Inline_flow_1','Sheet3','A1:B5001');
t2=dataset2(:,1);
Ax=dataset2(:,2);
Axd=detrend(Ax);
Axd2=detrend(xy(:,1)/0.18);
plot(t,Axd2,'b--',t2,Axd,'r')
xlabel('Time(s)')
%ylabel('Inline-flow Displacement (m)')
ylabel('Inline-flow response amplitude-Ax/D')
%legend('Diameter of Cylinder=0.09m')
legend('1-way FSI','2-way FSI')
%title('Inline-flow Response Amplitude vs Time')
%figure(3)
%plot(t,Disp_m)
%xlabel('Time(s)')
%ylabel('Displacement(m)')
```

6. Harvested energy calculation

```
% Inline
clc
clear
dataset1= xlsread('Inline-flow Displacement-V05','Sheet3','A2:B5001');
t1=dataset1(:,1);
Ax=dataset1(:,2);
f1= figure;
subplot(2,1,1);
plot(t1,Ax);   %Displacement vs Time
xlabel('Time (s)');
ylabel('Amplitude (m)');
title('Inline VIV Response amplitude in Time Domain')
dt=0.001;
vel_x=gradient(Ax)./dt;%Velocity vs Time
acc_x=gradient(vel_x)./dt;%Accerleration vs Time
subplot(2,1,2);
plot(t1,vel_x);
xlabel('Time (s)');
ylabel('Velocity (m/s)');
title('Inline VIV Velocity in Time Domain')
%plot(t1,acc_x);
E_k_x=1/2*(0.089^2*pi/4*0.01*998.3)*(vel_x.^2);%Kinetic energy=1/2*m*v.^2
%subplot(2,2,3);
%plot(t1,E_k)
%subplot(2,2,4);
E_p_x=(0.089^2*pi/4*0.01*998.3)*9.81*Ax;%Potential energy=m*g*h

E_P_x=trapz(E_p_x)/t1(length(t1));
%trapz(t,E)/t(length(t))
E_K_x=trapz(E_k_x)/t1(length(t1));

e_x=E_P_x/E_K_x*100

dataset2= xlsread('Cross-flow Displacement-V05','Sheet2','A2:B5001');
t2=dataset2(:,1);
Ay=dataset2(:,2);
f2= figure;
subplot(2,1,1);
plot(t1,Ay);   %Displacement vs Time
xlabel('Time (s)');
ylabel('Amplitude (m)');
title('Crossflow VIV Response amplitude in Time Domain')
dt=0.001;
vel_y=gradient(Ay)./dt;%Velocity vs Time
acc_y=gradient(vel_y)./dt;%Accerleration vs Time
subplot(2,1,2);
plot(t1,vel_y);
xlabel('Time (s)');
ylabel('Velocity (m/s)');
title('Crossflow VIV Velocity in Time Domain')
%plot(t1,acc_x);
E_k_y=1/2*(0.089^2*pi/4*0.01*998.3)*(vel_y.^2);%Kinetic energy=1/2*m*v.^2
%subplot(2,2,3);
%plot(t1,E_k)
```

```
%subplot(2,2,4);
E_p_y=(0.089^2*pi/4*0.01*998.3)*9.81*Ay;%Potential energy=m*g*h

E_P_y=trapz(E_p_y)/t2(length(t2));
%trapz(t,E)/t(length(t))
E_K_y=trapz(E_k_y)/t2(length(t2));

e_y=E_P_y/E_K_y*100
```

7. Video Writer

```
clc
workingDir = tempname;
mkdir(workingDir)
mkdir(workingDir,'Image_contour')
imageNames = dir(fullfile(workingDir,'Image_contour','*.jpg'));
%imageNames = {imageNames.name}';
outputVideo = VideoWriter(fullfile(workingDir,'animation.avi'));
%outputVideo.FrameRate = shuttleVideo.FrameRate;
open(outputVideo)
for ii = 1:length(imageNames)
   img = imread(fullfile(workingDir,'Image_contour',imageNames{ii}));
   writeVideo(outputVideo,img)
end
close(outputVideo)
```

Appendix B: Figures

1. Additional information of 3-D FSI simulation

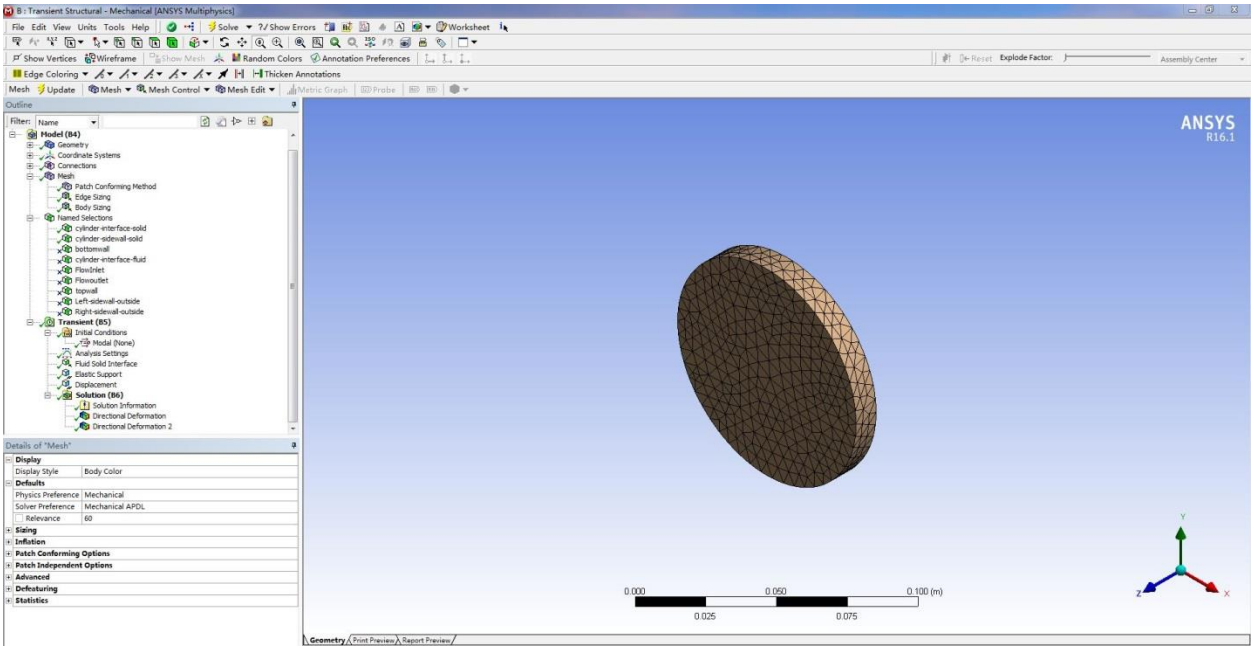

Figure B. 1 Overview of Transient Structural Module

Properties of DataTransfer : Data Transfer

	A	B
1	Property	Value
2	Source	
3	Participant	Transient Structural
4	Region	Fluid Solid Interface
5	Variable	Incremental Displacement
6	Target	
7	Participant	Fluid Flow (Fluent)
8	Region	cylinder-interface-fluid
9	Variable	displacement
10	Data Transfer Control	
11	Transfer At	Start Of Iteration
12	Under Relaxation Factor	1
13	RMS Convergence Target	0.01
14	Ramping	None

Figure B. 2 3-D FSI Data Transfer #1

Properties of DataTransfer : Data Transfer 2

	A	B
1	Property	Value
2	Source	
3	Participant	Fluid Flow (Fluent)
4	Region	cylinder-interface-fluid
5	Variable	force
6	Target	
7	Participant	Transient Structural
8	Region	Fluid Solid Interface
9	Variable	Force
10	Data Transfer Control	
11	Transfer At	Start Of Iteration
12	Under Relaxation Factor	1
13	RMS Convergence Target	0.01
14	Ramping	None

Figure B. 3 3-D FSI Data Transfer #2

Outline of Schematic D1: System Coupling

	A
1	System Coupling
2	Setup
3	Analysis Settings
4	Participants
5	Transient Structural
6	Regions
7	Fluid Solid Interface
8	Fluid Flow (Fluent)
9	Regions
10	cylinder-interface-fluid
11	Data Transfers
12	Data Transfer
13	Data Transfer 2
14	Execution Control
15	Co-Sim. Sequence
16	Debug Output
17	Expert Settings
18	Intermediate Restart Data Output
19	Solution
20	Solution Information
21	System Coupling
22	Transient Structural
23	Fluid Flow (Fluent)
24	Chart Monitors

Properties of Analysis Settings

	A	B
1	Property	Value
2	Analysis Type	Transient
3	Initialization Controls	
4	Coupling Initialization	Program Controlled
5	Duration Controls	
6	Duration Defined By	End Time
7	End Time [s]	15
8	Step Controls	
9	Step Size [s]	0.001
10	Minimum Iterations	1
11	Maximum Iterations	15

Figure B. 4 Overview of System Coupling Module

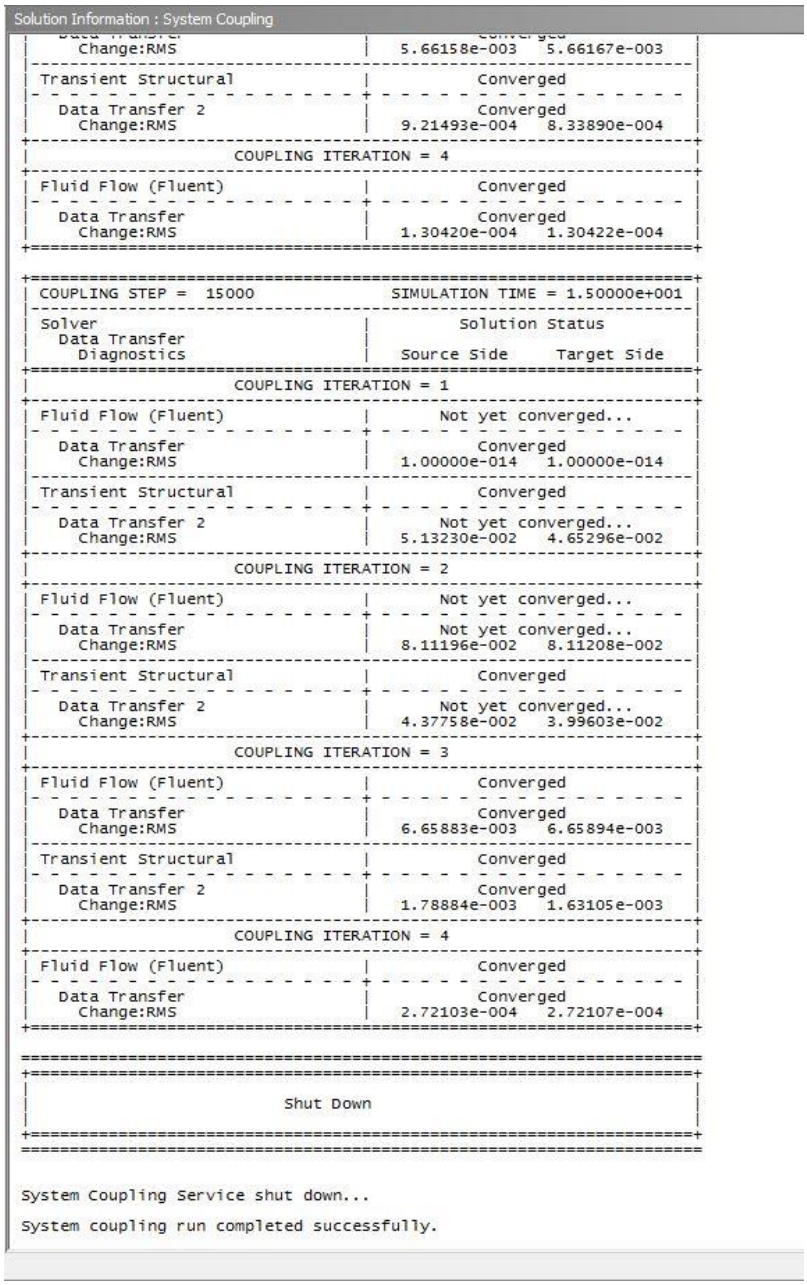

Figure B. 5 Solution information of 3-D FSI Simulation

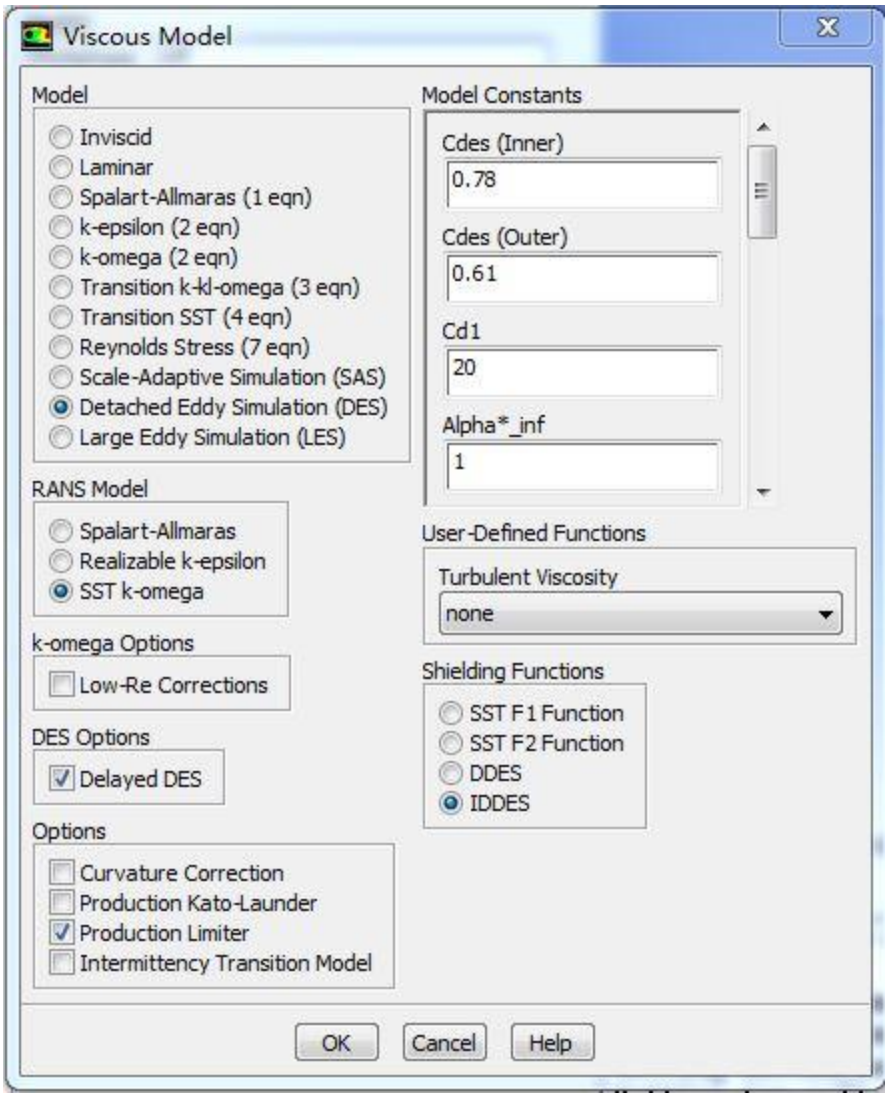

Figure B. 6 Viscous Model of 3-D FSI Simulation

2. 2-D Preliminary Result

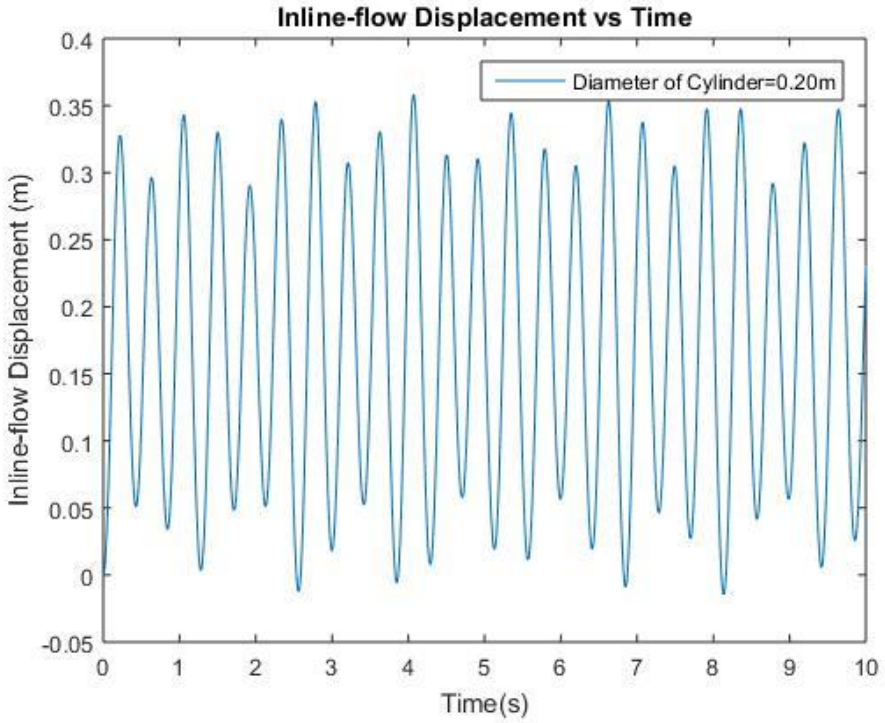

Figure B. 7 Inline-flow Displacement vs Time for Cylinder with D=0.2m-(U=1 m/s)

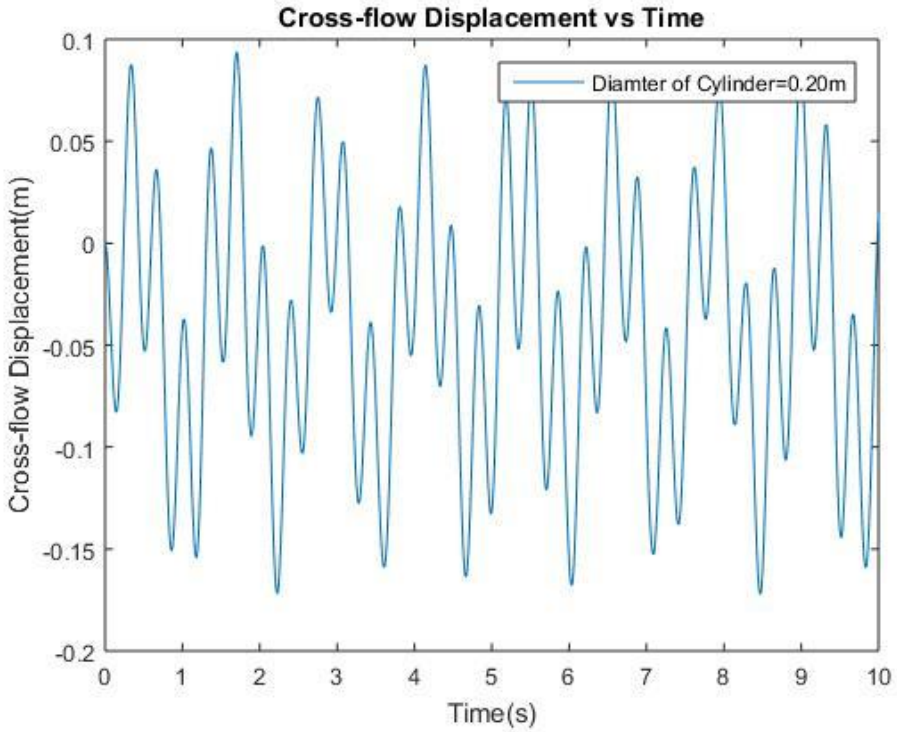

Figure B. 8 Cross-flow Displacement vs Time for Cylinder with D=0.2m-(U=1 m/s)

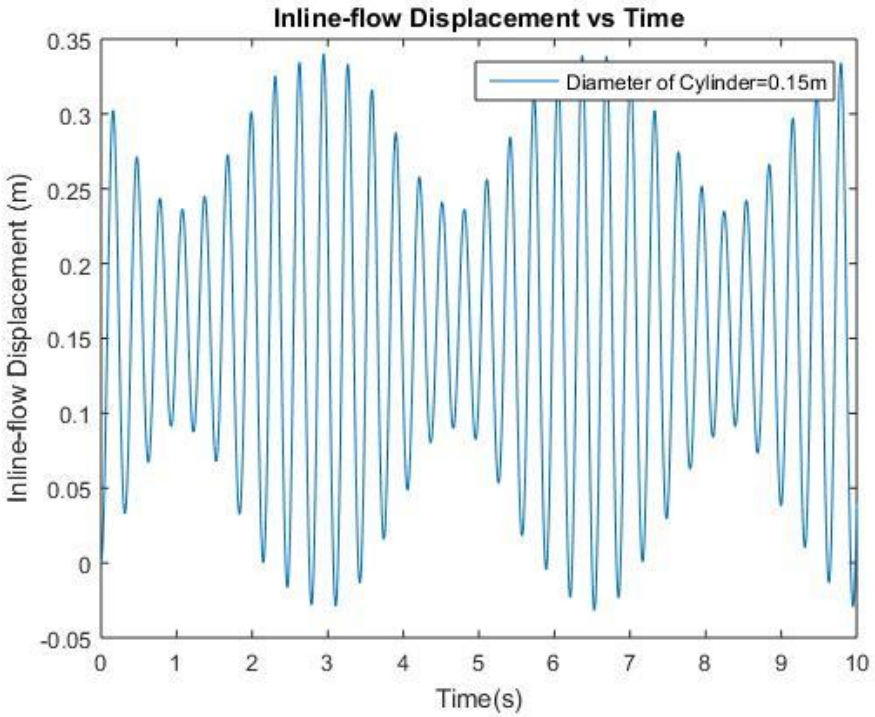

Figure B. 9 Inline-flow Displacement vs Time for Cylinder with D=0.15m-(U=1 m/s)

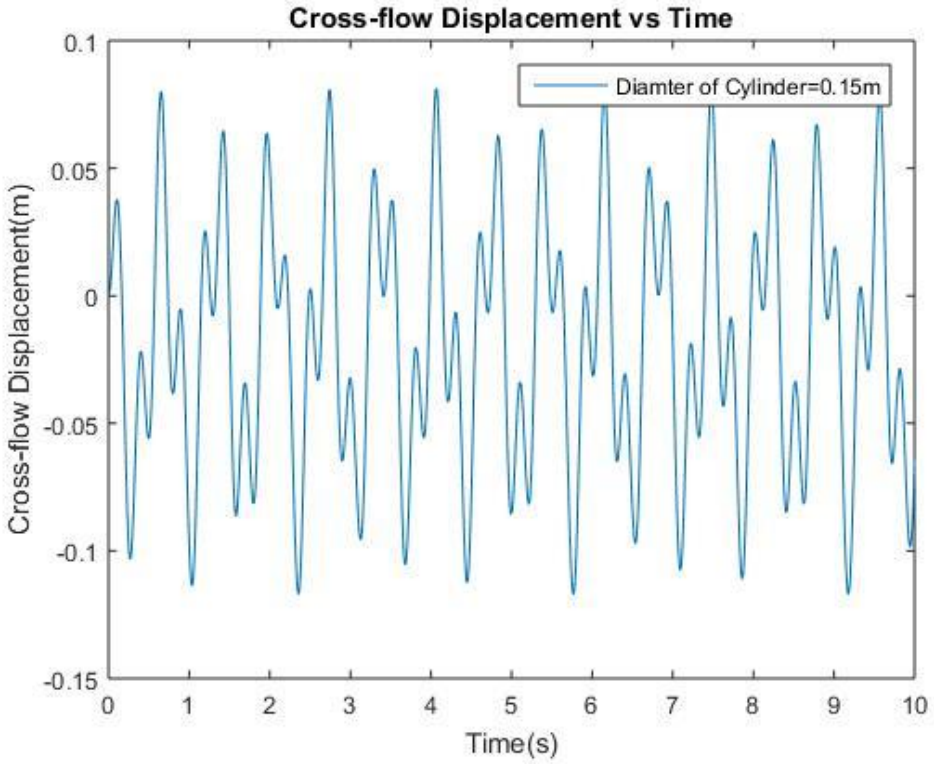

Figure B. 10 Cross-flow Displacement vs Time for Cylinder with D=0.15m-(U=1 m/s)

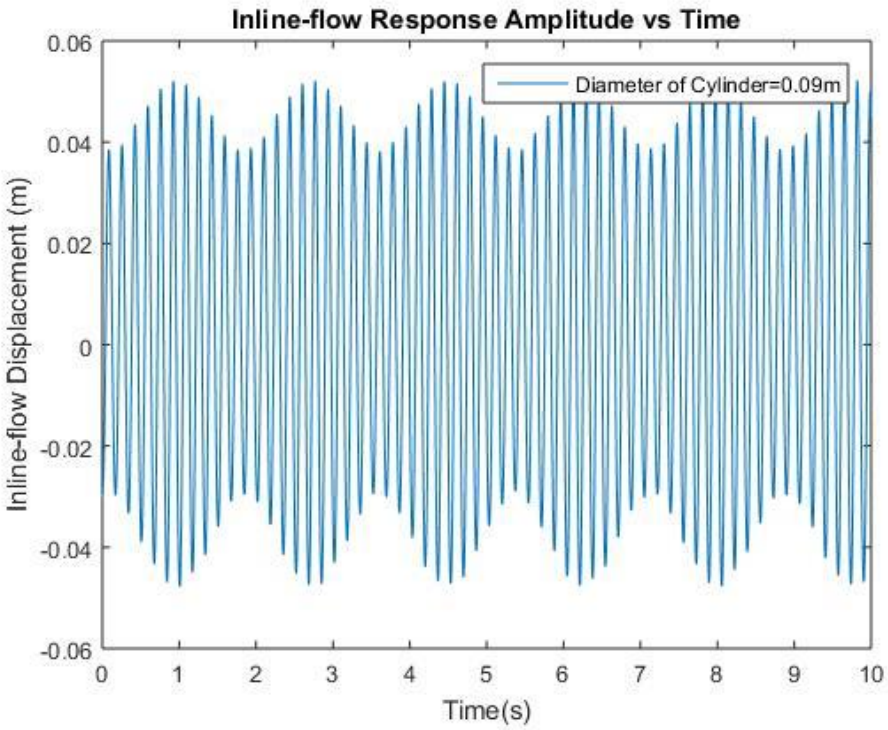

Figure B. 11 Inline-flow Displacement vs Time for Cylinder with D=0.09m-(U=1 m/s)

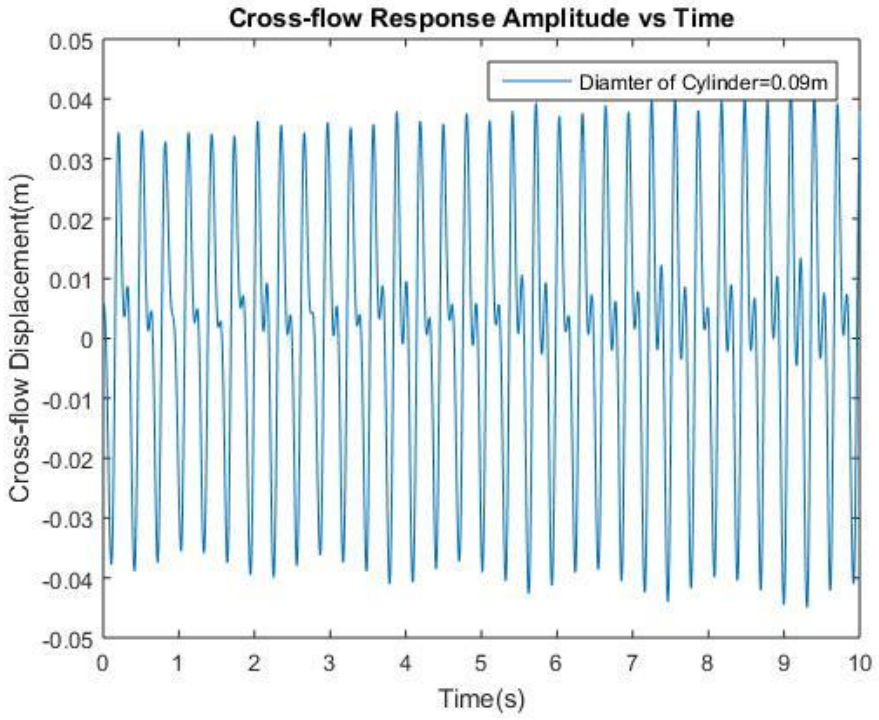

Figure B. 12 Cross-flow Displacement vs Time for Cylinder with D=0.09m-(U=1 m/s)

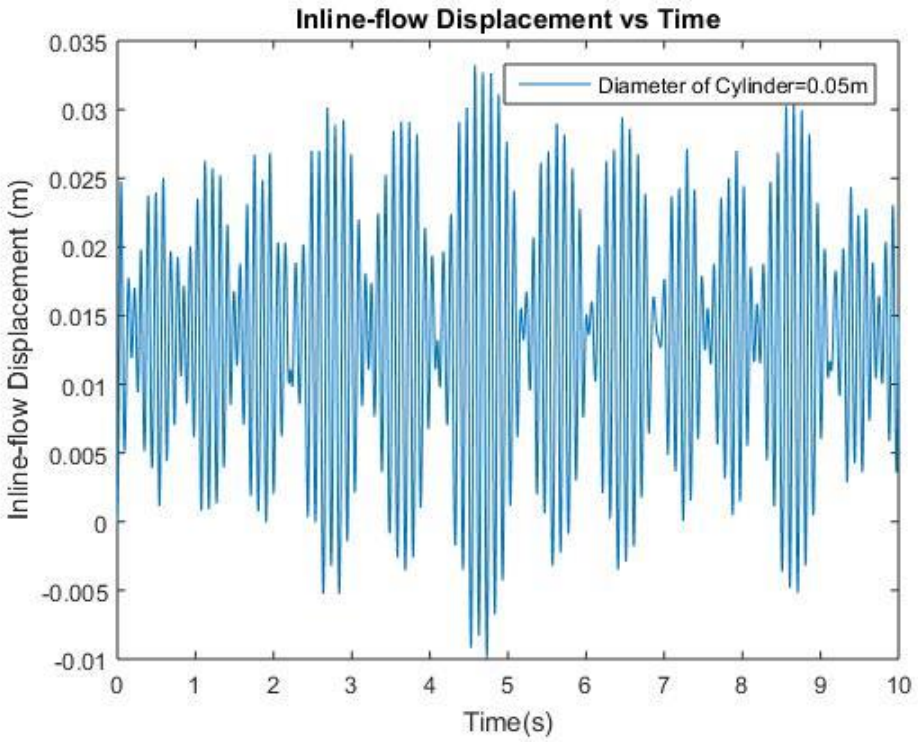

Figure B. 13 Inline-flow Displacement vs Time for Cylinder with D=0.05m-(U=1 m/s)

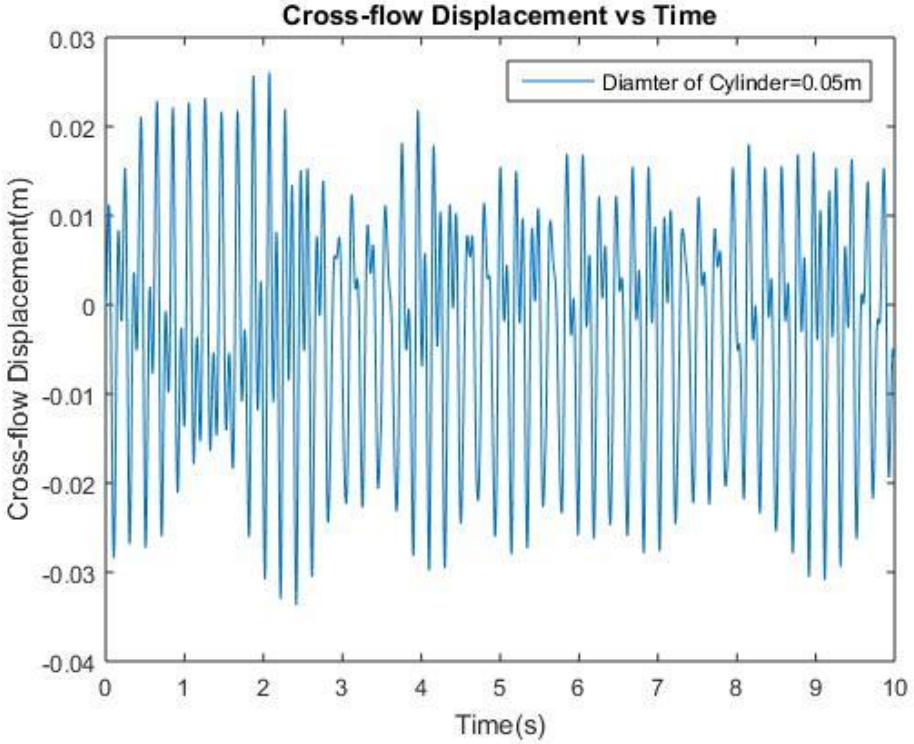

Figure B. 14 Cross-flow Displacement vs Time for Cylinder with D=0.05m-(U=1 m/s)

3. FFT analysis of 3-D stationary model

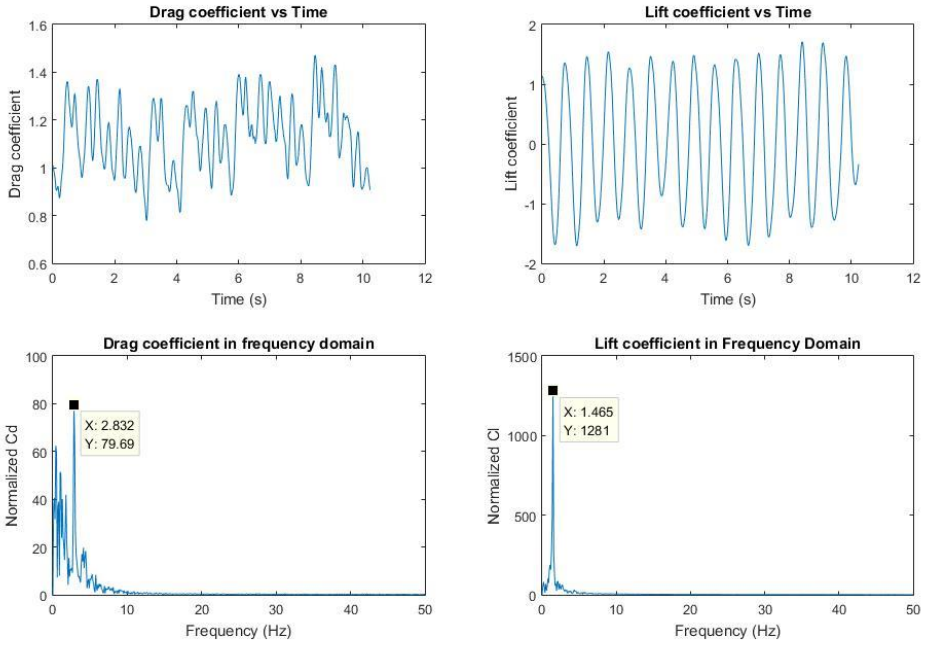

Figure B. 15 FFT Analysis of Drag and Lift Coefficients-U=0.5 m/s

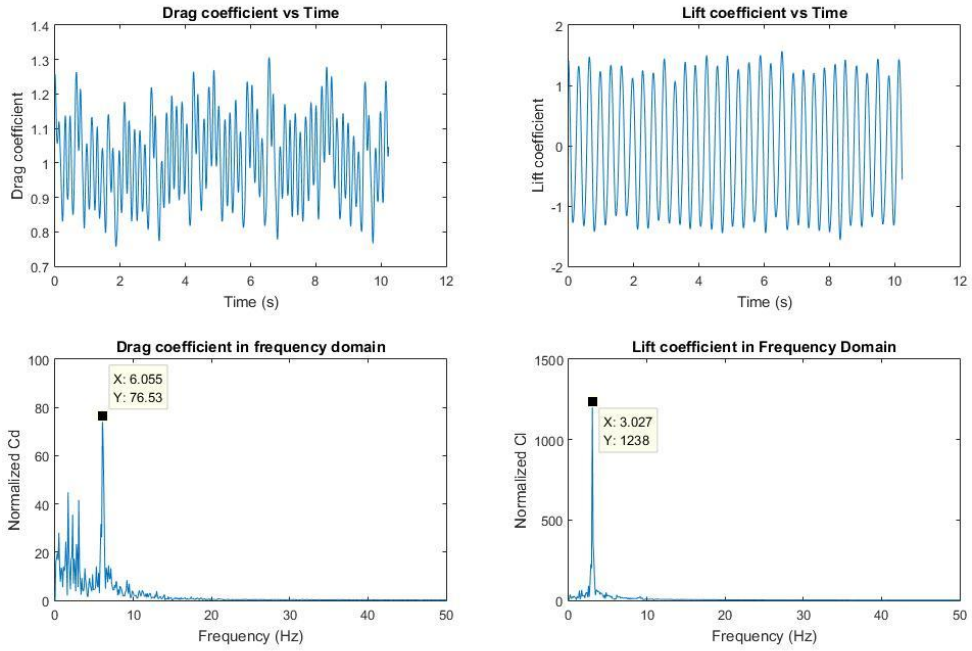

Figure B. 16 FFT Analysis of Drag and Lift Coefficients-U=1 m/s

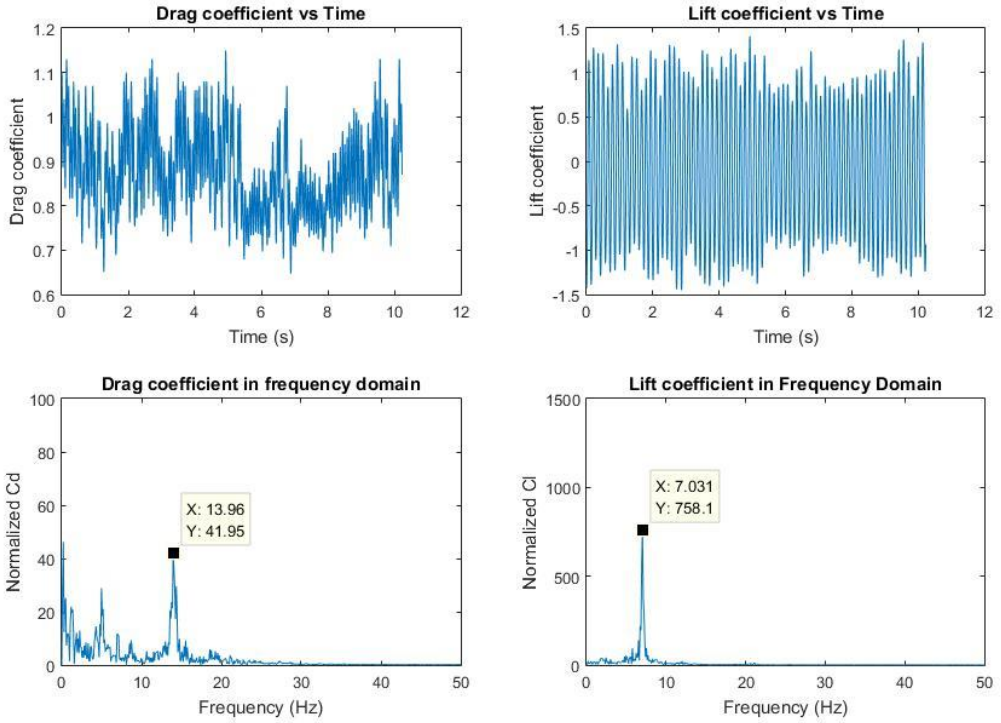

Figure B. 17 FFT Analysis of Drag and Lift Coefficients-U=2.25 m/s

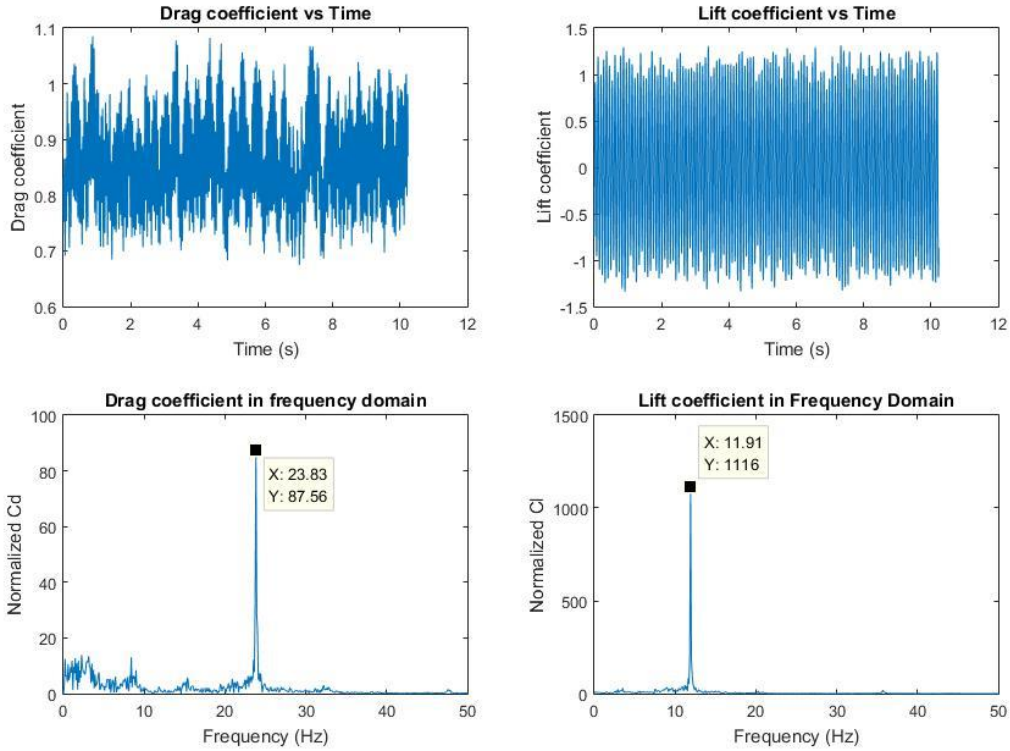

Figure B. 18 FFT Analysis of Drag and Lift Coefficients-U=4 m/s

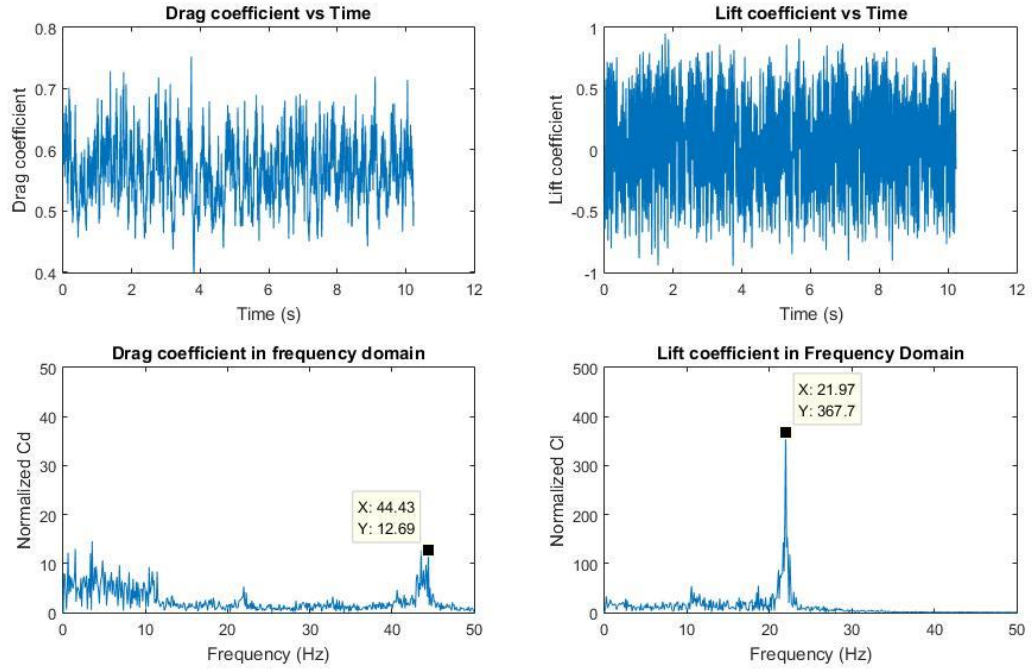

Figure B. 19 FFT Analysis of Drag and Lift Coefficients-U=8 m/s

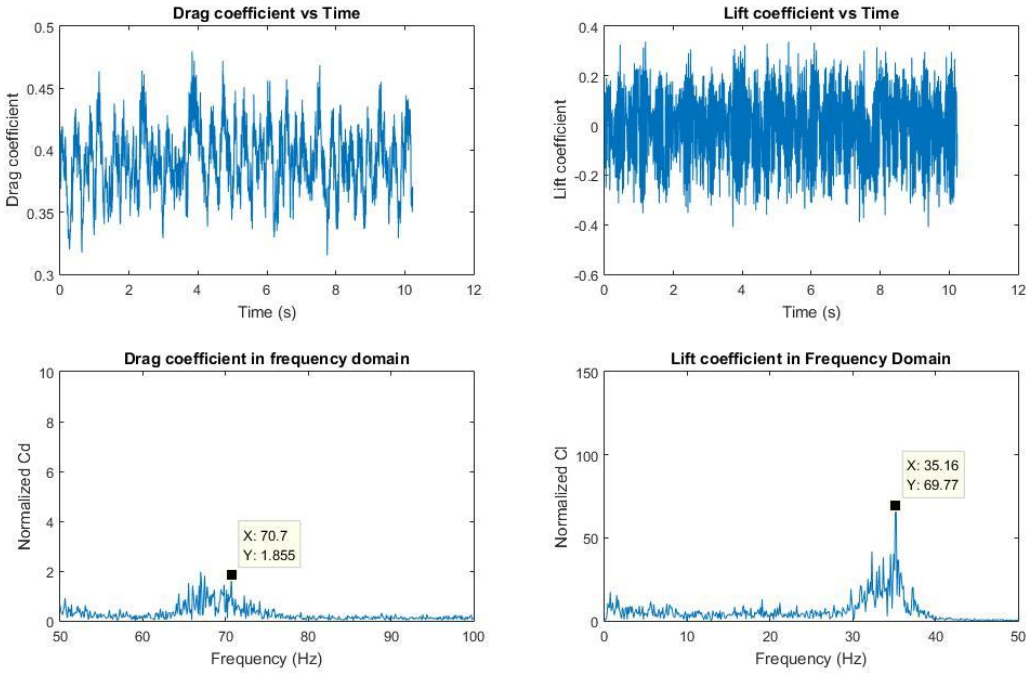

Figure B. 20 FFT Analysis of Drag and Lift Coefficients-U=16 m/s

4. FFT analysis of 3-D coupled FSI model

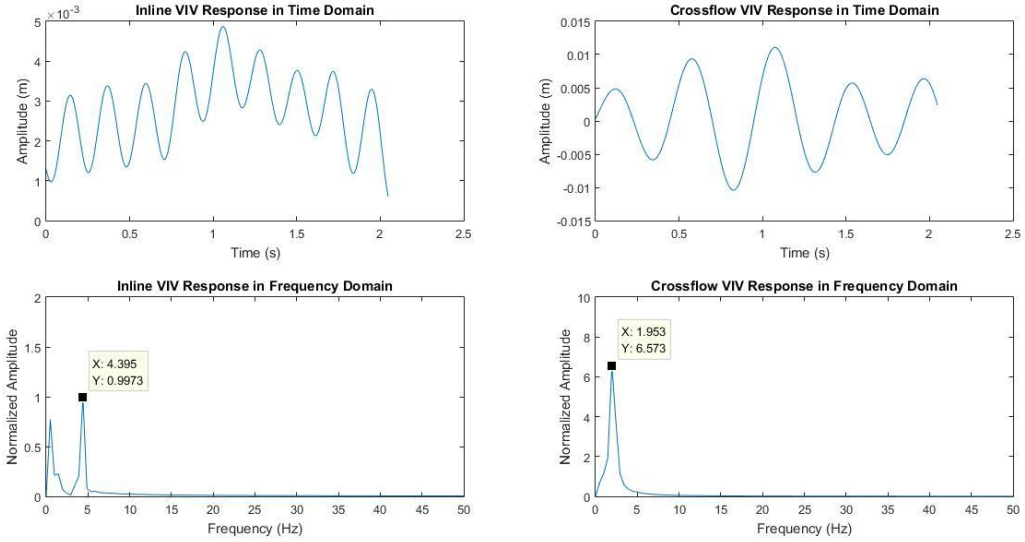

Figure B. 21 FFT Analysis of VIV Response of 3-D Coupled Model-U=0.5 m/s

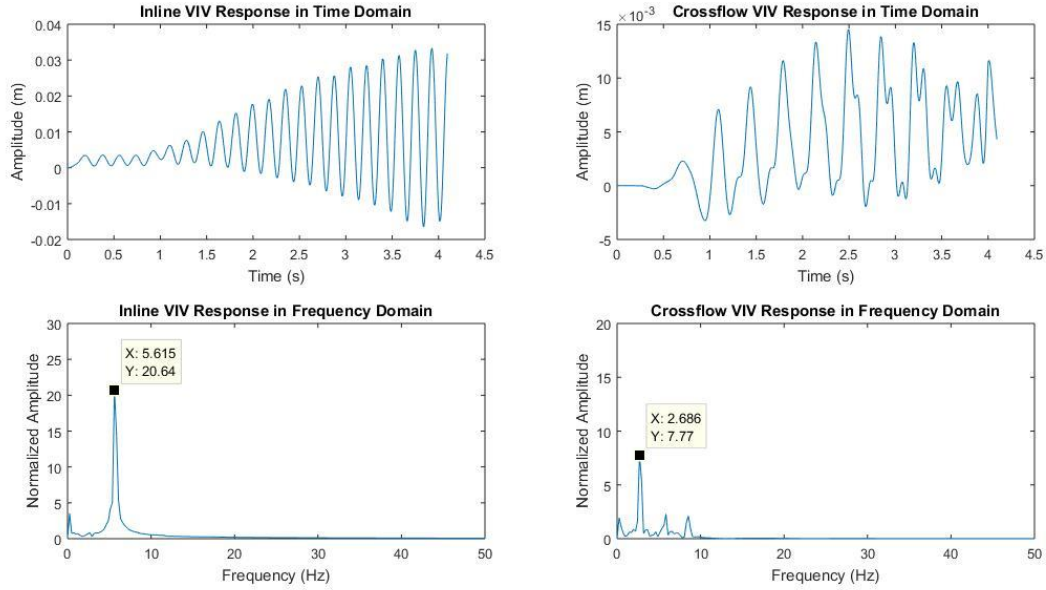

Figure B. 22 FFT Analysis of VIV Response of 3-D Coupled Model-U=1 m/s

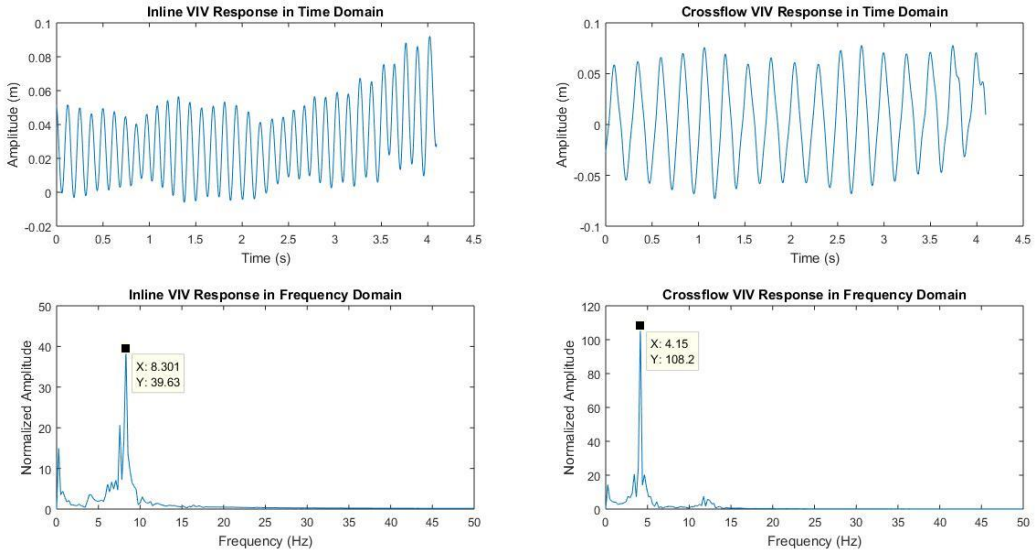

Figure B. 23 FFT Analysis of VIV Response of 3-D Coupled Model-U=2.25 m/s

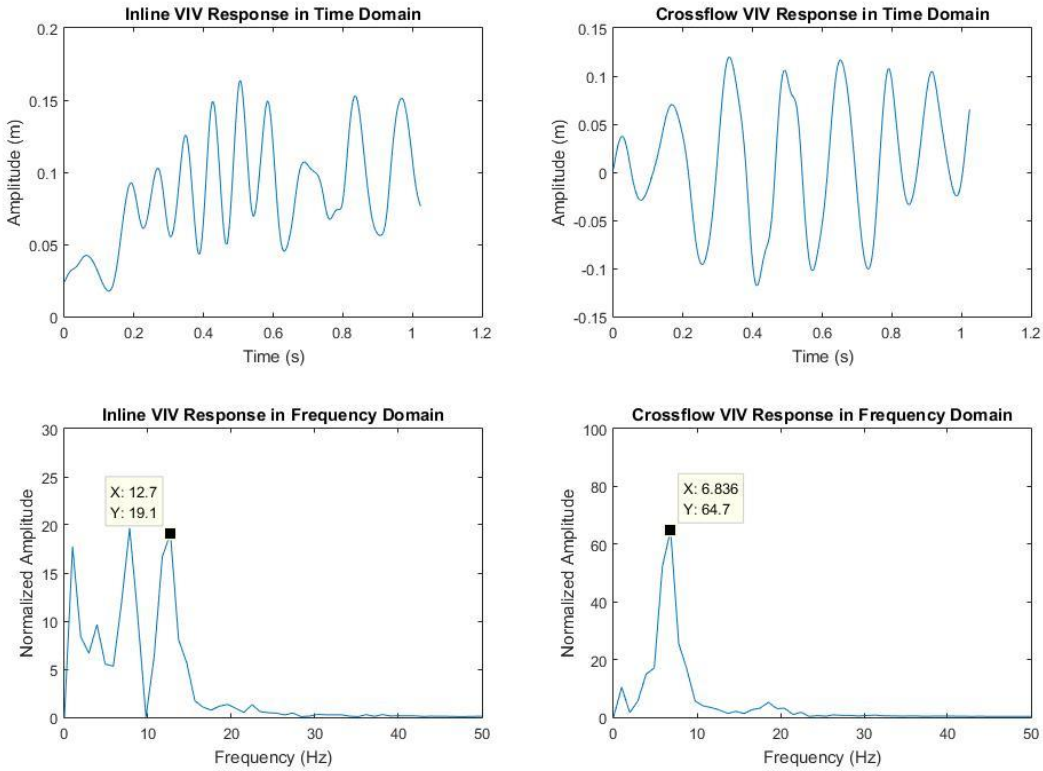

Figure B-24 FFT Analysis of VIV Response of 3-D Coupled Model-U=4 m/s

Appendix C: Tables

Table C. 1 Bill of Material

Bill of Material				
Part Number	Description	QTY	Unit	Cost
Acrylic Cylinders				
8532K19	Acrylic-1.25"/3.175cm	1	6 feet/182.9cm	$18.35
8532k22	Acrylic-2"/5.08cm	1	6 feet/182.9cm	$29.46
8486K355	Cast Acrylic-2.75"/6.9cm	1	1 foot/30.5cm	$40.04
8486K371	Cast Acrylic-3.5"/8.9cm	1	1 foot/30.5cm	$42.61
8486K943	Cast Acrylic-4.25‘’/10.7cm	1	1 foot/30.5cm	$44.63
Stainless Steel Rod				
1325T5	316 Stainless Steel Rods-1/4"/0.635cm	1	3 ft/91.44cm	$20.30
Acrylic Beam				
1227T649	Acrylic Bar-4ft length*2.5" width*1" thickness	2	4 ft/121.92cm	$50.08*2=$100.16
Cable Tie				
7130K13	Regular Cable Tie	1	5.5" lg/1" max dia	$4.43
7130K21	Cable Tie	1	17" lg/5" max dia	$6.32

Table C. 2 Energy Density-2D Preliminary Results

Diameter (m)	F-crossflow (*Hz*)	A-crossflow (m)	Energy Density - Crossflow	F-inline (*Hz*)	A-inline (m)	Energy Density-Inline	Total
0.05	4.78	0.028	0.017	9.56	0.016	0.022	0.039
0.09	3.26	0.045	0.022	6.52	0.070	0.208	0.229
0.15	1.47	0.085	0.016	2.94	0.120	0.124	0.140
0.20	0.80	0.120	0.009	1.60	0.145	0.054	0.063

Table C. 3 Boundary Conditions for 3-D FSI Simulations

Zones	Boundary Conditions
Cylinder interface	Non-slip wall
Left-sidewall	Symmetry
Right-side wall	Symmetry
Top wall	Symmetry
Bottom wall	Symmetry
Flow inlet	Velocity inlet
Flow outlet	Pressure outlet

VITA AUCTORIS

NAME: Haonan Kong

PLACE OF BIRTH: HEBEI, CHINA

YEAR OF BIRTH: 1993

EDUCATION: University of Windsor, B.A.Sc., Windsor, ON, 2016

University of Windsor, M.A.Sc., Windsor, ON, 2019

PUBLICATIONS:

Kong, H., Roussinova, V.& Stoilov, V. (2019) . Renewable energy harvesting from water flow, International Journal of Environmental Studies, 76:1, 84-101, DOI: 10.1080/00207233.2018.1494928